ISSN 1349-2667

JOURNAL OF THE EARTH SIMULATOR

MARCH 2008

VOLUME 9

EARTH SIMULATOR

THE EARTH SIMULATOR CENTER

JAPAN AGENCY FOR MARINE-EARTH SCIENCE AND TECHNOLOGY

JAMSTEC

Journal of the Earth Simulator

SCOPE OF THE JOURNAL

The Earth Simulator Center is dedicated to serving the research and development communities by providing substantial results obtained from the effective utilization of the Earth Simulator, coupled with publications of papers and articles on the earth sciences and other fields. The journal emphasizes a holistic approach; the entire earth system should be considered by simultaneously meshing our understanding of micro- and macroscopic processes. Areas of interest include, but are not necessarily restricted to:

Atmospheric and oceanic science
Climate science
Solid earth science
Computer science and technology
Nano-science
Bio-science.

In addition to original research papers, technical articles, reviews, expositions, commentaries on backgrounds policy-making, and news, are also welcome.

EDITORIAL POLICY

In order to ensure timely delivery, editors in each research & development field are entrusted with editorial responsibilities over manuscripts. In the usual case, the editor selects topics and authors; however, voluntary contributions are also welcome (submission procedures are presented at the end of the journal).

JOURNAL OF THE EARTH SIMULATOR

Contents

Volume 9 March 2008

Research Articles

Journal of the Earth Simulator, Volume 9, March 2008, 3–18

NIES/FRCGC Global Atmospheric Tracer Transport Model: Description, Validation, and Surface Sources and Sinks Inversion

Shamil Maksyutov[1,2], Prabir K. Patra[2]*, Ryo Onishi[1,3], Tazu Saeki[4], and Takakiyo Nakazawa[5,1]

[1] *National Institute for Environmental Studies, Tsukuba, Ibaraki 305-8506, Japan*
[2] *Frontier Research Center for Global Change, Japan Agency for Marine-Earth Science and Technology, Yokohama 236-0001, Japan*
[3] *The Earth Simulator Center, Japan Agency for Marine-Earth Science and Technology, Yokohama 236-0001, Japan*
[4] *Research Institute for Humanity and Nature, Kyoto 603-8047, Japan*
[5] *Graduate School of Science, Tohoku University, Sendai 980-8578, Japan*

(Received June 13, 2007; Revised manuscript accepted January 25, 2008)

Abstract We present description, validation, utilization, and update of the NIES/FRCGC (National Institute for Environmental Studies/Frontier Research Center for Global Change) off-line global atmospheric tracer transport model. The model transport is driven by analyzed meteorological fields and designed to simulate seasonal and diurnal cycles, synoptic variations, and spatial distributions of atmospheric chemical constituents in the troposphere. Tracer transport is simulated with semi-Lagrangian transport algorithm. The vertical mixing by the boundary layer turbulence and penetrative convection are parameterized. We have tested the model performance against observations of radon-222 and SF_6. The long-lived tracer transport properties are also compared to the other models and observations using the simulation of atmospheric-CO_2. Our results suggest that the model can produce realistic interhemispheric exchange rate and vertical tracer distributions in lower and mid troposphere. A new version (NIES05) of the transport model has been developed for simulating diurnally varying CO_2 concentrations at much finer horizontal resolution (0.25°×0.25°×47 level). The high resolution model results show large improvements in match with the observations at a continental site Tsukuba (~50km north-west of Tokyo). The NIES/FRCGC model is adopted to run on Earth Simulator for the purpose of source/sinks inversion of atmospheric-CO_2. We used interannually varying meteorology for the forward simulations of known CO_2 fluxes and normalized emissions from 64 divisions of the globe for which CO_2 fluxes are determined by inverse modeling of atmospheric-CO_2. We have discussed the long-term trends and interannual variability in global and regional CO_2 fluxes. The results suggest weak increases and reduction in total land/ocean and southern ocean sinks, respectively, for the period of 1982-2004. The estimated land flux variabilities have been explained by accounting for ecosystem response to inter-annual climate variability and forest fires.

Keywords: Forward Transport Model, High Resolution CO_2 Simulations, Inverse Modeling of CO_2 Sources/Sinks

1. Introduction

Atmospheric transport has to be accounted for when analyzing the relationships between observations of atmospheric constituents and their sources/sinks near the earth's surface or through the chemical transformation in the atmosphere. The tracer transport modeling is done on different scales from local plume spread, regional mesoscale transport to global scale analysis, depending on scales of the phenomena. The global atmospheric tracer transport models are usually applied to studies of the global cycles of the long-lived atmospheric trace gases such as carbon dioxide (CO_2) and methane (CH_4), because the long-lived tracers exhibit observable global patterns (e.g. interhemispheric gradient of the concentration). Global modeling analysis has helped to identify the relative contribution of the land and oceans in Northern and Southern hemisphere to the interhemispheric concentration differences for CO_2, CH_4, carbon monoxide and other tracer

* ***Corresponding author****: Dr. Prabir K. Patra, Frontier Research Center for Global Change, Japan Agency for Marine-Earth Science and Technology, 3173-25 Showa-machi, Yokohama 236-0001, Japan. E-mail: prabir@jamstec.go.jp*

species (e.g. Bolin and Keeling, 1963; Hein et al, 1997). For the case of the stable and slowly reacting chemical species, a number of studies have derived information on the spatial and temporal distribution of the surface sources and sinks by applying transport model and atmospheric observations (e.g., Tans et al., 1990; Rayner et al., 1999).

In this paper we present the development of a global atmospheric tracer transport model, its application for retrieving CO_2 flux variability by time-dependent inversion (TDI), and finally recent updates for high resolution simulations using improved meteorology. Our main objective is to model the sub-grid scale physical process parameterizations tuned to recent observations, and at the same time trying to maintain flexibility to choose meteorological input, model resolution and other practical considerations. For atmospheric tracers with a lifetime longer than several months, an accurate simulation of interhemispheric transport rate appears to be important for global scale analysis, because it affects critically the results for regional or hemispheric breakdown of unknown fluxes, such as the terrestrial CO_2 sink. Another important feature is a vertical profile of the tracer concentration over emitting regions, influenced by a rate of PBL mixing with free troposphere. Global tracer transport model intercomparison studies (e.g., Jacob et al., 1997; Law et al., 1996; Denning et al., 1999) demonstrated that the sizable difference in vertical mixing rates exists between models, and discrepancies between models and observations appear to be significant for the well established climate and transport models.

2. Model description

In this section, we describe our model design and numerical representation of the model processes, including the model equations, physical processes parameterizations and their numerical realizations. The development of NIES/FRCGC model reported here is to simulate the seasonal cycles of the long-lived tracer species at a relatively coarse grid resolution (2.5 to 5 degrees longitude-latitude), and to perform sources/sinks inversion of atmospheric-CO_2. The transport model has been improved by increasing spatial resolution and driven by diurnal cycle resolving meteorology for simulating diurnal-synoptic scale variations (version: NIES05). Present model version evolved since early 1990s (Akimoto et al., 1993; Maksyutov, 1994; Maksyutov and Inoue, 2000; Maksyutov et al. 2000). Several model algorithms and parameterizations tested in this process and were replaced or refined in order to produce more realistic simulation of the various atmospheric tracers.

2.1 Model equations

We use the terrain following σ vertical coordinate (Philips, 1957), which is defined by expression: $\sigma = p/p_s$, where p and p_S are atmospheric and surface pressures, respectively. Atmospheric constituent transport equation can be presented in the Lagrangian-style form (Williamson and Laprise, 2000):

$$\frac{dq^k}{dt} = \frac{\partial q^k}{\partial t} + \mathbf{V} \cdot \nabla_\sigma q^k + \dot{\sigma} \cdot \frac{\partial q^k}{\partial \sigma} = \frac{\partial}{\partial \sigma} F^k + S^k$$
$$\nabla_\sigma = \frac{\partial}{R\cos(\phi)\,\partial\lambda} + \frac{\partial}{R\partial\phi} \tag{1}$$

Here q^k is the mixing ratio (volume) in dry air for tracer k, and F^k is the vertical flux of that tracer due to turbulent diffusion and moist convective transport. S^k is the mixing ratio tendency due to surface fluxes and chemical transformations, λ and ϕ are the longitude and latitude in radians, R is the radius of the Earth, and $\mathbf{V}$ the horizontal wind velocity vector with longitudinal and latitudinal components (u, v). $\dot{\sigma}$ is vertical wind velocity in σ-coordinate system ($\dot{\sigma}$=+ve indicates downward motion). Eqn. (1) is solved using single time-level, time splitting scheme, with separate consecutive steps for surface emissions and transformations, semi-Lagrangian transport, vertical mixing by penetrative convection (all explicit), and vertical diffusion by turbulence (implicit). The winds (u, v) are interpolated from the global analysis winds. Vertical subgrid scale fluxes F^k are obtained using parameterizations of the penetrative cumulus convection and PBL climatology. The vertical wind in sigma coordinates $\dot{\sigma}$ is derived diagnostically from the global analysis winds. It is assumed that vertical velocity in global analysis ω represents a mass flow through constant pressure surface, and is prepared using the equation (see Washington and Parkinson, 1986):

$$\omega = p_S \cdot \dot{\sigma} + \sigma \cdot \left(\frac{\partial p_S}{\partial t} + \mathbf{V} \cdot \nabla_\sigma p_S\right), \tag{2}$$

which includes effects of air motion with respect to constant sigma surfaces (as pressure and sigma planes are not parallel) and surface pressure tendency. The $\dot{\sigma}$ is calculated from Eqn. 2 according to

$$p_S \cdot \dot{\sigma} = \omega - \sigma \cdot \left(\frac{\partial p_S}{\partial t} + \mathbf{V} \cdot \nabla_\sigma p_S\right).$$

2.2 Representation of the physical processes: cumulus convection

The vertical redistribution of tracers by cumulus convection is based on cumulus mass-fluxes calculated in a Kuo-type scheme following Grell (1995), and modified to include entrainment and detrainment processes on convective updrafts and downdrafts proposed by Tiedtke (1989). In this formulation the cloud base level σ_c is obtained by adding small perturbation to humidity and temperature at levels below 700 hPa and adiabatically lifting the air parcel until the condensation occurs. For cloud base σ_c we use the lowest level where condensation would occur, known as lifting condensation level. The supply rate of moisture available for penetrative convection is then estimated. The horizontal moisture divergence is evaluated from analysis winds and water vapor content (threshold at the cloud base is set to 0.0002 kg/kg). Low-level moisture convergence M_1 is obtained by integrating the horizontal moisture convergence below cloud base level:

$$M_1 = -\left[\int_{\sigma_c}^{1} \nabla_\sigma \left(p_S \cdot \mathrm{V} \cdot q \right) d\sigma - M_c \right] + S_{evap}. \qquad (3)$$

S_{evap} is the surface evaporation. For evaporation climatology, we use monthly surface evaporation fields by NASA GEOS-1 reanalysis for 1992-1993 (Schubert et al., 1993). Use of the monthly evaporation rate for estimating the moisture divergence has been tested by Heimann (1995). To account for deviation from the mass conservation in the wind data the moisture divergence term is corrected for non-zero divergence of the air mass M_c:

$$M_c = \int_{\sigma_c}^{1} q \cdot \nabla_\sigma \left(p_S \cdot \mathrm{V} \right) d\sigma.$$

The mass flux M_u in updraft is set to M_1 divided by water vapor mixing ratio at cloud base q_{base}, so that $M_1 = M_u \cdot q_{base}$. The vertical profiles of entrainment and detrainment rates are set proportional to M_u in accordance with Tiedtke (1989). The cloud top is determined by comparing the virtual potential temperatures in the updraft and environment, for which an overshot of 3 degrees K is allowed. The clouds thinner than $\Delta\sigma = 0.1$ are excluded. The downdraft mass flux is set to 0.2 of that in the updraft. The vertical distribution of zonal average cumulus mass flux on updrafts is presented on Fig. 1, which clearly shows the location of the tropical convective cell moving along with the seasonal changes in solar insolation, from southern hemisphere in January to northern hemisphere in July. Also the overall seasonal features in mid-latitude convective zones are well captured.

The tracers are transported vertically by applying a simplified explicit scheme. It is assumed that the updrafts and downdrafts make only a negligibly small part of a grid column; the rest is designated as environment air. First the vertical profiles of the concentrations in the updraft and downdraft air are computed taking into account rates of mixing with environment air by entrainment and detrainment, than the concentration tendencies in environment air are obtained from entrainment/detrainment rates.

2.3 Representation of the physical processes: turbulent diffusion

We used climatological planetary boundary layer (PBL) height to separate transport processes in the well-mixed PBL and free troposphere. The monthly averages of daily maximum PBL thickness data are prepared from 3-hourly PBL height data at GEOS-1 reanalysis dataset for 1992–1993 (Schubert et al., 1993). Daily maximum height is selected to representative time of trace gas observations. The summer-time PBL height over mid-lat-

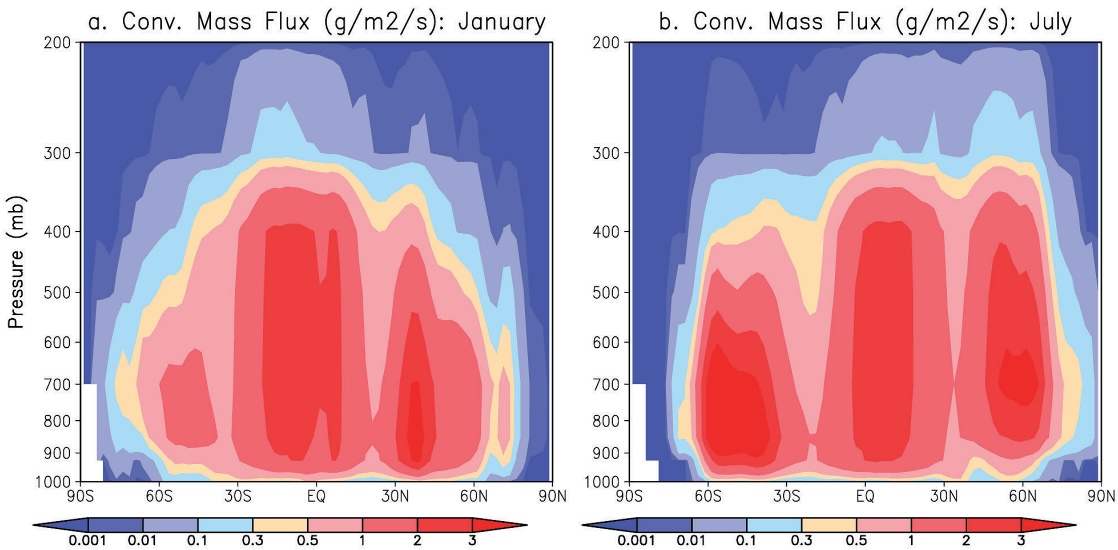

Fig. 1 An example of zonal average convective mass fluxes for January and July as estimated by the model.

itude continental areas varies around 150 hPa, approximately 1.5 km. The optimal procedure to derive the monthly PBL climatology can be debated. The other problem is lack of day to day variability. To overcome this problem and more realistic simulation of diurnal cycle, newer version of the model (version: NIES05) uses diurnally varying PBL heights at 3 hourly interval from ECMWF analyzed and forecasts products.

Below PBL top, the turbulent diffusivity is set to a constant value of 40 m^2 s^{-1}. The large scale transport such as zonally-averaged vertical profiles of constituents does not change appreciably by decreasing the diffusivity to 20 m^2 s^{-1}. The selection of the turbulent diffusivity value inside the PBL seems to be not critical as far as vertical profiles in well-mixed daytime conditions are concerned (in the older version). Above the PBL top the turbulent diffusivity K_T is calculated using local stability function, as in Hack et al. (1993):

$$K_T = l^2 \cdot S \cdot F_S(Ri).$$

Here l is the mixing length, l = 30 m. $S = \left|\frac{\partial V}{\partial z}\right|$ is the vertical wind shear, Ri is local Richardson number, defined by temperature and wind gradients as:

$$Ri = \frac{g}{S^2} \cdot \frac{\partial \ln \theta_V}{\partial z}.$$

θ_V is the virtual potential temperature, g is the acceleration of gravity. Stability dependent function $F_S(Ri)$ is defined as:

$$F_S(Ri) = (1 - 18 \cdot Ri)^{\frac{1}{2}} \quad \text{for unstable conditions} \ (Ri < 0)$$

and

$$F_S(Ri) = 1 - \frac{Ri}{Ri_C} \quad \text{for stable conditions} \ (0 < Ri < Ri_C),$$

where $Ri_c = 0.2$ is a critical Richardson number, above which $F_S(Ri) = 0$.

2.4 Semi-Lagrangian transport and trajectory calculation

Semi-Lagrangian transport algorithm is an effective way to solve the tracer transport problems in a polar coordinate system (Williamson and Rasch, 1989), as opposed to the regular-grid schemes formulated in flux form, that have a singularity near the poles caused by small grid size in longitudinal direction. In the semi-Lagrangian approach the tracer concentration change due to transport from initial state (time t_0) to new value at next time step $t_0 + \Delta t$ is evaluated in 2 steps:

Step 1 (Trajectory calculation): For the each grid point location a three-dimensional trajectory is calculated for an air parcel, which arrives to that grid point at time $t_0 + \Delta t$. The trajectory location at time t_0 is designated as departure point, and the trajectory itself is called a back trajectory, because it is calculated backward in time.

Step 2 (Interpolation): A concentration at departure point at time t_0 is obtained using interpolation from nearby grid point values. In the absence of mixing and transformation processes, concentration at arrival point should be exactly same as that at the departure point, thus the tracer concentrations at new time step $t_0 + \Delta t$ are set to those at corresponding departure points.

The trajectories are calculated using explicit integration of the air parcel motion in the Cartesian coordinate system originated in the Earth center. The coordinate transformation from polar to Cartesian coordinate system and back is used on the each time step. Calculation of the departure point on each time step is done in 3 sub-steps:

a) Interpolate wind and pressure to the current air parcel position in polar coordinates, using bilinear approximations.
b) Convert the winds and air parcel coordinates to Cartesian coordinate system centered at the Earth center, and calculate displacement tangent to Earth surface.
c) Convert new position back to polar coordinate system and finding sigma level change by integrating vertical motion.

We provide here a short description of the trajectory calculation equations (as referred in Step 1 above). The horizontal (parallel to Earth surface) air parcel movement is determined in the earth-centered coordinate system. The earth centered system has x–axis passing the point on the Earth surface at 0˚E, 0˚N; y-axis passes via 90˚E, 0˚N, z-axis passing via 90˚N. Horizontal motion in polar coordinates (λ, ϕ) can be represented as

$$R \cdot \cos(\phi) \frac{d\lambda}{dt} = u, \ \ R \cdot \frac{d\phi}{dt} = v.$$

The air parcel displacement in the earth-centered system is given by

$$dx = -\ \delta\phi \cdot \sin(\phi) \cdot \cos(\lambda) - \sin(\phi) \cdot \delta\lambda$$
$$dy = -\ \delta\phi \cdot \sin(\phi) \cdot \cos(\lambda) - \sin(\phi) \cdot \delta\lambda,$$
$$dz = -\ \delta\phi \cdot \cos(\phi)$$

where dx, dy, dz are the air parcel displacements in x, y, z directions in the earth-centered coordinate system. $\delta\lambda$, $\delta\phi$ are displacements in longitude, latitude directions and calculated as:

$$\delta\lambda = u \cdot \Delta t = u/(R\cos\phi)\delta t, \ \delta\phi = v \cdot \Delta t = (v/R)\delta t.$$

Here Δt is the time step (negative for back-trajectory). A new position of the air parcel is given by

$$x = R \cdot \cos(\phi) \cdot \cos(\lambda) + dx$$
$$y = R \cdot \cos(\phi) \cdot \sin(\lambda) + dy.$$
$$z = R \cdot \sin(\phi) + dz$$

x, y, z are longitude, latitude height position of the air parcel, R is radius of the Earth. After the position in the earth-centered coordinate system is determined, the position in the polar coordinate system is given by: $\phi = \arctan\left(z/\sqrt{x^2 + y^2}\right)$ $\lambda = \arctan(y/x)$.

This trajectory calculation module has been extensively used for analysis of the relationship between the atmospheric transport and observed time series of the long-lived tracers such as nitrous oxide (Tohjima et al., 2000), methane (Tohjima et al, 2002) and ozone (Pochanart et al., 2001). The studies where performed with the same wind and trajectory calculation algorithm as in present 3-D transport model, and a good correlation was observed between the variations of the atmospheric composition and trajectory pathways over a time periods extending from 1994 to 1999. Those results give us some degree of confidence in the model's horizontal transport performance.

2.5 Model grid

The model's horizontal and vertical resolutions match those of the meteorological dataset when possible. We use pressure level ECMWF operational analyses at 12-hour time step and 2.5 degrees horizontal resolution in model validation experiments, and NCEP reanalysis data at same resolution for multiyear inverse model simulations (ECMWF, 1999; Courtier et al., 1998). Same horizontal resolution is used in the model; however, the grid layout is different from the meteorological dataset. The first model grid cell on a horizontal plane is located near South Pole, and is confined between (0˚E, 90˚S) and (2.5˚E, 87.5˚S), the last one, at North Pole, is confined between (357.5˚E, 87.5˚N) and (0˚E, 90˚N). Vertical grid layout was designed to provide enough layers to match the resolution of the wind dataset (ECMWF operational analyses), and the variability in the boundary layer height. The validation tests were performed with 15 layer vertical grids, which have slab centers at $\sigma_K = \{.97, .93, .89, .85, .775, .7, .6, .5, .4, .3, .25, .2, .15, .1, 0.03\}$. The slab interfaces are at mid levels $\sigma_{K+1/2} = (\sigma_K + \sigma_{K+1})/2$. Model grid is staggered in vertical dimension. Turbulent diffusivities, convective mass fluxes are assigned to slab interfaces $\sigma_{K+1/2}$, while the winds, temperature, humidity, constituents are assigned to slab centers σ_K. The winds are interpolated from the meteorological analysis grid to the model grid using bilinear interpolation in longitude and latitude in log-pressure coordinate.

The NIES05 model version uses meteorological data by NCEP operational analyses at 26 levels and 1×1 degree resolution at 6 hourly interval and the model simulations are performed at varied horizontal resolution; e.g., 0.5×0.5, 1×1, and 2×2 degrees. This version has 47 vertical layers.

2.6 Mass fixer description

The total tracer mass tendency by the semi-Lagrangian transport algorithm usually deviates from zero, which is often negligible in short term but can disturb the global trends and tracer budgets in long-term simulations. A variety of mass fixers are applied in transport models in order to keep total tracer mass unchanged during transport (Hack et al., 1993; Rasch et al., 1995). We distribute the required correction proportionally to local advection tendencies as described in Taguchi (1996). The mass fixer is designed to conserve as total tracer mass, which is calculated as an integral (with constant factor omitted):

$$M_q = \int_0^1 \int_{-1}^1 \int_0^{2\pi} p_S \cdot (1 - 0.61 \cdot q_W) \cdot q \cdot d\lambda \cdot d(\sin\phi) \cdot d\sigma \tag{4}$$

Here q_w is the water vapour mixing ratio, so $(1–0.61 \cdot q_w)$ is the dry air mass fraction. Mass fixer is designed to conserve M_q by balancing the positive and negative tendencies. The constraint for tracer tendencies on each time step is derived from mass balance equation Eqn. 4 as follows

$$\begin{aligned} \frac{\partial}{\partial t} M_q = \int_0^1 \int_{-1}^1 \int_0^{2\pi} & \Big\{ p_S \cdot \left(1 - 0.61 \cdot q_W\right) \cdot \tilde{\dot{q}} \\ & + q \cdot \frac{\partial}{\partial t}\left[p_S \cdot \left(1 - 0.61 \cdot q_W\right)\right] \Big\} \cdot d\lambda \cdot d(\sin\phi) \cdot d\sigma \\ & = 0. \end{aligned}$$

Here $\tilde{\dot{q}}$ is the corrected tendency for each tracer. We apply two different factors a_p, a_n as multipliers for positive and negative tendencies so that

$$\tilde{\dot{q}} = \dot{q} \cdot \left[a_p \cdot \theta(\dot{q}) - a_n \cdot \theta(-\dot{q})\right],$$

where $\dot{q}$ is tracer tendency from semi-Lagrangian transport step, $\theta(\dot{q})$ is the step function ($\theta(x) = 1$ for $x \geq 0$, and $\theta(x) = 0$ for $x < 0$). The condition $\max(a_p, a_n)$ is enforced to keep the solution monotonic.

Recent tests conducted for TransCom 3 intercomparison experiment (Gurney et al., 2002) revealed that the mass fixer we use does have a detectable non-local ("teleconnection") effect. It is caused by values of a_p and a_n being slightly different for each particular tracer. The values of a_p and a_n influence the rate of interhemispheric transport, and the difference is generally larger than that for other mass fixers (R. Law, personal communication, 2001), such as flat concentration adjustment (Hack et al., 1993).

2.7 Treatment of the surface emission-sink fields and chemical transformations

The model is designed to handle constant surface emission fields and seasonally changing emissions in the form of 12 monthly average fields per year. The NIES05 version can ingest fluxes at higher frequency, at up to hourly time interval. The monthly average emissions are interpolated linearly to daily values, on the 15th of each month the emission rate is equal to the monthly average for that month as provided by emission inventory files. The emission inventory fields have higher resolution (e.g., 1×1 degree), than the model grid (e.g., 2.5×2.5 degrees), so the input dataset is mapped to a model grid by counting the overlap area of each input data cell to all model grid data cells. That assures that the global total emission flux is conserved during interpolation.

3. Validation of NIES/FRCGC global transport model

An effective way to validate the atmospheric transport models is by simulating the non-reacting or slowly reacting atmospheric tracer species with well-known emissions and transformations. The tracers of choice are both short lived like radon-222 for diagnosing local/regional transport (Jacob et al., 1997), and long-lived species for evaluating large scale/interhemispheric transport such as SF_6 (Denning et al., 1996; Levin and Hesshaimer, 1996; Maiss et al., 1996), ^{85}Kr (Jacob et al., 1987; Heimann and Keeling, 1989; Zimmermann et al., 1989), chlorofluorocarbons (Prather et al., 1987; Mahowald et al., 1997). General requirements to the suitable tracer species can be summarized as follows: a) availability of reliable emission inventory; b) stable emissions with little seasonal and diurnal variations; c) availability of the observations at required temporal and spatial scales. Most of naturally emitted gaseous species like carbon dioxide, methane, and carbon monoxide can not be used for the model validation because of the large and poorly known spatial-temporal variability of their sources and sinks. Among the most widely used are the gases of the anthropogenic origin – SF_6 and chlorofluorocarbons, because their emission rates are constrained by both the industrial statistics and the trends in global atmospheric content and in addition have no known chemical loss in the troposphere. On the other hand radon-222 (atmospheric residence time of 3.8 days) is emitted only naturally, but its emission rate is related to stable factors, such as type of soil and rocks, rather than the changing vegetation or weather conditions.

We evaluate the model's overall performance using results from several extensively tested global tracer transport models and comparing our model simulations with observations. Those model simulations include the WCRP model intercomparison experiment for radon (Jacob et al., 1997), TransCom experiment (Law et al., 1996) for CO_2 transport intercomparison, and SF_6 transport intercomparison experiment TransCom 2 (Denning et al., 1996). These modeling setups were developed by large transport modeling community, and provide concise and tested set of atmospheric observations and surface emission fields. This gives us an opportunity to concentrate on limited number of key and integral simulated tracer field parameters. The limited set of tests may not actually substitute running the comprehensive validation using large variety of observations (e.g., Dentener et al., 1999), but can still give valuable information on the model performance in terms of large scale averages.

3.1 Evaluation of vertical transport using simulation of radon

Radon-222 is a product of radium-226 decay and has a lifetime of 3.8 days in the atmosphere. The surface radon emission rate varies considerably from 0.5 to 2 atoms $cm^{-2}\ s^{-1}$; the emission is suppressed by poorly conducting wet soils and snow cover. Yet there is no better choice of relatively short-lived and widely observed tracer for validating a transport model for continental and remote oceanic atmosphere, and between boundary layer and free troposphere. For validating the model performance using transport of radon-222, we follow the World Climate Research Program (WCRP) inter-comparison experiment specification (Jacob et al., 1997). Radon-222 surface fluxes were set to 0.005 atoms $cm^{-2}\ s^{-1}$ for oceans and 1 atom $cm^{-2}\ s^{-1}$ over land between 60°S to 60°N, and to 0.005 atoms $cm^{-2}\ s^{-1}$ for land between 60°N to 70°N.

The observed and simulated radon concentrations for different heights at Crozet, Hawaii and Cincinnati are compared (not shown) by using the data at Cincinnati (Gold et al., 1964), Crozet (Lambert et al., 1995), and Hawaii (Kritz et al., 1990). The model appears to underpredict surface concentrations at Cincinnati and upper atmospheric observations over Hawaii (200 hPa level), and slightly over-predict the observations at Crozet island. Worth mentioning, however, that several models that participated in Jacob et al. (1997) inter-comparison also failed to capture observed variability in the upper troposphere and reproduce the high radon observed values at 200 hPa over Hawaii. Crozet Island is located south of African coast; the data indicate low background concentrations of below 10^{-21} mol mol^{-1}, with infrequent high radon episodes lasting few days. In case of Crozet, Jacob at al. (1997) found that the low background concentrations are over-predicted; but the amplitude of the high radon episodes is captured more successfully by the "established" transport models, which is believed to be an indication of models' ability to transport radon to remote atmosphere without significant amplitude loss due to diffusion. The summer maximum at Crozet in our model is within the range of the observed variability.

Figure 2 shows the comparison for winter and summer averages together with other model results as presented by Jacob et al. (1997). The comparison to the observations concludes that our model performs similar to the established three-dimensional transport models (see Fig. 2 caption for details), and the model simulated vertical profiles are close to observed ones. The model results are within the range of observations (widened by observed variability) for all but summer mixed layer value. Even in later case it is close to lower bound of the observation ranges. This may indicate that the summertime mixing (ventilation of the boundary layer) is stronger than that occur in the real world. Same conclusion is also applicable to some other transport models as well (see Fig. 2). However this low value is not conclusive evidence in the view of the fact that the local emission rate uncertainty could be as high as 50%.

3.2 Evaluation of interhemispheric transport using long-lived gases

The validation of the inter-hemispheric and vertical transport became more reliable with the increasing availability of the observational data on a stable tracer, SF_6,

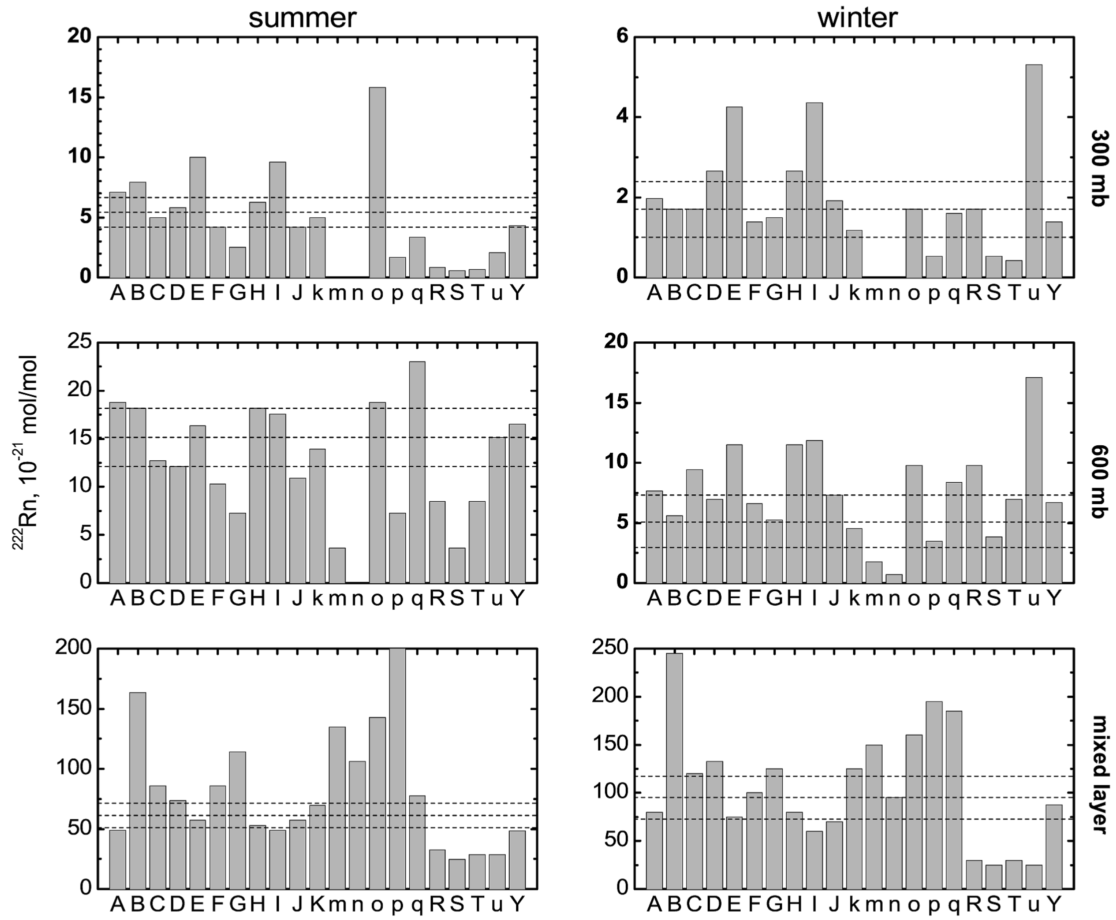

Fig. 2 Comparisons between observations and model simulations of radon-222 averaged for 3 continental sites during winter and summer. Results at three vertical levels (surface, 600 mb and 300 mb) are shown. Models A to J are established three-dimensional models, models k to q are three-dimensional models under development, R to U are two-dimensional models, and Y is for this model. Observations are taken at Cincinnati (40˚N, 84˚W), Socorro (34˚N, 107˚W) and Kirov (58˚N, 49˚E). Different model results are designated by letters along the x-axis: A. CCM2, B. ECHAM3, C. GFDL/ZODIAC, D. GISS/H/I, E. KNMI/TM2, F. LLNL/GRANTOUR, G. LLNL/E, H. LMD, I. TM2Z, J. MOGUNTIA, k. CCC-GCM, m. LaRC, n. LLNL/IMPACT, o. MRI, p. TOMCAT, q. UGAMP, R. AER, S. UCAMB, T. HARWELL, u. UW, Y. NIES/FRCGC (this work).

which can be analyzed accurately in the laboratory after sampling to flasks, has a long atmospheric lifetime of more than 3000 years (Ravishankara et al., 1993), has steady emissions, verifiable via global atmospheric abundance observations (Levin and Hesshaimer, 1996; Geller et al., 1997). We follow the TransCom 2 protocol (Denning et al., 1999) in applying the global emission scenario for SF_6, and present the 5-year simulation that starts from globally homogeneous concentration of 2 pptv (parts per trillion volume) at the beginning of 1989. In Denning et al. (1999) intercomparison the initial value was set to 2.06 pptv, and that resulted some overestimation of the global 1993 average by all models. They had to scale down the concentration increase by a factor of 0.936, which may be interpreted as same amount of decrease in emission rate considering linearity in SF_6 transport.

The annual average of simulated SF_6 concentration for 1993 is compared to the observations compiled by Denning et al. (1999) and plotted in Fig. 3. The common problems that can be observed with both our model and models reported by Denning et al. (1999), are large mismatch for Barbados (13°N, 59°W), and large variability in mismatch for continental and background Northern hemispheric background locations. The pole-to-pole difference (South Pole to Alert) is captured fairly well by our model. Similar simulations of fossil fuel component of CO_2 flux are also conducted. We estimate an interhemispheric exchange time of about 1.5 year and 0.9 year by considering the hemispheric means of surface concentrations and values integrated for the whole hemisphere, respectively.

According to the data presented, the model in a given configuration tends to under-predict inter-hemispheric

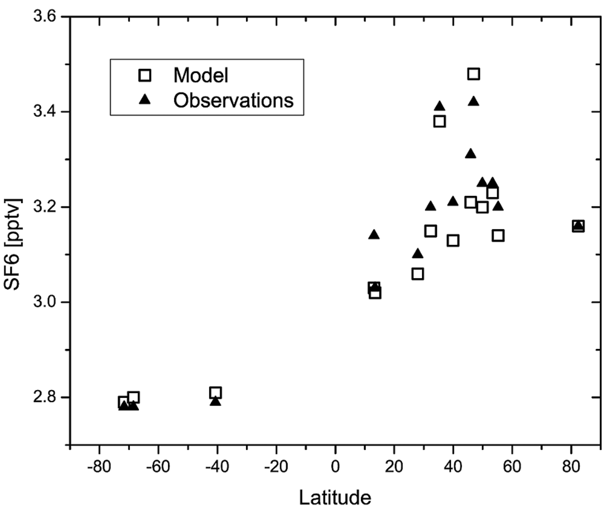

Fig. 3 Interhemispheric gradients in modeled and observed SF_6 concentrations during 1993 are depicted. The modeling set up for this simulation is similar to TransCom 2 experiment (see text).

gradient in background locations by 10% of interhemispheric difference (taken as 0.4 pptv), but at the continental sites the difference can be both positive and negative. The average mismatch is comparable to that by other established transport models in TransCom 2 intercomparison, but indicates that there are scopes for further improvements in forward modeling as well as the spatial distribution of SF_6 emission. The wish list for those improvements would include: a) increasing the interhemispheric gradient in background atmosphere by extra 10% to improve the match between model and observations at background locations, and b) at the same time keep the match at continental locations within present level. The later action would require enhancing the vertical mixing in lower troposphere potentially leading to widening the mismatch with radon-222 data as in Fig. 2. Some these improvements are introduced in the NIES05 version of the model and some results have been discussed later.

3.3 CO_2 transport simulation with TransCom 1 experimental protocol

Another test of the model performance is given by the TransCom 1 intercomparison study, which provides the handy set of parameters for evaluating the both horizontal (interhemispheric) and vertical tracer transport by comparison with the established models. Here we report the simulation results for “fossil fuel CO_2” tracer, as specified by Law et al. (1996). The fossil fuel CO_2 source field derived by Inez Fung is same as in Tans et al. (1990), and is based on CO_2 emission inventory by Marland (1989). The results are presented as averages for North and South Hemispheres for surface level, 500 hPa, and 200 hPa levels. The interhemispheric concentration gradient defined as difference in hemispheric averages simulated by our model and models reported by Law et al. (1996) are summarized in Fig. 4. According to previous studies with short/long-lived tracers, such as Jacob et al. (1987), Denning et al. (1999), the extensively validated models such as GISS and TM2 are capable of reproducing the interhemispheric gradient of the long-lived tracers with the accuracy of about 10% or better. We use the same yard-stick for evaluating the performance of our model. NIES/FRCGC model is not considerably different from TM2 in terms of the North-South difference at surface. Along with several other global tracer transport models it predicts about 3-ppm difference at surface, however there is a difference in vertical profile of interhemispheric gradient. At the level of 500 hPa, the relative difference between models becomes larger with TM2 and GISS showing larger interhemispheric difference as compared to others. At 500 hPa our model also produces larger gradient than other models, and difference from TM2 is

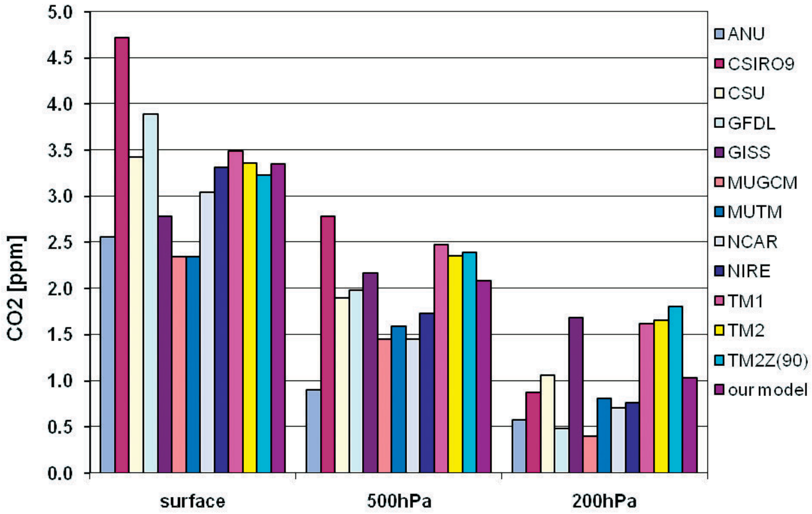

Fig. 4 Interhemispheric gradients in fossil fuel CO_2 tracer simulated by TransCom 1 models and NIES/FRCGC model are shown for three vertical levels.

minor. That is not the case at 200 hPa level. As one can see on Fig. 4, the North-South difference at 200 hPa is as large as 1.5 ppm for GISS and TM2, and about 1 ppm or less for our and other models. Main reason is a stronger vertical transport in GISS and TM2 models, which also makes smaller the model simulated difference between continental boundary layer and background oceanic air, as discussed in Law et al. (1996) and Denning et al. (1999).

4. Introduction to High resolution model version (NIES05)

While the NIES/FRCGC model successfully captures overall features in tracer transport and being used for CO_2 sources/sinks estimation by inverse modeling of atmospheric-CO_2 (section 5), there are increasing demands for simulating tracer distributions at sub-daily time and local scales. Presently about 30 stations are observing atmospheric CO_2 using in situ deployed instruments and provide hourly average values for scientific research (WDCGG, 2007). To understand the observed variability, the transport model simulations are required to be performed at increased spatial resolution and driven by diurnally varying meteorology. We have run our transport model (version NIES05) as high horizontal resolution as 0.25×0.25 degree longitude-latitude, in order to investigate the impact of grid resolution on global CO_2 transportation. Here, we present our simulation results at 4 horizontal resolutions; 2×2, 1×1, 0.5×0.5 and 0.25×0.25 degrees. The vertical resolution is enhanced to 47 levels for better resolving the mixing processes in the boundary layer. For resolving the diurnal variations in surface concentrations, the NIES05 model version is driven by 3-hourly PBL height data from ECMWF analyzed and forecast products (http://www.ecmwf.int; path:/products/data/operational_system). The other 2-D and 3-D meteorological parameters, e.g., sea-level pressure, winds, temperature, are taken from NCEP final analysis (http://dss.ucar.edu;path:/datasets/ds083.2/). Computational demand increased many-fold to run the model at 0.5×0.5 degree horizontal resolution and 47 vertical level; e.g., time and memory size required for one month simulation of 3 tracers are 1.4 hours in real time and 4.4 GB, respectively on 6 CPUs of Earth Simulator (NEC SX-6 series processor).

Three surface CO_2 fluxes are used; SiB3 hourly varying terrestrial ecosystem flux (Denning et al., 1996), seasonally varying ocean flux (Takahashi et al., 2002) and anthropogenic fossil fuel emissions (Marland, 1989) following the TransCom continuous experiment protocol (Law et al., 2006). Higher resolution anthropogenic CO_2 emission distributions are generated from 1×1 degree emission inventory, by redistributing the fluxes spatially following the 2.5min global population map data (CIESIN, 2000), and combined with lower resolution ecosystem and oceanic flux data. This redistribution procedure for fossil fuel emission is an approximation and should ideally be placed according to the source locations. The summation of those fluxes is considered as the total CO_2 surface flux. August 2002 is selected as the target period of our test simulation. The preceding simulation (spin-up run) is performed at 2×2 degree horizontal resolution for the period of 1st January to 31st July, 2002 in order to obtain realistic spatial CO_2 gradients. Figure 5 shows the snapshots of surface CO_2 distributions over East Asia at the resolutions of (a) 2×2 and (b) 0.25×0.25 degree. Though the area-averages concentrations are similar in both cases, the distribution patterns are quite different from each other. For example, Figure 5b shows much clearer city plumes than Fig. 5a. It also shows clearer vortex shape due to a typhoon near the Kyusyu area (130˚E, 30˚N).

Figure 6 shows a comparison of atmospheric CO_2 data at Tsukuba 200m tall tower with NIES05 model results at different horizontal resolutions. Tsukuba is located close to a large anthropogenic CO_2 emission region around Tokyo (distance ~ 50 km). The observation data are provided by Y. Sawa and H. Matsueda of Meteorological Research Institute (MRI), Tsukuba (also available at WDCGG website). Each simulation result has its offset value, which is determined from the average value in the August. The higher-resolution simulations have stronger diurnal changes, which are more consistent with observed diurnal cycle. Furthermore, they produce better predictions, particularly during the 3rd to 7th August period when winds from Tokyo dominate. Model simulations at horizontal resolution of 1×1 degree or coarser do not resolve the separation between Tokyo and Tsukuba emissions and transport as Tokyo and Tsukuba reside within the same grid cell and sampling grid do not accurately represents Tsukuba (see Fig. 6 caption). The nearest north-eastern model grid is selected for sampling, and the distance between model grids and Tsukuba are estimated to be about 128, 58, 23 and 8 km for 2×2˚, 1×1˚, 0.5×0.5˚ and 0.25×0.25˚ horizontal resolutions, respectively. Thus the highest resolution run enables us to capture the CO_2 variabilities more realistically compared to the coarse resolution runs.

The simulations of CO_2, radon-222 and SF_6 at hourly, daily and synoptic time scales are being evaluated under the TransCom continuous intercomparison project (Law et al., 2006). Though the first forward simulation results are encouraging this model version will not be used in surface CO_2 sources/sinks inversion for resolving flux variabilities at high spatial and temporal resolutions, until a rigorous evaluation of model simulations of the above mentioned species is completed.

5. Inverse modeling of CO_2 sources and sinks

Using the NIES/FRCGC model version (2.5×2.5 degrees horizontal resolution and 17 vertical layers) we have employed a 64-region time-dependent inverse model (TDIM) for deriving CO_2 fluxes at monthly time interval from atmospheric-CO_2 data at 87 stations. Our 64-region TDIM is based on that has been used in Rayner et al. (1999) and partially follows the TransCom3 protocol (Gurney et al., 2000). The results have been widely reported by analyzing interannual variability in fluxes (Patra et al., 2005a,b), and for understanding the anomalous CO_2 growth rate at Mauna Loa during 2001–2003 (Patra et al., 2005c). Fluxes for oceanic regions have been validated in comparison with independent oceanic-pCO_2 inversion and explored for mechanistic understanding of the flux variabilities using biogeochemical models of land and ocean (Patra et al., 2006b, 2007). Here we will present some recent developments that support the derived flux variabilities and trends by our TDIM setup. In addition, NIES/FRCGC model has been utilized exclusively for optimization of futuristic surface observation networks and to study utility of satellite measurements in surface sources/sinks estimation. Most of these studies

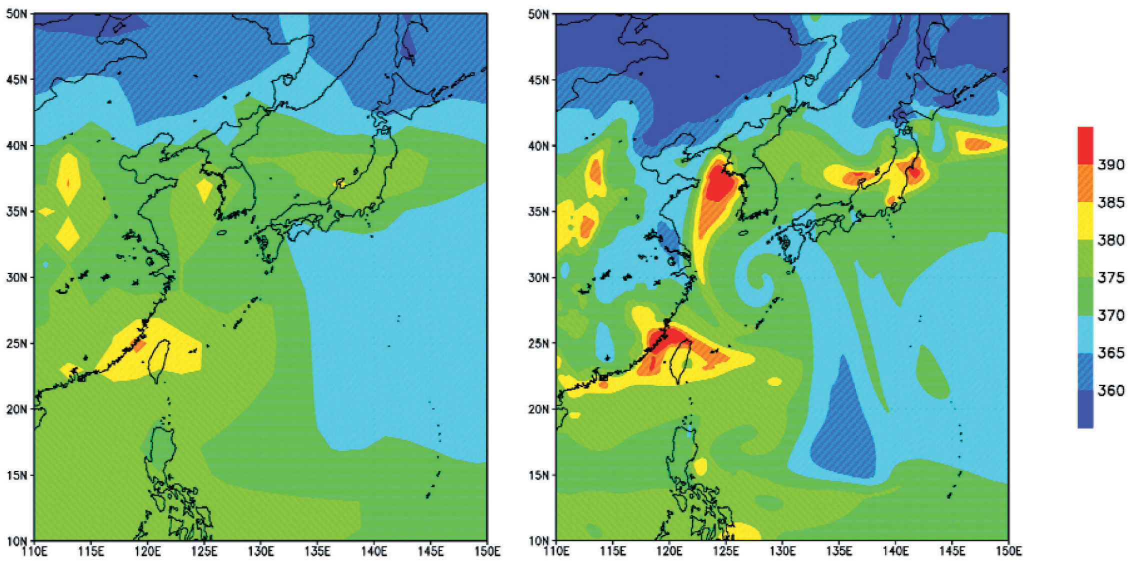

Fig. 5 Surface CO_2 concentrations at 03Z30AUG 2002 obtained from (a) 2×2 degrees (left) and (b) 0.25×0.25 degree (right) horizontal resolution simulation.

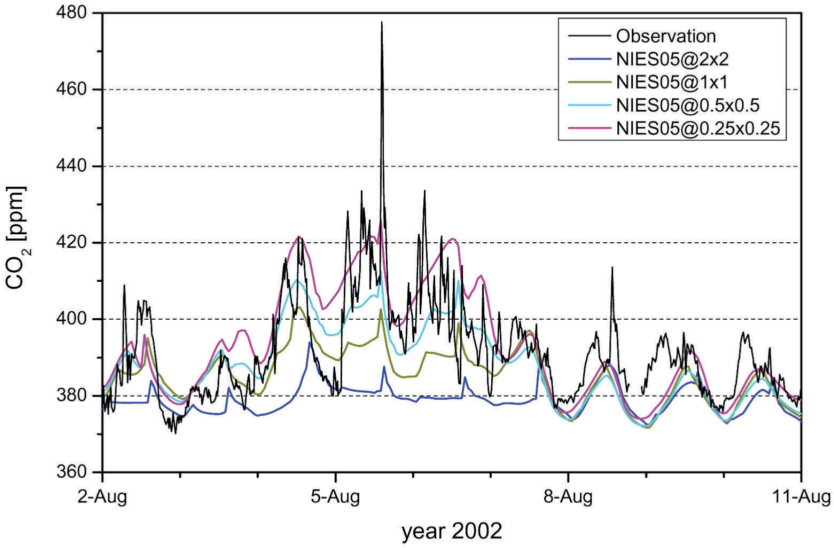

Fig. 6 Results of NIES05 at four kinds of resolutions at Tsukuba (36.05˚N, 140.13˚E) 200m high tower, which is in close proximity of megacity Tokyo (35.66˚N, 139.75˚E), and is occasionally under the influence of strong anthropogenic sources (an episode of up to about 70 ppm on 5th afternoon). An offset of 373 ppm is added to the model values for comparison with observations. The model sampling grids are located at (37˚N, 141˚E), (36.5˚N, 140.5˚E), (36.25˚N, 140.25˚E) and (36.13˚N, 140.13˚E) in 2×2˚, 1×1˚, 0.5×0.5˚ and 0.25×0.25˚ model resolutions, respectively.

are conducted using synthetic data experiments in time-independent inversion mode for 22, 42 or 432 region divisions of the globe (Maksyutov et al., 2003a; 2003b; Patra et al., 2002; 2003a; 2003b). Multi-model intercomparisons of time-independent and time-dependent CO_2 flux inversions are done under the TransCom3 project (Gurney et al., 2002, 2003, 2004; Law et al., 2003, Baker et al., 2006; Patra et al., 2006a). The inverted fluxes corresponding to NIES/FRCGC model are found to be similar to most other 12 or 16 participating models.

Figure 7 shows the TDIM estimated fluxes for the period 1979–2005 using NIES/FRCGC forward model simulations driven by interannually varying winds (TDI/64-IAV), and cyclostationary winds and CO_2 measurements at 67 stations (TDI/64-CYC/67) and 19 stations (TDI/64-CYC/19). Use of cyclostationary winds and smaller CO_2 data network significantly reduces the interannual variability in TDIM derived CO_2 fluxes for both the land and ocean regions (see Patra et al., 2006b for a discussion). However, the trends in fluxes are fairly independent of the forward model transport. Total land and ocean sinks appear to be increasing over the 1980–2005 periods (Fig. 7a, b) though the interannual variability has large influence on the trends derived, i.e., selection of period for trends estimation has measureable impact on the value itself. Similar is the situation for regional flux trends. Recently, trends in CO_2 exchange over the Southern Ocean (SO) have drawn considerable attention (see LeQuere et al., 2007 and references therein). Their analysis also use results from an atmospheric-CO_2 inversion that employs independent technique and derives fluxes at forward model grid resolution (Rodenbeck, 2005). Our model results also suggest a decrease in SO CO_2 sink in the past 2.5 decades but the magnitude of net decrease can be debated and vary between 0.04-0.1 Pg-C/decade depending on period of the fits, and appears to follow the trends in AAO (Fig. 7c). More detailed look in to the fluxes corresponding to northern (40–60˚S) and southern (60–80˚S) parts of SO suggests that the former region tending to become a weaker sink of CO_2 (Fig. 7d), where the biological uptake is prominent. In contrast, the net release from southern part indicates a decrease over our analysis period where the sea-air CO_2 exchange is believed to be controlled by coastal upwelling.

Greater flux anomalies estimated using 64-region inverse model and observations at 87-stations have generated curiosity in the scientific community (e.g., McKinley et al., 2006). The flux variability for total land and ocean show good correspondence with ENSO cycle and vary in opposite phase with each other (Fig. 7a, b). The amplitude and phase correspondence weakens for total ocean flux variability if atmospheric-CO_2 data at smaller num-

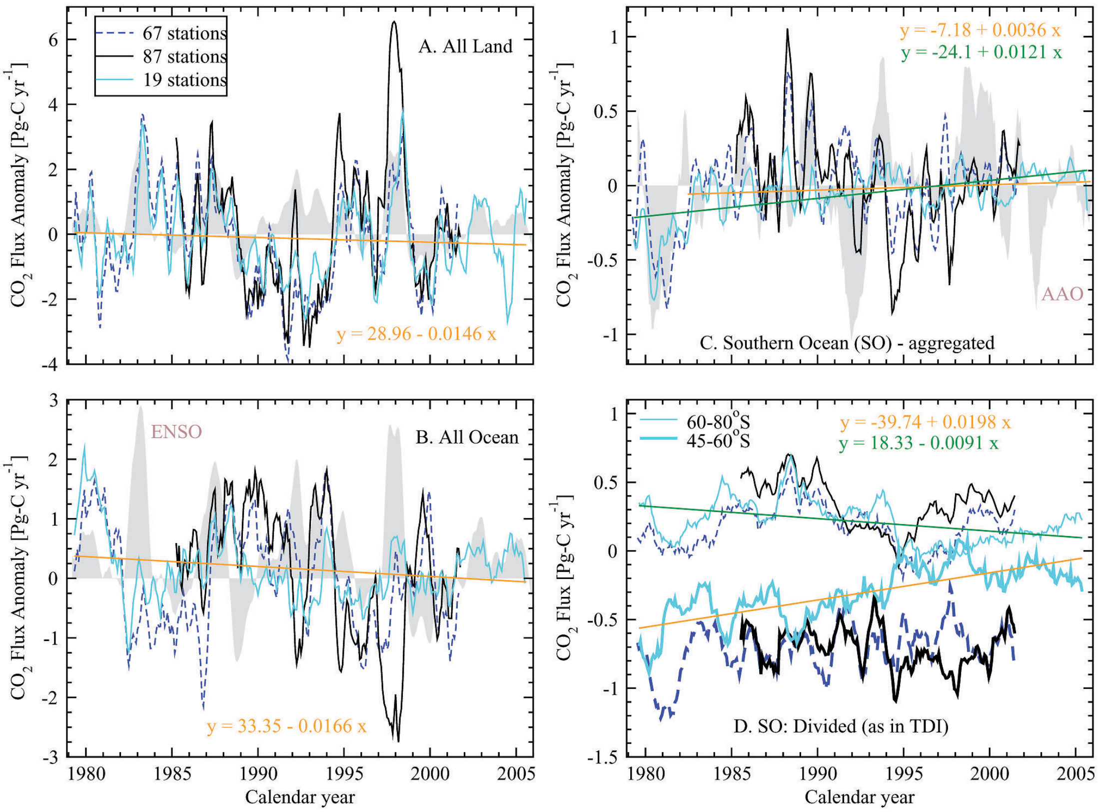

Fig. 7 Long-term trends and inter-annual variability in global and regional in CO_2 fluxes as derived by 64-region TDI model are depicted for the period 1979-2005. The NIES/FRCGC model is used for forward transport simulations and atmospheric CO_2 data are taken from three different observation networks consisting of 87, 67 and 19 stations. Linear fits to the fluxes using 19 stations network are shown as straight lines (panels A and B: orange line, Panel C: green and orange lines for 1979–2005 and 1982–2005 periods, respectively, Panel D: green and orange lines for southern and northern SO parts, respectively). In Panel D, absolute fluxes for two SO regions as in the TDIM are shown: thick and thin lines are for northern and southern parts, respectively. Note all other panels show flux anomalies. The shaded curves are for El Niño Southern Oscillation (ENSO; source: www.cdc.noaa.gov) and Antarctic Oscillation (AAO; source: www.cpc.ncep.noaa.gov) indices.

ber of sites is used in TDIM calculation, and amplitude of total land flux variability reduces although the phase remains fairly similar. Comparison of TDI/64-IAV derived flux anomalies with the estimates based on observations have been done for some of the ocean regions (Patra et al., 2005a). Both approaches result in similar magnitudes in flux anomalies for Equatorial Pacific, North Atlantic and North Pacific. Using an ocean biogeochemical elemental cycling model, sensitivity studies indicate flux anomalies to changes in nutrient supply through dust deposition from the atmosphere can partly explain the TDI/64-IAV derived CO_2 flux anomalies (see Patra et al., 2007 for details). The full range of IAVs for the ocean regions are encompassed by the sensitivity runs selected in that analysis when the dust-iron input is varied by ten times or one-tenth.

For the land regions, analysis using a simulation setup of Biome-BGC terrestrial ecosystem model underestimated the TDI estimated flux variability (Patra et al., 2005b), and they attributed the mismatch between the two to the lack biomass burning processes in Biome-BGC model. Reliable estimates of monthly-mean CO_2 fluxes due to fires (referred to as fire CO_2 flux) for several years have now been produced based on satellite derived burned area estimates, CASA terrestrial ecosystem model based fuel load inventories and known emission factors (van der Werf et al., 2006; version GFED2). Figure 8 shows a comparison of Biome-BGC net ecosystem exchange (NEE) and fire CO_2 flux (bottom-up estimate) with that estimated by TDI/64-IAV (top-down). For most of the years, the bottom-up and top-down estimates agree very well (difference within 10%), with the exception of Boreal Asia region for the period 1999–2000 only. This comparison further enhances our confidence in the derived flux IAV in the TDI/64-IAV inversion.

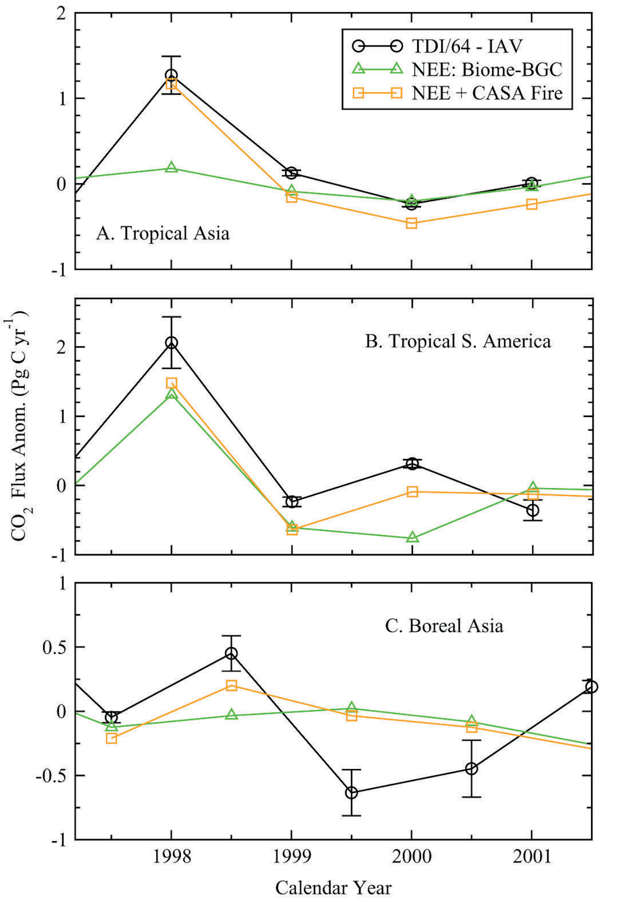

Fig. 8 The inverse modeling results for selected land regions. Biome-BGC + GFED2 fire match with TDI fluxes (observation network of 87 stations case).

6. Conclusions

Our "off-line" global atmospheric tracer transport model features a blend of established and newer approaches to representing the physical processes in the atmosphere important for atmospheric tracer transport. The semi-Lagrangian transport algorithm is combined with climatological PBL scheme and penetrative cloud convection parameterization to give a model capable of simulating the variations of the atmospheric tracers at a monthly and longer time scales. The chosen combination of the parameterizations proved to be effective in reproducing observed vertical and horizontal distributions of the passive atmospheric constituents with accuracy similar to those of the established atmospheric transport models. Test problems suite included transport of radon-222 as in WCRP transport model intercomparison experiment, sulfur hexafluoride (SF_6) following TransCom 2 model intercomparison, and CO_2 as in TransCom 1 intercomparison experiments. Vertical profiles of radon-222 are simulated successfully except for some possible underestimation of the surface concentrations in summer. The simulations of the long-lived tracers SF_6 and CO_2 demonstrated satisfactory performance in the interhemispheric transport. Strength of interhemispheric gradient in tracer transport is important for realistic estimation of sources/sinks estimation using inverse modeling of atmospheric CO_2 and satisfactory results are obtained for annual and monthly mean flux inversions. We have reviewed the CO_2 sources/sinks inversion results using a 64-region time-dependent inverse model using atmospheric CO_2 data and NIES/FRCGC transport model driven by interannually varying meteorology. Some recent developments in capturing the interannual variations in CO_2 fluxes and short-term trends are discussed. Our model results are supported by other independent estimates. Further tests and improvements in the forward transport model design are achieved for better simulation of day-to-day and diurnal variability in the tracer concentrations. The newer model version (NIES05) uses diurnally varying PBL (3-hour interval), and 6-hourly pressure level meteorological parameters (U, V, T etc.). This model is run at one of the finest horizontal resolution (0.25°×0.25°) globally and 47 layers. The finest resolution simulation shows remarkable improvements for matching the observations from a tower near to the megacity Tokyo.

Acknowledgment

We are grateful to H. Akimoto and G. Inoue for supporting this research at FRCGC and NIES. The global meteorological analysis data were provided by the ECMWF, NASA/GSFC DAO, and NCEP/NCAR. Authors thank M. Heimann for providing information on TM2 model design that facilitated development of our cumulus parameterization scheme. This work is benefited from discussions with S. Taguchi and Y. Takayabu. Thanks are due to the reviewers for useful comments to improve the manuscript.

References

[1] H. Akimoto, S. Maksyutov, and H. Ueda, Three-dimensional numerical model of atmospheric pollutant transport and transformation. - In: *Proc. 2-nd Symposium of Supercomputer Society*, Tokyo, Nov. 1992, CRC Research Institute, pp.18–23, 1993.

[2] D. F. Baker, et al., TransCom 3 inversion intercomparison: Impact of transport model errors on the interannual variability of regional CO_2 fluxes, 1988–2003, *Global Biogeochem. Cycles*, vol.**20**, GB1002, 2006.

[3] B. Bolin and C.D. Keeling, Large scale atmospheric mixing as deduced from seasonal and meridional variations of the atmospheric carbon dioxide, *J. Geophys. Res.*, vol.**68**, pp.3899–3920, 1963.

[4] CIESIN, The Center for International Earth Science Information Network, Earth Institute, Columbia University,

New York (www.ciesin.columbia.edu), 2000.

[5] P. Courtier, E. Andersson, W. Heckley, J. Paillex, et al., The ECMWF implementation of the three-dimensional variational assimilation (3D-Var), I, Formulation, *Quart. J. Roy. Meteor. Soc*., vol.**124**, pp.1783–1807, 1998.

[6] A. S. Denning, D. A. Randall, Collatz, and P. J. Sellers, Simulations of terrestrial carbon metabolism and atmsopheric CO_2 in a general circulation model, Part 2: Simulated CO_2 concentrations, *Tellus*, vol.**48B**, pp.8543–8567, 1996.

[7] A. S. Denning, M. Holzer, K. R. Gurney, M. Heimann, et al., Three-dimensional transport and concentration of SF_6: A model intercomparison study (TransCom 2), *Tellus*, vol.**51B**, pp.266–297, 1999.

[8] F. Dentener, J. Feichter and A. Jeuken, Simulation of the transport of Rn222 using on-line and off-line global models at different horizontal resolutions: a detailed comparison with measurements, *Tellus*, vol.**51B**, pp.573–602, 1999.

[9] ECMWF, ECMWF/WCRP Level III-A Global Atmospheric Data Archive, ECMWF (http://www.ecmwf.int), 1999.

[10] L. S. Geller, J. W. Elkins, J. M. Lobert, A. D. Clarke, D. F. Hirst, J. H. Butler and R. C. Meyers, Tropospheric SF_6: Observed latitudinal distribution and trends, derived emissions and interhemispheric exchange time. *Geophys. Res. Lett*., vol.**24**, pp.675–678, 1997.

[11] G. Grell, J. Dudhia, and D. Stauffer, A Description of the Fifth-Generation Penn State/NCAR Mesoscale Model (MM5), *NCAR/TN-398*, pp.122, 1995.

[12] S. Gold, H. Barkhau, W. Shleien, and B. Kahn, Measurement of naturally occurring radionuclides in air. In: *The natural radiation environment*, edited by J.A.S. Adams and W.M.Lowder, Univ. of Chicago Press, Chicago, Ill., pp.369–382, 1964.

[13] K. R. Gurney, R. M. Law, P. J. Rayner, and A. S. Denning, TransCom-3 experimental protocol, *Paper No. 707*, Dept. Atmos. Sci., Colo. State Univ., 2000.

[14] K. R. Gurney and Transcom3 modellers, Towards robust regional estimates of CO_2 sources and sinks using atmospheric transport models, *Nature*, vol.**415**, pp.626–630, 2002.

[15] K. R. Gurney and Transcom3 modellers, TransCom-3 CO_2 inversion intercomparison: 1. Annual mean control results and sensitivity to transport and prior flux information, *Tellus*, vol.**55B**, pp.555–579, 2003.

[16] K. R. Gurney and Transcom3 modellers, Transcom 3 inversion intercomparison: Model mean results for the estimation of seasonal carbon sources and sinks, *Global Biogeochem. Cycles*, vol.**18**, GB1010, 2004.

[17] J. J Hack, B. A. Boville, B. P. Briegleb, J. T. Kiehl, P. J. Rasch, and D. L. Williamson, *Description of the NCAR community climate model (CCM2)*, NCAR/TN-382, pp.108, 1993.

[18] M. Heimann and C. D. Keeling, A three dimensional model of atmospheric CO_2 transport based on observed winds: 2. Model description and simulated tracer experiments. In: *Aspects of Climate Variability in the Pacific and the Western Americas*, Ed. D. H. Peterson, American Geophysical Union, Washington DC, pp.237–275, 1989.

[19] M. Heimann, The TM2 tracer model, model description and user manual, *DKRZ Report*, *No.10*, Hamburg, pp.47, 1995.

[20] R. Hein, P. J. Crutzen, and M. Heimann, An inverse modeling approach to investigate the global atmospheric methane cycle, *Global Biogeochem Cycles*, vol.**11**, pp.43–76, 1997.

[21] D. J. Jacob, M. J. Prather, S. C. Wofsy, and M. B. McElroy, Atmospheric distribution of ^{85}Kr simulated with a general circulation model, *J. Geophys. Res*., vol.**92**, pp.6614–6626, 1987.

[22] D. Jacob, M. J. Prather, P. J. Rasch, R.-L. Shea et al., Evaluation and intercomparison of global transport models using ^{222}Rn and other short-lived tracers., *J. Geophys. Res*. vol.**102**, no.D5, pp.5953–5970, 1997.

[23] M. A. Kritz, J.-C. Le Roulley, and E. F. Danielsen, The China Clipper, Fast advective transport of radon-rich air from the Asian boundary layer to the upper troposphere near California, *Tellus*, vol.**42B**, pp.46–61, 1990.

[24] G. Lambert, G. Polian, B. Ardouin, J. Renault, and Y. Balkanski, *CFR Database of ^{222}Rn, ^{220}Rn and ^{210}Pb in Subantarctic and Antarctic atmosphere*, Centre des Faibles Radioactiv., Gif-sur-Yvette, France, 1995.

[25] R. Law, P. Rayner, A.S. Denning, D. Erickson, et al., Variations in the modelled atmospheric transport of carbon dioxide and its consequences for CO_2 inversions, *Global Biogeochem. Cycles*, vol.**10**, pp.783–796, 1996.

[26] R. M. Law and Transcom3 modellers, TransCom 3 CO_2 inversion intercomparison: 2. Sensitivity of annual mean results to data choices, *Tellus*, vol.**55B**, pp.580–595, 2003.

[27] R. M. Law, W. Peters, and C. Rödenbeck, Protocol for TransCom continuous data experiment, *Purdue Clim. Change Res. Center Tech. Rep*., (www.purdue.edu; path:/transcom/pdf/transcom/protocol_v5.pdf), 2006.

[28] C. Le Quéré, C. Rödenbeck, E. T. Buitenhuis, T. J. Conway, R. Langenfelds, A. Gomez, C. Labuschagne, M. Ramonet, T. Nakazawa, N. Metz, N. Gillett, and M. Heimann, Weakening of the Southern Ocean sink of CO_2, *Science*, vol.**316**, 2007.

[29] I. Levin and V. Hesshaimer, Refining of atmospheric transport model entries by the globally observed passive tracer distributions of ^{85}Kr and sulfur hexafluoride (SF_6), *J. Geophys. Res*., vol.**101**, pp.16745–16755, 1996.

[30] M. Maiss, L. P. Steele, R. J. Francey, P. J. Fraser, R. L. Langefelds, N. B. A. Trivett, and I. Levin, Sulfur hexafluoride – a powerful new atmospheric tracer, *Atmos. Environ.*, vol.**30**, pp.1621–1629, 1996.

[31] N. M. Mahowald, R. G. Prinn, and P. J. Rasch, Deducing CCl_3F emissions using an inverse method and a chemical

transport model with assimilated winds, *J. Geophys. Res.*, vol.**102**, pp.28127–28138, 1997.

[32] S. Maksyutov, Short-term simulations of atmospheric methane concentrations with a global tracer transport model. In: *International Symposium on Global Cycles of Atmospheric Greenhouse Gases*, Sendai, Japan, pp.333–336, 1994.

[33] S. Maksyutov and G. Inoue, Vertical profiles of radon and CO_2 simulated by the global atmospheric transport model. In: *CGER Supercomputer activity report*, *CGER-I039–2000*, CGER NIES, Tsukuba, Japan, vol.**7**, pp.39–41, 2000.

[34] S. Maksyutov, D. Fujita, T. Saeki, and T. Nakazawa, Tracer transport model validation and model-simulated CO_2 cycle over continents, *EOS Trans.*, vol.**81**, no.48, *AGU Fall Meet. Suppl.*, abstract B21F-08, 2000.

[35] S. Maksyutov, P. K. Patra, and G. Inoue, Pseudo-data inversion of column-CO_2 observations by remote sensing using a high resolution inverse model, *Int. Archives of Photogrammetry*, *Remote Sensing and Spatial Inform. Sci.*, *Vol.XXIV*, Part. 7/W14, 2003a.

[36] S. Maksyutov, T. Machida, H. Mukai, P. K. Patra, T. Nakazawa, G. Inoue, and TransCom-3 modelers, Effect of recent observations on Asian CO_2 flux estimates with transport model inversions, *Tellus*, vol.**55**, no.2, pp.522–529, 2003b.

[37] G. Marland, Fossil fuels CO_2 emissions: Three countries account for 50% in 1986 - In: *CDIAC Communications*, Winter 1989, pp.1–4, 1989.

[38] G. A. McKinley, et al., North Pacific carbon cycle response to climate variability on seasonal to decadal timescales, *J. Geophys. Res.*, vol.**111**, C07S06, 2006.

[39] P. K. Patra and S. Maksyutov, Incremental approach to the optimal network design for CO_2 surface source inversion, *Geophys. Res. Lett.*, vol.**29**, no.10, 1459, 2002.

[40] P. K. Patra, S. Maksyutov, and TransCom-3 modelers, Sensitivity of Optimal Extension of CO_2 Observation Networks to Model Transport, *Tellus*, vol.**55**, no.2, pp.498–511, 2003a.

[41] P. K. Patra, S. Maksyutov, Y. Sasano, H. Nakajima, G. Inoue, and T. Nakazawa, An evaluation of CO_2 observations with Solar Occultation FTS for Inclined-Orbit Satellite sensor for surface source inversion, *J. Geophys. Res.*, vol.**108**, no.D24, 4759, 2003b.

[42] P. K. Patra, M. Ishizawa, S. Maksyutov, T. Nakazawa, and G. Inoue, Role of biomass burning and climate anomalies for land-atmosphere carbon fluxes based on inverse modeling of atmospheric CO_2, *Global Biogeochem. Cycles*, vol.**19**, GB3005, 2005a.

[43] P. K. Patra, S. Maksyutov, M. Ishizawa, T. Nakazawa, T. Takahashi, and J. Ukita, Interannual and decadal changes in the sea-air CO_2 flux from atmospheric CO_2 inverse modelling, *Global Biogeochem. Cycles*, vol.**19**, GB4013, 2005b.

[44] P. K. Patra, S. Maksyutov, and T. Nakazawa, Analysis of atmospheric CO_2 growth rates at Mauna Loa using inverse model derived CO_2 fluxes, *Tellus*, vol.**57B**, pp.357–365, 2005c.

[45] P. K. Patra and Transcom3 modellers, Sensitivity of inverse estimation of annual mean CO_2 sources and sinks to ocean-only sites versus all-sites observational networks, *Geophys. Res. Lett.*, vol.**33**, L05814, 2006a.

[46] P. K. Patra, S. E. Mikaloff-Fletcher, K. Ishijima, S. Maksyutov, and T. Nakazawa, Comparison of CO_2 fluxes estimated using atmospheric and oceanic inversions, and role of fluxes and their interannual variability in simulating atmospheric CO_2 concentrations, *Atmos. Chem. Phys. Discuss.*, vol.**6**, pp.6801–6823, 2006b.

[47] P. K. Patra, J. K. Moore, N. Mahowald, M. Uematsu, S. C. Doney, and T. Nakazawa, Exploring the sensitivity of basin-scale air-sea CO_2 fluxes to interannual to decadal variability in atmospheric dust deposition using ocean carbon models and atmospheric CO_2 inversions, *J. Geophys. Res.*, vol.**112**, G02012, 2007.

[48] N.A. Philips, A coordinate system having some special advantages for numerical forecasting, *J. Meteorol.*, vol.**14**, pp.184–185, 1957.

[49] P. Pochanart, H. Akimoto, S. Maksyutov, and J. Staehelin, Surface ozone at the Swiss alpine site Arosa: the hemispheric background and the influence of the large scale atmospheric emissions, *Atmos. Environ.*, vol.**35**, pp.5553–5566, 2001.

[50] M. Prather, M. McElroy, S. Wofsy, G. Russel, and D. Rind, Chemistry of the global troposphere: Fluorocarbons as tracers of air motion, *J. Geophys. Res.*, vol.**92**, pp.6579–6613, 1987.

[51] P. J. Rasch, B. A. Boville, and G. P. Brasseur, A three-dimensional general circulation model with coupled chemistry for the middle atmosphere, *J. Geophys. Res*, vol.**100**, pp.9041–9071, 1995.

[52] A. R. Ravishankara, S. Solomon, A. A. Turnispeed, and R. F. Warren, Atmospheric lifetimes of long-lived halogenated species, *Science*, vol.**259**, pp.194–199, 1993.

[53] P. J. Rayner, I. G. Enting, R. J. Francey, and R. Langenfelds, Reconstructing the recent carbon cycle from atmospheric CO_2, $\delta^{13}C$ and O_2/N_2 observations, *Tellus*, vol.**51B**, pp.213–232, 1999.

[54] C. Rödenbeck, Estimating CO_2 sources and sinks from atmospheric mixing ratio measurements using a global inversion of atmospheric transport, *Max-Planck-Institute for Biogeochemistry*, *Tech. Rep. 6*, P.O. Box 100164, 07701 Jena, Germany, 2005 (http://www.bgc-jena.mpg.de;path: /mpg/websiteBiogeochemie/Publikationen/Technical_Reports/tech_report6.pdf).

[55] S. Schubert, R. Rood, and J. Pfaendtner, An assimilated

dataset for Earth science applications, *Bull. Am. Meteorol. Soc*., vol.**74**, pp.2331–2342, 1993.

[56] S. Taguchi, A three-dimensional model of atmospheric CO_2 transport based on analyzed winds: model description and simulation results for TRANSCOM, *J. Geophys. Res*., vol.**101**, pp.15099–15109, 1996.

[57] T. Takahashi, S. C. Sutherland, C. Sweeney, A. Poisson, N. Metzl, B. Tilbrook, N. Bates, R. Wanninkhof, R. A. Feely, C. Sabine, J. Olafsson, and Y. Nojiri, Global sea-air CO_2 flux based on climatological surface ocean pCO_2, and seasonal biological and temperature effects, *Deep-Sea Research Part II*, vol.**49**, pp.1601–1622, 2002.

[58] P. Tans, I. Fung, and T. Takahashi, Observational constraints of the global atmospheric CO_2 budget, *Science*, vol.**247**, pp.1431–1438, 1990.

[59] M. Tiedtke, A comprehensive mass flux scheme for cumulus parameterization in large-scale models, *Mon. Wea. Rev*., vol.**117**, pp.1779–1800, 1989.

[60] Y. Tohjima, H. Mukai, S. Maksyutov, Y. Takahashi, T. Machida, M. Utiyama, M. Katsumoto, and Y. Fujinuma, Variations in atmospheric nitrous oxide observed at Hateruma monitoring station, *Chemosphere-Global Change Science*, vol.**2**, pp.435–443, 2000.

[61] Y. Tohjima, T. Machida, M. Utiyama, M. Katsumoto, Y. Fujinuma, S. Maksyutov, Analysis and presentation of in situ atmospheric methane measurements from Cape Ochiishi and Hateruma Island, *J. Geophys. Res*., vol.**107**, no.D12, 4148, 2002.

[62] G. R. van der Werf, J. T. Randerson, L. Giglio, G. J. Collatz, P. S. Kasibhatla, and A. F. Arellano Jr, Interannual variability in global biomass burning emissions from 1997 to 2004, *Atmos. Chem. Phys*., vol.**6**, pp.3423–3441, 2006.

[63] WDCGG, WMO World Data Centre for Greenhouse Gases, Japan Meteorological Agency, Tokyo (http://gaw.kishou.go.jp), 2007.

[64] W. M. Washington and C. L. Parkinson, *An introduction to three-dimensional climate modeling*, Oxford University Press, New York, pp.422, 1986.

[65] D.L. Williamson and P. J. Rasch, Two-Dimensional Semi-Lagrangian Transport with Shape Preserving Interpolation, *Mon. Wea. Rev*., vol.**117**, pp.102–129, 1989.

[66] D.L. Williamson and R. Laprise, Numerical approximations for global atmospheric GCMs – In: *Numerical modeling of global atmosphere in the climate system*. Ed. P. Mote and A. O'Neil, NATO Science Series, Kluwer Academic Publishers, Series C, vol.**550**, pp.127–220, 2000.

[67] P. H. Zimmermann, J. Feichter, H. K. Rath, P. J. Crutzen, and W. Weiss, A global three-dimensional source-receptor model investigation using ^{85}Kr, *Atmos. Environ*., vol.**23**, pp.25–35, 1989.

Journal of the Earth Simulator, Volume 9, March 2008, 19–26

Internal and External Flow of Rocket Nozzle

Taro Shimizu[1]*, Masatoshi Kodera[2], and Nobuyuki Tsuboi[3]

[1] *JAXA's Engineering Digital Innovation Center, Japan Aerospace Exploration Agency, 3-1-1, Yoshinodai, Sagamihara, Kanagawa 229-8510, Japan*

[2] *Advanced Propulsion Technology Research Group, Space Transportation Propulsion Research and Development Center, Office of Space Flight and Operations, Japan Aerospace Exploration Agency, 1, Koganezawa, Kimigaya, Kakuda, Miyagi 981-1525, Japan*

[3] *Institute of Space and Astronautical Science, Japan Aerospace Exploration Agency, 3-1-1, Yoshinodai, Sagamihara, Kanagawa 229-8510, Japan*

(Received January 5, 2008; Revised manuscript accepted February 13, 2008)

Abstract The objective of this study is to clarify flow structures inside and outside a rocket nozzle, which are indispensable for actual development of rocket engine. One is the transition of the flow structure between free shock separation and restricted shock separation inside a nozzle, which would sometimes generate a destructive side-load. The transition is numerically reproduced under the experimental condition where the transition occurs. We also found a simple function to analyze the flow structure inducing transition. Another is ignition overpressure induced by engine ignition. The overpressure, which originates in shock wave, imposes high pressure load on the nozzle or rocket surface and also influence the ignition process especially under clustering (two) nozzle configuration. The numerical results show that besides an overpressure, a vortex ring is generated and propagated from the nozzle. Under clustering nozzle configuration, the interaction between the overpressure waves and the vortex rings occurs between the nozzles. This makes the force acting on the nozzle asymmetric. We could estimate the side-load acting on the nozzle actuator in advance of the development and firing test.

Keywords: rocket nozzle, RSS, FSS, flow transition, ignition overpressure, RANS

1. Introduction

Understanding the phenomena of the internal and external flow of a rocket nozzle is essential for developing a highly reliable space launch vehicle. Until recently, almost all the development of Japanese rocket elements was based on trial and error, i.e. an iterative cycle of trial design and experimental verification. However, in a new engine development, or an engine improvement for lowering cost and high performance, sometimes latent troubles have included in many components of the rocket, which would unfortunately end in mission failure once in a while. Therefore it is obvious that we need more stores of our own knowledge for the development. Recent progress in computational fluid dynamics has changed the trial and error approach, as numerical simulation is now playing a major role in the development of rockets and rocket engines built today. Fortunately Japan leads the world in supercomputing technology, *e.g.* the Earth Simulator. However, the effective and substantial use of this technology has just begun especially in the industry. In JAXA (Japan Aerospace Exploration Agency), the CFD (Computational Fluid Dynamics) by the supercomputer plays an important role in the development because the CFD results began to provide the reliable answer for development. In other words, the simulation can explain or reproduce the real phenomena. As a result, the role of the simulation is changing; from just a reference of the experiment to the basis of early design process. Since the full-scale experiment of the rocket element is much time and cost consuming, effective use of the CFD will contributes to the development. We think that it gives a hope to complement the luck of experience and limited budget.

In this study, two simulation results are presented, which could contribute to the actual development. One is the verification of the origin of the large side-load at a nozzle, which occurs during the development of the LE-7A engine. Another is on the newly developing H-IIB rocket, which has two liquid engines for the first time in Japan.

* ***Corresponding author***: *Taro Shimizu, JAXA's Engineering Digital Innovation Center, Japan Aerospace Exploration Agency, 3-1-1, Yoshinodai, Sagamihara, Kanagawa 229-8510 Japan. E-mail: shimizu.taro@jaxa.jp*

Estimating the difference of flow fields between single and clustering nozzle configurations is very important issue.

2. Numerical method

A numerical method of solving the Navier-Stokes equations on the hybrid unstructured grid was developed using a finite-volume cell vertex scheme and the LU-SGS implicit time integration algorithm [1, 2]. Figure 1 presents the unstructured grid distribution near the LE-7A original nozzle. The Goldberg -Ramakrishnan model was used to evaluate the turbulent kinetic viscosity, and the Venkatakrishnan limiter function was used to enhance the convergence. In some unsteady calculations, Newtonian sub-iteration was implemented based on the Crank-Nicholson method to ensure time accuracy up to the second order. In order to take the O/F (mixture ratio; mass ratio of oxidizer to fuel) effect into account, the adopted code should treat the properties of gas mixture that consists of multi chemical species. Therefore, the code incorporates the standard finite reaction rate model for the H_2-O_2 reaction including nine species (H_2, O_2, H_2O, H, HO_2, OH, O, H_2O_2, and N_2). The calculation was performed using the Earth Simulator of the Japan Agency for Marine-Earth Science and Technology (JAMSTEC).

3. Transition of the flow structure

Design of a nozzle contour is one of the major factors for an effective rocket engine. Therefore optimization of the nozzle contour has been conducted to obtain maximum thrust under the limits of the whole engine system. So far various kinds of design methods are developed based on classical nozzle design methods, such as conical, parabolic and truncated perfect nozzles, only to increase steady performance [3-5]. However it is also known that such high performance nozzle sometimes causes a large side-load and high thermal stress on the nozzle wall during the transient of the operation. These would induce serious launch problems and also destroy engine hardware in sea-level tests. Therefore the unsteady behavior of the flow structure should be considered in the design process. In order to avoid the destructive side-load, a great deal of work has been done experimentally and numerically to clarify the origin of the side-load generation [6-8]. Inside the thrust optimized and parabolic nozzles, an internal shock is generated by the nozzle contour. This internal shock, usually generated from the throat of the nozzle, forms an inverse Mach reflection at the centerline downstream of the throat, enhancing the momentum of the flow toward the nozzle wall. Therefore, the transition of the flow structure, from FSS (free shock separation) to RSS (restricted shock separation or attached flow) and vise versa, could occur and create the sudden change of the pressure distribution on the nozzle wall, generating the side-load [7, 8].

In developing the LE-7A engine of the Japanese H-IIA launch vehicle, we were faced with a side-load originating in the transition of the flow structure during the start-up and shut-down transients [9-12]. Actually, the nozzle was initially designed as a compressed truncated perfect nozzle (CTP nozzle) which is different from any other nozzles developed. Therefore the study has begun to investigate the origin of this undesired phenomenon. In the start-up and shut-down transient, the O/F is fluctuating sharply in the actual operation. Although the nominal value for the O/F designed for the steady condition is about 6 (hydrogen rich), the transient value can be from 3 to 8 for a short period of time. The subscale experiment [10, 11] demonstrated it is shown that the flow transition from FSS to RSS is likely to occur with a lower O/F than the designed value. Therefore, the start-up transient flow structures for O/F's corresponding to 6 and 3 are investigated in detail. The transition mechanism is explained by analyzing the flow properties that are difficult to obtain by experiment alone.

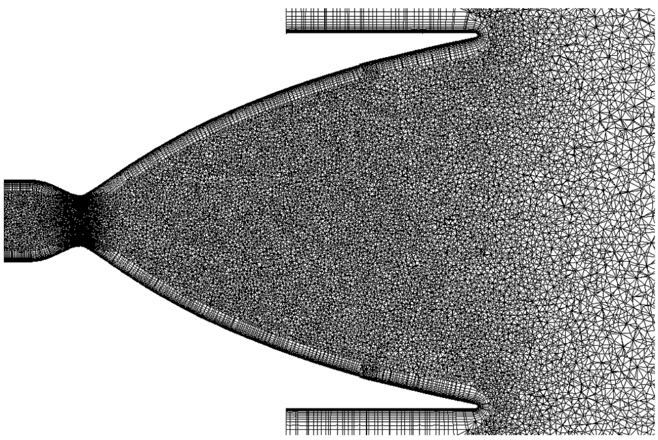

Fig. 1 Unstructured grid distribution on a symmetric plane for LE-7A original nozzle.

Here we briefly explain the numerical settings. The boundary condition of the nozzle inlet is as follows. The reaction of the fuel, H_2 and the oxidizer, O_2, is assumed to be completed upstream of the nozzle inlet (in the combustion camber) under a prescribed mixture ratio. Therefore, H_2O and H_2 flow into the nozzle with a given total temperature and total pressure (only if O/F is less than 8, which corresponds to the stoichiometric ratio). This simplified frozen chemistry model is used mainly for reducing CPU time. However, we conducted preliminary axis-symmetric simulations for non-equilibrium chemistry and found that there was no major difference in the Mach isolines inside the nozzle between the non-equilibrium and the frozen calculation. Therefore, we simplify the inlet condition mentioned above. Initially, inside the nozzle and the surroundings are filled with the standard air ($T = 300K$, $P_a = 0.1MPa$). Throughout the calculation, the temperature of the nozzle wall is assumed to be 700K which roughly corresponds to the actual operation.

3.1 Reproduction of the flow transition

Figures 2 and 3 present the snapshot of flow fields showing the FSS and the transition to RSS structure respectively. Here we define the nozzle pressure ratio,

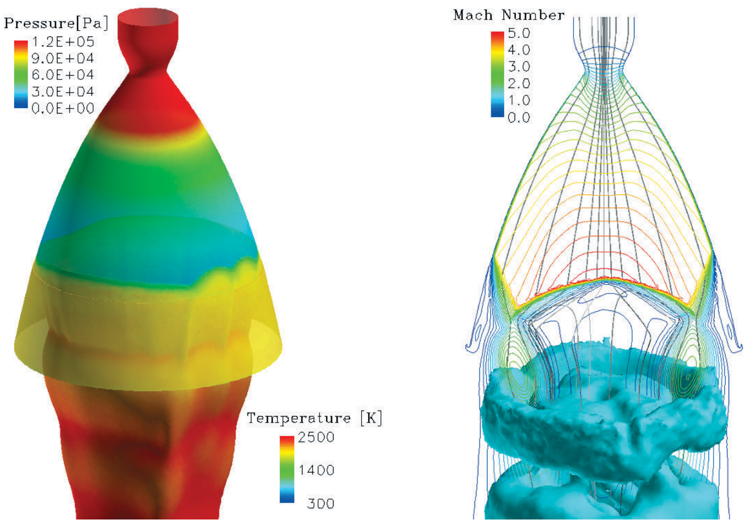

Fig. 2 FSS flow structure. NPR = 52. O/F = 6.
Wall pressure and temperature on the iso-surface where mass fraction of $H_2O = 0.6$ (left figure). Mach number and large vortical structure (second invariant of velocity gradient tensor) together with stream lines (right figure).

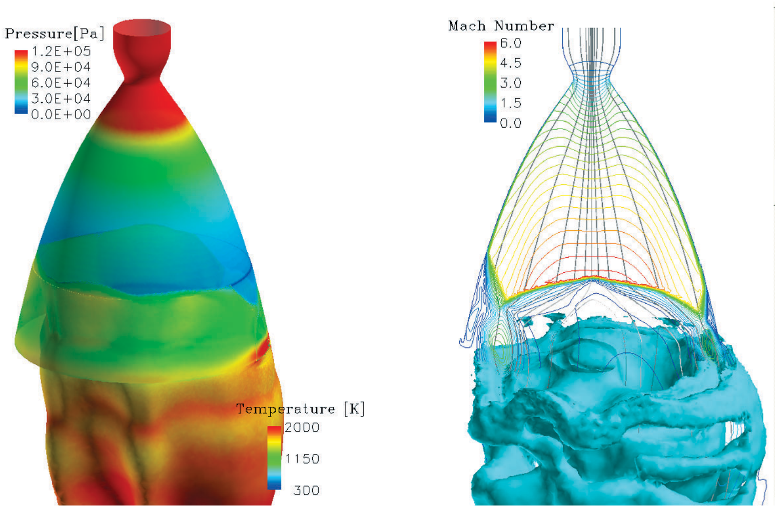

Fig. 3 Transition to RSS flow structure. NPR = 52. O/F = 3.
Wall pressure and temperature on the iso-surface where mass fraction of $H_2O = 0.6$ (left figure). Mach number and large vortical structure (second invariant of velocity gradient tensor) together with stream lines (right figure).

NPR = P_c / P_a, where P_c is the chamber pressure. The rate of the pressure increment is set about 0.05 [NPR / msec], which is of the same order as in real operation of this range. When O/F = 6 (Fig. 2), the separation line remains nearly symmetric (throughout all transient state). The wall pressure behind the separation line remains at ambient pressure. This means the hot combustion gas is apart from the nozzle wall. Mach isolines also indicate the flow has FSS structure. The vortical structure represents that the downstream of the nozzle exit, there generates series of stable symmetrical vortex rings as NPR increases. When O/F=3 (Fig. 3), the region between the supersonic jet and the wall narrows. In this region, aspired inflow of ambient air is accelerated, resulting in decreased wall pressure (the green part of the nozzle wall pressure upstream of the nozzle exit). Since the separation shock location is determined to balance the pressure gap, once the wall pressure downstream is decreased, the corresponding part of the separation line moves downstream inducing a further decrease in wall pressure. Thus, part of the deformed separation line moves downstream suddenly, generating the recirculation bubble and RSS flow structure shown in right part of the nozzle wall (observed as in wall pressure and Mach isolines). The imbalance of the circumferential pressure distribution (the different flow structure between FSS and RSS) generates a large side-load. The vortical structure downstream of the nozzle exit becomes asymmetric indicating that the flow is unsteady and unstable. A comparison of the magnitude of side loads between calculated and measured is conducted. The magnitude of the calculated side-load is 120 kN when O/F = 3, which is in accord with the firing test (75~100 kN). Although a slight distortion of the separation line is observed when O/F = 6, the supersonic jet stays away from the nozzle wall (Fig. 2). Therefore, the magnitude of the calculated side-load is 20 kN. The agreement between the simulation and the experiment in the NPR where the large side-load occurs and the O/F at which the transition from FSS to RSS is obtained is reasonably good (NPR = 35~59 and O/F = 2.8~4.1 in the subscale experiment) [10]. Therefore it is shown both in CFD and experiment that the O/F, in other words, the ratio of specific heat has an essential effect on the flow transition.

3.2 Detection of the fine flow structure

Next, we investigate the obtained flow structure in detail to find some design standard. This is particularly important for the actual development process where the large simulations conducted here are not usually applicable. It is known that inside thrust optimized and parabolic nozzles, an internal shock is generated from the throat and an inverse Mach reflection at the centerline downstream of the throat forms a cap shock structure. Thus, the momentum of the flow toward the nozzle wall increases, hence pushing the supersonic jet toward the nozzle wall resulting in the generation of RSS flow. However, little is known about a CTP nozzle studied here. In particular, although the cap shock structure is observed independent of the O/F, it is not clear whether the bending contour of the Mach number corresponds to the existence of an internal shock wave, which is characteristic of thrust optimized and parabolic nozzles. Therefore, using the shock function [13], we first investigate whether an internal shock exists. The shock function is defined as follows:

$$f(\mathbf{x}) \equiv \frac{\mathbf{u}}{\mathrm{c}} \cdot \frac{grad\,\mathrm{p}}{|grad\,\mathrm{p}|},$$

where $\mathbf{u}$ is the velocity, c is the acoustic speed and p is the pressure. This function represents the Mach number ($\mathbf{u}/c$) of the velocity component perpendicular to the pressure discontinuity. Therefore, if a shock wave exists, the function changes from greater than 1 upstream to less than 1 downstream. We applied this function to the obtained flow field. However, no shock wave is detected around the bending Mach contour inside nozzle. Compression waves generated from the wall contour downstream of the initial expansion (circular arc) may coalesce into a shock wave depending on the compression ratio of the truncated perfect nozzle. We believe that for the CTP nozzle studied here, the internal shock wave, if existed, is too weak to be detected by the shock function under the mesh size used. Therefore it is necessary to investigate in detail the compression and expansion in the flow fields for understanding the difference of flow structures with varying O/F. Here, we introduce the compression function defined below [14]:

$$C(\mathbf{x}) \equiv \frac{grad\,\mathrm{p}}{\mathrm{p_c}} \cdot \frac{\mathbf{u}}{|\mathbf{u}|}.$$

This function becomes positive (negative) when the pressure increases (decreases) along a stream line. Note that this function has a dimension (1/m). Figure 4 shows the compression function applied for steady full flow condition (NPR = 124). The blue part indicates the expansion region where the flow is efficiently expanded by the nozzle. The red part including the shock wave which can be detected by the shock function, indicates the region where the flow is not expanded or accelerated efficiently. A strong correlation is observed between this low-expansion region and the contour of the Mach number. The concentrated and bending contour corresponds closely to the low-expansion region (thin triangular red region). By this

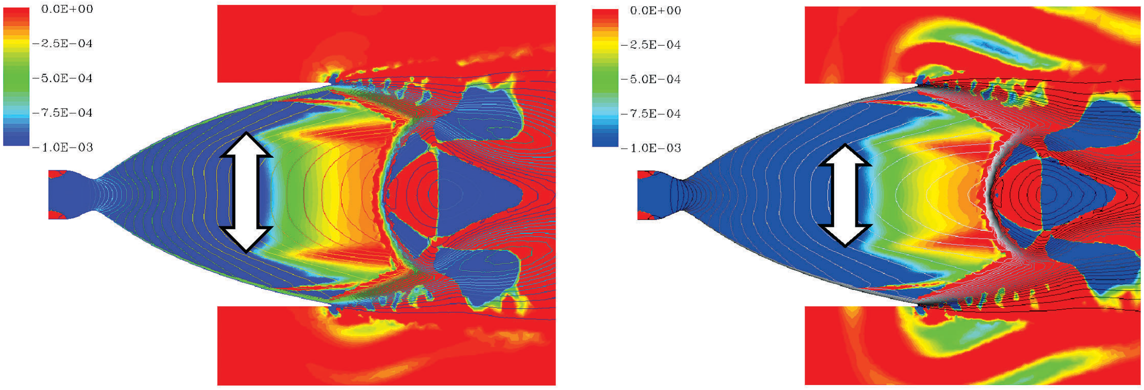

Fig. 4 Compression function [1/m] and Mach number distribution (contours), O/F = 3 (left figure). O/F = 6 (right figure).

low-expansion region, we can roughly know the internal core, where the contour of the Mach number becomes nearly perpendicular to the nozzle axis, and the outer region bounded by the separation shock from the nozzle wall. When O/F = 3, the internal core becomes broad radially. Therefore, the curvature of the Mach isolines is small. This results in a small curvature of the cap shock downstream. It is quite natural that the curvatures are similar because the shock wave is formed to balance the flows passing through the shock wave itself. Another notable point is that the radial widths of the outer boundary of the low-expansion region and the end of the cap shock downstream are nearly identical. Since there is no precise theory to describe the Mach reflection or the oblique shock in an axis-symmetric flow configuration, it is very difficult to analytically explain the flow structure inside a nozzle. However, it is worth noting that the compression function applied here reveals a strong correlation between the outer boundary radial widths of the low-expansion region and the end of the cap shock. This function captures the mild compression flow structure inside the nozzle where an internal shock is not detected and helps to understand the flow transition between FSS and RSS without conducting unsteady simulation.

The present nozzle design for LE-7A engine is classical truncated perfect nozzle which is considered to be the most robust nozzle design, but not to have highest performance. Therefore there is room for developing a high performance nozzle without undesired unsteady phenomena in the future.

4. Generation of the overpressure in the start-up transient of the rocket engine

The H-IIB launch vehicle, which is an upgraded version of the current H-IIA launch capacity, is under development (Fig. 5). The H-IIB launch vehicle has two major purposes. One is to launch the H-II Transfer Vehicle (HTV) to the International Space Station (ISS). The other is to respond to broader launch needs by making combined use of both H-IIA and H-IIB launch vehicles. To obtain larger launch capability, the H-IIB has clustering (two) liquid rocket

Fig. 5 Schematic of newly developing H-IIB launch vehicle. The clustered LE-7A are installed as the first stage engine.

engines (LE-7A) in the first-stage, instead of one for the H-IIA. The efficient development is expected based on the use of the knowledge obtained so far.

Since this is for the first time in Japanese rocket having two liquid rocket engines clustered, the estimation of the difference of flow fields between single and clustering nozzle configurations is very important. In this study, the generation of the large pressure disturbance at the start-up transient, called ignition overpressure is numerically investigated in detail, which is one of the concerns on the modifications. The ignition overpressure is originally well recognized in solid rocket booster [15-17]. However, since the two liquid engines are designed to be located very close, the mutual influence of pressure disturbances and flow structure around nozzles should be investigated in detail.

First, the flow under original single nozzle configuration is simulated for verification (not shown here). The numerical method is the same as the previous section except that the mass fractions of the each species are obtained from the chemical equilibrium calculation. The transient operation is modeled as follows. The total pressure is linearly increased from the atmospheric pressure to the first peak of the chamber pressure (2.6MPa), where the influence of the overpressure is almost disappeared. The total temperature is set 3560K throughout the calculation which corresponds to the chemical equilibrium state of the chamber. The rate of the pressure increase is set about 1 [NPR/msec] which is the same as the actual operation. The result shows that at the start-up transient, an overpressure and a vortex ring are generated and propagated downstream from the nozzle. As the NPR increases, the overpressure arrives at the nozzle tip decreasing its amplitude, and then propagates nearly spherically from the nozzle. At the same time, vortex ring is made by the shear and impulse, which propagates downstream of the nozzle. The tip wall pressure is compared with the experiment for verification of the simulation. The positive pressure disturbance (from the atmospheric pressure) is observed first, which corresponds to the overpressure, and then the negative pressure disturbance is observed, which corresponds that the vortex core is generating, dissipating and moves downstream. The peak amplitude and the time lag between the overpressure and the vortex ring are in good agreement between CFD and experiment.

Based on this preliminary study, we estimate that when the nozzles are clustered, the pressure disturbance induced by the neighboring nozzle is 10% of the atmospheric pressure. Therefore, the influence of the disturbance is not enough to deform the separation line which induces the side-load. However, under the clustering nozzle configuration, the interaction between the overpressure waves and the vortex rings may occur especially between the nozzles. Therefore we next investigate the transient flow structure with clustered nozzle configuration.

Figure 6 shows time series of the numerical result for the simultaneous start-up. All colored contours and surfaces represent the pressure field; pressure of nozzle outside wall, iso-surface (9.0E+4 and 1.09E+5 Pascal) of the pressure and the slice of the pressure on the symmetric surface are shown. The contour for Mach number is also plotted as observed inside the nozzle. As NPR increases, the overpressure propagates outside the nozzle nearly spherically and interacts between nozzles (Fig. 6a). The weak pressure disturbance (as seen by small circle in Fig. 6a.) is the weak sound propagating from the wall which has initially different temperature form the ambient. It is verified that the influence is negligible by the calculation of adiabatic wall. We can also observe the generation of the vortex rings by green tori. When NPR = 9 (Fig. 6b), the interaction of the overpressure stands out and generates the positive pressure disturbances on the inner side of nozzle walls, which generates repulsive force between nozzles. Then it is found that the interaction of two vortex ring (shown as merging green tori in pressure field of Fig. 6c-d) occurs, which induces the anomalous behavior that the inner part of the interacting vortex ring propagates upstream. This irregular behavior can be understood by the motion of the two dimensional vortex pair whose magnitude of the vorticity is the same but has opposite sign. As a result, it generates negative pressure disturbances and asymmetric wall pressure distribution on each nozzle. Thus, the force acting on the nozzle becomes attractive force between nozzles this time.

Based on the result obtained, we estimate the side-load acting on the actuator of the nozzle, which is necessary for the development. Due to the symmetry of the configuration, the forces acting on the four actuators of two nozzles behave nearly the same for repulsive and attractive force mentioned above. Figure 7 shows the normalized loads acting on the four actuators of the nozzles. The negative and positive loads correspond to the repulsive and attractive force between nozzles respectively and have nearly the same amplitude. The positive load has larger time scale than the negative load, because of the slow propagating velocity for the vortex rings. It is also observed that the positive loads obtain high frequency disturbances, which originates in the jet noise generation. The peak and the frequency of the loads (about 50 Hz) are expected by this numerical result, which is taken into consideration at the early development process before the firing test.

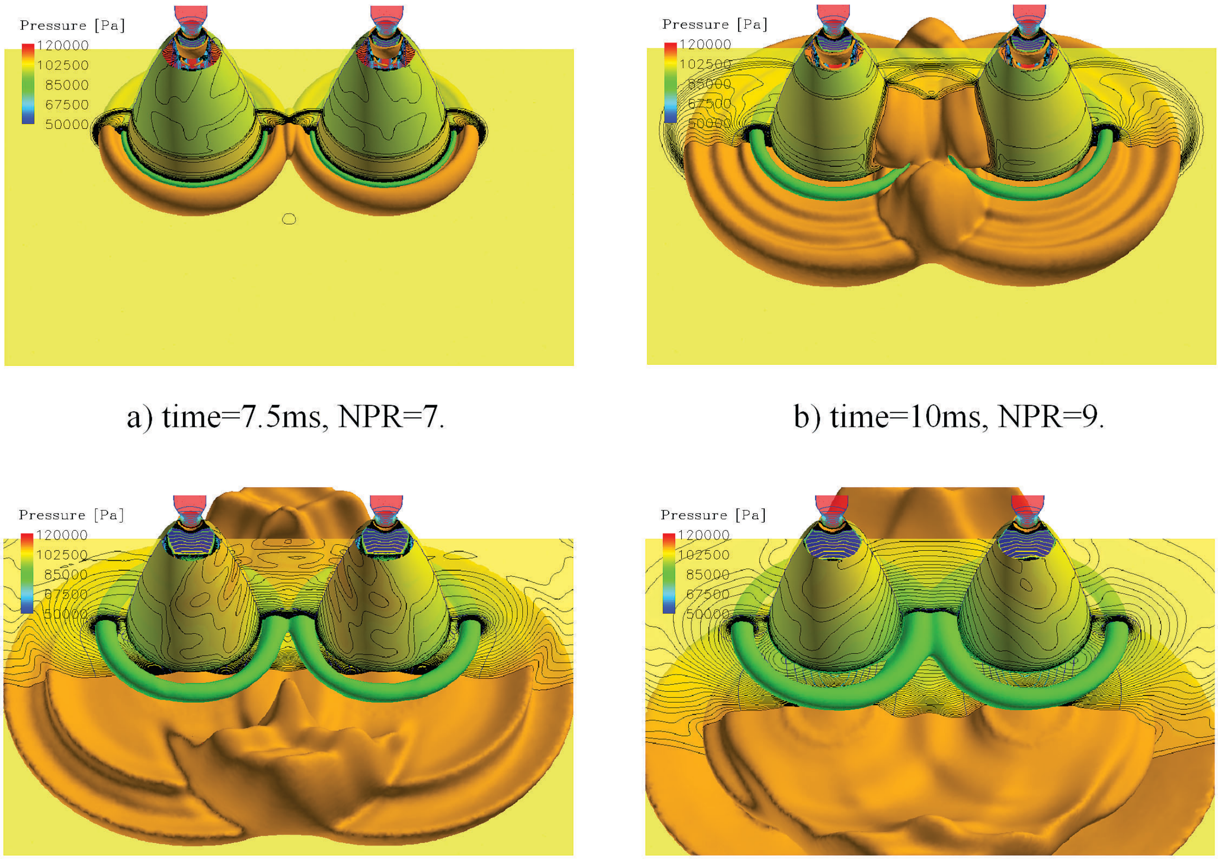

a) time=7.5ms, NPR=7.

b) time=10ms, NPR=9.

c) time=12.5ms, NPR=11.

d) time=15.0ms, NPR=13.

Fig. 6 Time series of the pressure and Mach number distributions for simultaneous start-up of H-IIB rocket.

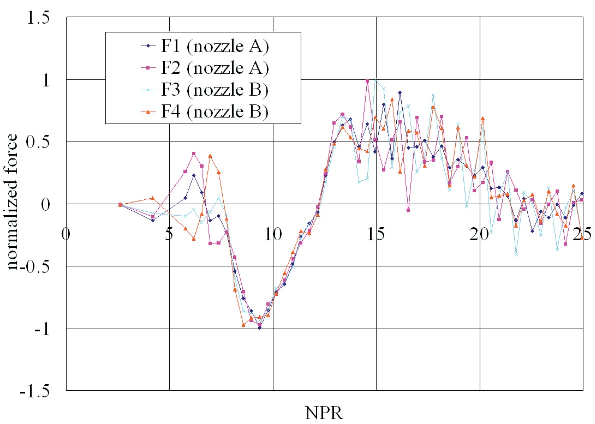

Fig. 7 Normalized loads acting on the four actuators of the nozzles.

5. Conclusions

Two simulation results were presented, that could contribute to the actual development of the rocket engines. One is the verification of the origin of the large side-load at a nozzle we have faced during the development of the LE-7A engine. The transition of the flow structure from FSS to RSS inside a nozzle was numerically reproduced and explained. The mixture ratio is the key to determining flow structure. A simple method using the compression function is proposed to capture the flow structure and understand the transition. Another is on the newly developing H-IIB rocket which has two LE-7A engines. The estimation of the difference of flow fields between single and clustering nozzle configurations is very important issue. In this study, the generation of the large pressure disturbance at the start-up transient by the interaction between ignition overpressures and vortex rings were investigated in detail. The peak and the frequency of the loads were estimated by the numerical results, which is taken into consideration at the early development process before the firing test.

(This article is reviewed by Dr. Tetsuya Sato.)

References

[1] M. Kodera, T. Sunami, and K. Nakahashi, Numerical Analysis of SCRAMJET Combusting Flows by Unstructured Hybrid Grid Method, *AIAA Paper*, 00–0886,

2000.
[2] Tohoku University Aerodynamic Simulation Code (TAS).
[3] M. J. Zucrow and J. D. Hoffman, *Gas Dynamics*, vol.**2**, John Wiley and Sons, New York, pp.160–164, 1977.
[4] G. V. R. Rao, Exhaust Nozzle Contour for Optimum Thrust, Jet Propulsion, vol.**28**, pp.377–382, 1958.
[5] J. D. Hoffman, Design of Compressed Truncated Perfect Nozzles, *Jet Propulsion*, vol.**3**, no.2, pp.150–156, 1987.
[6] L. H. Nave and G. A. Coffey, Sea Level Side Loads in High-Area-Ratio Rocket Engines, *AIAA Paper*, 73–1284, 1973.
[7] M. Frey and G. Hagemann, Restricted Shock Separation in Rocket Nozzles, *Journal of Propulsion and Power*, vol.**16**, no.3, pp.478–484, 2000.
[8] G. Hagemann, M. Frey, and W. Koschel, Appearance of Restricted Shock Separation in Rocket Nozzles, *Journal of Propulsion and Power*, vol.**18**, no.3, pp.577–584, 2002.
[9] Y. Watanabe and M. Tsuboi, LE-7A Engine Nozzle Problems during Transient Operations, *AIAA Paper*, 02–3841, 2002.
[10] T. Tomita, H. Sakamoto, M. Takahashi, M. Sasaki, T. Tamura, and M. Tsuboi, Sub-Scale Nozzle Combustion Tests of the LE-7A Engine for Clarification of Large Side-loads(I): Formation of RSS Structure Due to Combustion Condition, *AIAA Paper*, 02–3842, 2002.
[11] T. Tomita, H. Sakamoto, T. Onodera, M. Sasaki, M. Takahashi, H. Tamura, and Y. Watanabe, Experimental Evaluation of Side-load Characteristics on TP, CTP and TO nozzles, *AIAA Paper*, 04–3678, 2004.
[12] M. Takahashi, S. Ueda, T. Tomita, M. Takahashi, H. Tamura, and K. Aoki, Transient Flow Simulation of a Compressed Truncated Perfect Nozzle, *AIAA Paper*, 01–3681, 2001.
[13] D. Lovely and R. Haimes, Shock Detection from Computational Fluid Dynamics Results, *AIAA Paper*, 99–3285, 1999.
[14] T. Shimizu, H. Miyajima, and M. Kodera, Numerical Study of Restricted Shock Separation in a Compressed Truncated Perfect Nozzle, *AIAA Journal*, vol.**44**, no.3, pp.576–584, 2006.
[15] H. Ikawa and F. S. Laspesa, Ignition/Duct Overpressure Induced by Space Shuttle Solid Rocket Motor Ignition, *Journal of Spacecraft*, vol.**22**, no.4, pp.481–488, 1985.
[16] D. L. Pavish and J. E. Deese, CFD Analysis of Unsteady Ignition Overpressure Effect on Delta II and Delta III Launch Vehicles, *AIAA Paper*, 2000–3922, 2000.
[17] F. Canabal and A. Frendi, Study of the Ignition Overpressure Suppression Technique by Water Addition, *Journal of Spacecraft and Rockets*, vol.**43**, no.4, pp.853–865, 2006.

Journal of the Earth Simulator, Volume 9, March 2008, 27–35

Development of an Atmospheric General Circulation Model for Integrated Earth System Modeling on the Earth Simulator

Shingo Watanabe[1]*, Hiroaki Miura[1], Miho Sekiguchi[2], Tatsuya Nagashima[3], Kengo Sudo[4,1], Seita Emori[3,1], and Michio Kawamiya[1]

[1] *Frontier Research Center for Global Change, Japan Agency for Marine-Earth Science and Technology, 3173-25, Showamachi, Kanazawa-ku, Yokohama, 236-0001, Japan*

[2] *Department of Marine Electronics and Mechanical Engineering, Faculty of Marine Technology, Tokyo University of Marine Science and Technology, 2-1-6, Etchujima, Koto-ku, Tokyo, 135-0044, Japan*

[3] *National Institute for Environmental Studies, 16-2 Onogawa, Tsukuba, Ibaraki, 305-8506, Japan*

[4] *Department of Earth and Environmental Sciences, Graduate School for Environmental Studies, Nagoya University, Furo-cho, Chikusa-ku,Nagoya, 464-8601, Japan*

(Received August 7, 2007; Revised manuscript accepted February 27, 2008)

Abstract This paper introduces an atmospheric general circulation model (AGCM) that better simulates the dynamical and physical processes and is used in the framework of our integrated earth system modeling. In particular, the dynamical and physical processes in the stratosphere are greatly improved compared to the previous version of the climate model. In this study, the top of the AGCM is extended to the mesopause height, and a hybrid σ-pressure coordinate system, which is suited for the simulation of transport phenomena near the tropopause, is introduced. An improved radiative transfer scheme dramatically decreases the cold bias near the tropical tropopause and the extratropical lower stratosphere. Incorporation of the non-orographic gravity wave drag parameterization with a source function based on the results of a high-resolution AGCM simulation allows the model to reproduce a realistic general circulation in the stratosphere and mesosphere.

Keywords: Earth system, Stratosphere, General circulation, Gravity wave

1. Introduction

An integrated earth-system model has been developed at the Frontier Research Center for Global Change (FRCGC) in collaboration with the Center for Climate System Research (CCSR) of the University of Tokyo and the National Institute for Environmental Studies (NIES). The objective for the development of an earth system model was to model the variations and changes in the global environment as a whole, that is, to develop an integrated system, which includes the physical climatic processes, the biogeochemical processes, and the eco-dynamical processes [1, 2].

In order to simulate long-term changes in climate systems and atmospheric chemistry, as well as seasonal and interannual variations, an appropriate representation of the stratosphere is required [3]. This paper focuses on the following three topics that are important to properly represent the physical and chemical interaction between the troposphere and the stratosphere. The first process considers the thermal structure near the tropopause, which is important for chemical reactions and water vapor dehydration processes that can change with global warming. The second process considers the dynamical transport processes, such as the stratosphere-troposphere exchange and the mean meridional circulation in the stratosphere. These factors change with global warming and affect the concentration of greenhouse gases in the troposphere [4, 5]. The third and final process is the meridional structure of the stratospheric jets that can affect the tropospheric climate through dynamical connections, for example, the downward propagation of solar effects associated with the internal variability of the polar night jet [6, 7], and the downward effects of the stratospheric ozone hole in late spring [8].

This paper describes the development of an atmospheric general circulation model (AGCM) in the integrated earth-system model, which is called the Model for Interdisciplinary Research on Climate (MIROC) -

* ***Corresponding author***: *Shingo Watanabe, Frontier Research Center for Global Change, Japan Agency for Marine-Earth Science and Technology, 3173-25, Showamachi, Kanazawa-ku, Yokohama, 236-0001, Japan. E-mail: wnabe@jamstec.go.jp*

Kyousei Integrated Synergetic System Model of the Earth (kissme). Results of MIROC-kissme show many improvements in comparison with the coupled general circulation model MIROC-mid, which was the basis from which the MIROC-kissme was developed [1, 9, 10]. The improvements described in this paper are achieved by 1) extending the top of the model, 2) changing the vertical coordinate system, 3) improving the radiative transfer scheme, and 4) incorporating non-orographic gravity wave drag parameterization. Section 2 discusses each of these improvements in greater detail. Results of the MIROC-kissme are compared with those of MIROC-mid in Section 3. Section 4 gives concluding remarks.

2. Development of the AGCM in MIROC-kissme

The MIROC-kissme was developed based on MIROC-mid. The AGCM in MIROC-mid is a global spectral model with a T42 horizontal resolution, that is an approximately 2.8˚ grid spacing in latitude and longitude. It has 20 layers from the surface to a height of 30 km. It includes a full-set of physical parameterizations such as radiation, cumulus convection, stratiform clouds, and boundary layer. The bottom boundary of the AGCM is coupled to a physical land component model and an oceanic general circulation model. Detailed descriptions of MIROC-mid are given in [9,10].

2.1 Vertical coordinate system

In order to fully resolve the stratosphere and mesosphere, the top of the AGCM is raised from about 30 km to the mesopause height of about 80 km. The number of vertical layers is increased from 20 to 80. Fig. 1 shows the vertical coordinate systems for MIROC-kissme (L80) and MIROC-mid (L20). The new vertical coordinate system has a fine vertical resolution of about 680 m in the upper troposphere to the middle stratosphere. The fine vertical resolution is one of the conditions necessary for the spontaneous generation of the equatorial quasi-biennial oscillation (QBO) in AGCMs [11, 12, 13]. In order to prevent extra wave reflection at the top boundary, a sponge layer is added to the top level, which causes the wave motions to be greatly dampened.

The terrain-following σ vertical coordinate system used in MIROC-mid cannot accurately represent transport processes over mountainous regions. This system creates unrealistic exchanges of trace constituents across the tropopause and, thus, causes huge moisture biases in the lower stratosphere. The σ vertical coordinate system has been replaced with a hybrid σ-pressure vertical coordinate system, in which the vertical coordinate system is switched to a pure pressure coordinate system above about 350 hPa [14]. The hybrid coordinate system gives realistic results in high-resolution AGCM simulations, in terms of ozone distribution in an ozone coupled model [13], and wave dynamics associated with orographic gravity waves [15]

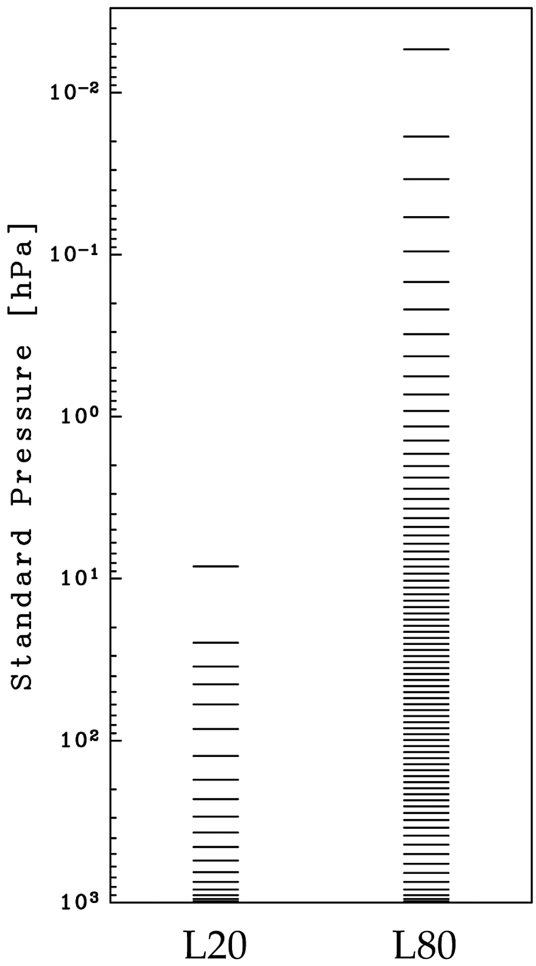

Fig. 1 Vertical coordinate system for MIROC-mid (left) and MIROC-kissme (right).

2.2 Radiative transfer scheme

The radiative transfer scheme used in MIROC-mid has problems with the accuracy of the heating rate calculations near the tropopause, which results in cold biases near the tropical tropopause and in the extratropical lower stratosphere [10]. In order to fix these biases, an updated version of the radiative transfer scheme is incorporated into MIROC-kissme. Major differences between these radiative schemes is that the new scheme 1) uses an updated database for line and continuum absorption, 2) considers an increased number of absorption bands, 3) reconsiders the number of integration points for the correlated-*k* distribution method, and 4) uses an improved optimization method to determine the best integration points. As a result, the accuracy of the heating rate calculation near the tropopause is greatly improved [16].

MIROC-kissme includes atmospheric chemistry in the troposphere and stratosphere [1]. The radiative transfer and photolysis of chemical constituents are consistently calculated. On the basis of the new radiative scheme, a new parameter table with 32 bands and 102 integration points, whose intervals are finer in the UV-VIS region than those used in the usual calculations and are optimized for the photolysis calculation of chemical constituents (ozone, molecular oxygen, and nitrous oxide), was developed. Using the new radiative scheme with the new parameter table allows MIROC-kissme to obtain a reasonable distribution of chemical constituents in the troposphere and stratosphere, as well as an accurate radiative heating rate.

2.3 Non-orographic gravity wave drag parameterization

Wind accelerations due to the momentum deposition of atmospheric gravity waves are important for the formation of the general circulation and thermal structure in the stratosphere and mesosphere [17]. The T42 horizontal resolution of the AGCM is insufficient to explicitly represent such gravity waves. Hence, the effects of such subgrid scale gravity waves should be considered using gravity wave drag parameterizations. The orographic gravity wave drag parameterization of McFarlane [18] is included in MIROC-mid and MIROC-kissme. In addition to the effects of the orographic gravity waves, effects of non-orographic gravity waves are important especially for driving the equatorial QBO and for the formation of the meridional structure of the mesospheric jets [17, 19].

The Doppler-Spread parameterization of Hines [20] is incorporated into MIROC-kissme. A source function of gravity waves is required by the Hines parameterization. It is a function of time, geographical location, propagation directions, and amount of vertical flux of horizontal momentum carried by the gravity waves. The tropospheric sources of the non-orographic gravity waves considered here are cumulus convection, fontal dynamics, and dynamical instability associated with jet streams. All of these are highly variable in time and geographical location. Furthermore, these sources emit different type of gravity waves, which depend not only on their own characteristics, but also on background winds and static stability [17]. Although recent estimations of the geographical distribution of gravity waves using satellites have been performed [21, 22], these data are still insufficient to determine the required complicated source function. Instead, the monthly climatology of the source function is derived from the results of the T213L256 AGCM simulation [18]. In the extratropics, an 8 azimuthal distribution for the horizontal wind variance and the vertical flux of horizontal momentum due to gravity waves that cannot be resolved in the horizontal resolution of T42, which is a horizontal wavelength of less than about 950 km, are considered. In the source function, the quasi-stationary gravity waves are filtered out with a running average of 48 hours, because they are considered as orographic gravity waves whose effects are separately parameterized with the McFarlane scheme. The source function is derived at about 70 hPa, where dominant gravity waves are those vertically propagating, that is, the source function should not include approximately horizontally propagating inertia gravity waves. In the tropics, an isotropic source is launched at 100 hPa. This is required, because the source function derived from the T213L256 AGCM is already affected by the equatorial QBO in that model. While Rayleigh friction is used in MIROC-mid to decrease wind speeds in the stratosphere, it is not used in MIROC-kissme, as the friction can be represented by the Hines parameterization.

2.4 Experimental set-up

The results from MIROC-kissme and MIROC-mid are compared. Both models are run as coupled climate models in which the components for the atmosphere, ocean, sea ice, land, aerosols, and river are interactively coupled. The pre-industrial CO_2 concentration of 285 ppmv, as well as the pre-industrial concentration of the other greenhouse gases and emission data for aerosols, is used. The models are run for more than 50 years using similar initial conditions. The results for 10 consecutive years are averaged for comparison. For the stratospheric ozone concentration, MIROC-mid uses a monthly climatology in the absence of the Antarctic ozone hole, while MIROC-kissme explicitly calculates the ozone and other chemical constituents under the pre-industrial conditions, that is without any anthropogenic chlorine and the absence of an Antarctic ozone hole. Differences in the ozone concentration in the models are sufficiently small so that the conclusions in the following section are not changed if the same monthly climatology data for ozone are used in MIROC-kissme.

3. Results

Fig. 2 shows the horizontal distribution of the water vapor mixing ratio at 100 hPa during December-January-February. Results from MIROC-mid exhibit an excess of water vapor around and downstream of the mountainous regions. This is primarily caused by numerical diffusion associated with the advection of humidity across the slopes of the σ coordinate surface. The results from MIROC-kissme show a realistic distribution of the water vapor. There are two distinct minima above the maritime

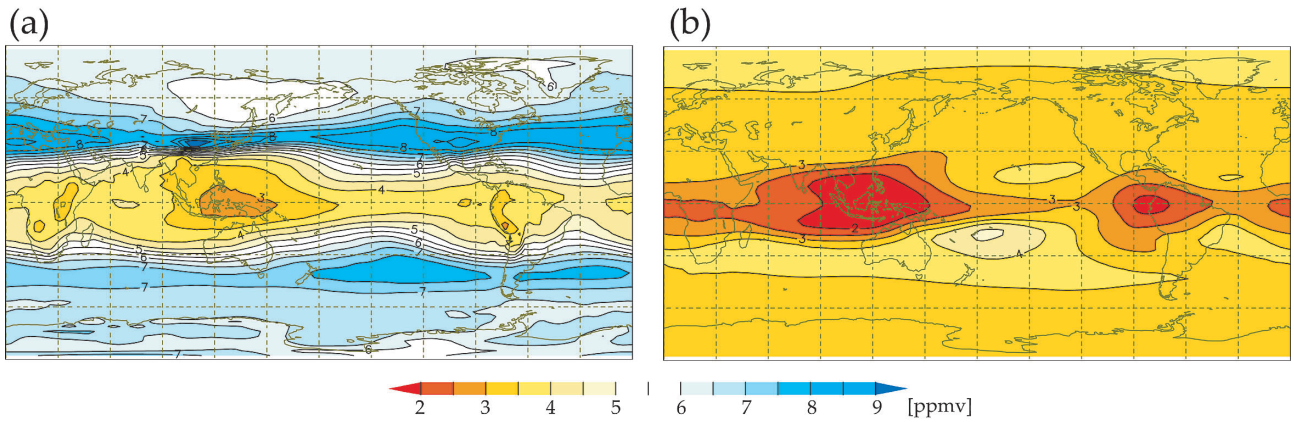

Fig. 2 December-January-February average of the water vapor mixing ratio at 100 hPa for MIROC-mid (a) and MIROC-kissme (b). The contour interval is 0.5 ppmv. Blue color shows the wet region.

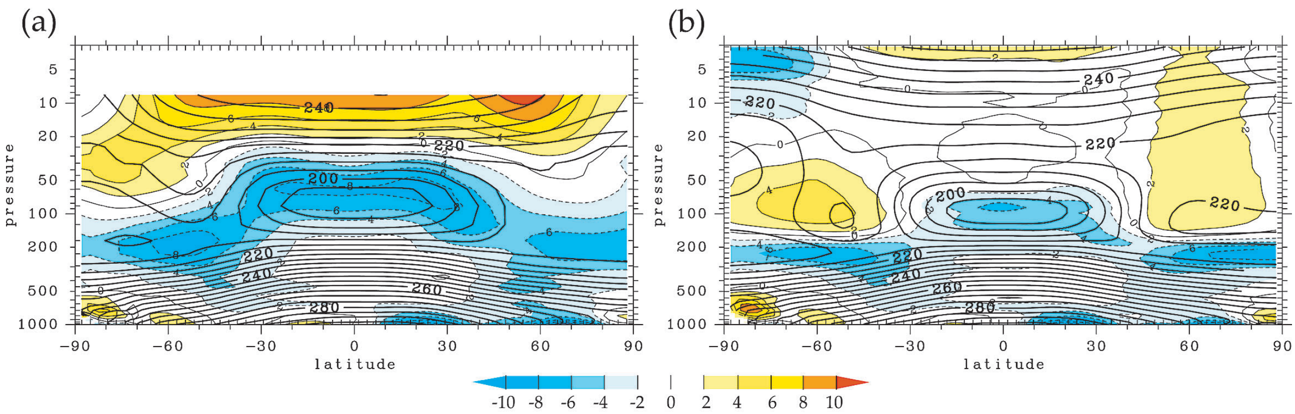

Fig. 3 Annual average of the zonal mean temperature for MIROC-mid (a) and MIROC-kissme (b). The contour interval is 10 K. Shading shows the temperature bias compared to the 1994-2001 average of the Met Office assimilation data. The contour interval is 2 K. Blue shows the cold bias.

continent and the tropics of South America, while there is a maximum over the middle Pacific in the Southern Hemisphere. This distribution is qualitatively similar to that for the ERA-40 re-analysis data [23].

Fig. 3 shows the meridional distribution of the annual average zonal mean temperature and its bias compared to the Met Office assimilation data [24], which are averaged for 1994–2001. The results from MIROC-mid have large cold biases near the tropical tropopause and in the extratropical lower stratosphere. These cold biases are dramatically decreased by the new radiative scheme. The remaining cold bias near the tropopause is probably associated with the treatment of ice clouds in the model. Alternatively, it suggests that further improvement is required in the radiative scheme.

The decrease of the cold bias in the extratropical lower stratosphere is partly due to the improvement of water vapor distribution resulting from the use of the σ-pressure hybrid coordinate system. A warm bias in the Southern Hemisphere lower stratosphere is associated with the pre-industrial condition, while the effects of the ozone hole lower the polar temperature for the present day climatology. Temperature biases near the surface are not considered. They are partly caused by issues related to properly determining the cloud distribution. This situation needs to be addressed in a separate study.

Fig. 4 shows the meridional structure of the zonal-mean zonal wind in January, over which the Met Office zonal wind is overlaid. The strength of the upper part of the subtropical jet is overestimated in results from MIROC-mid. The results from MIROC-kissme show a better correlation with the real data. This can be attributed to the decrease in the cold bias near the tropopause. The improved meridional structure of the subtropical jet may alter the vertical flux of wave activity propagating into the stratosphere through changes in the refractive index. Atmospheric waves in these models can be analyzed in future work.

Fig. 5 shows the July climatology of the gravity wave source function, which is used in the Hines gravity wave

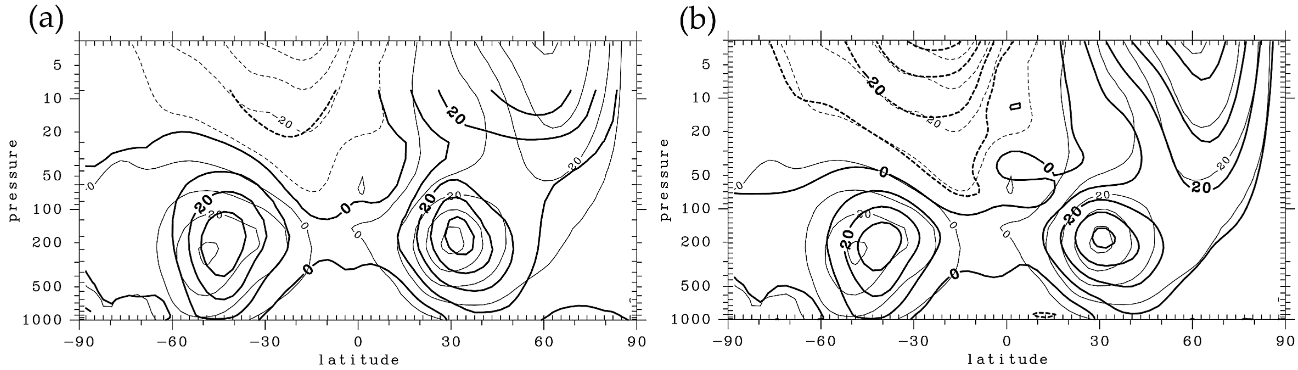

Fig. 4 December-January-February average of the zonal mean zonal wind for the MIROC-mid (a) and MIROC-kissme (b). The contour interval is 10 m·s^{-1}. Thin contours show the 1994-2001 average of the Met Office assimilation data.

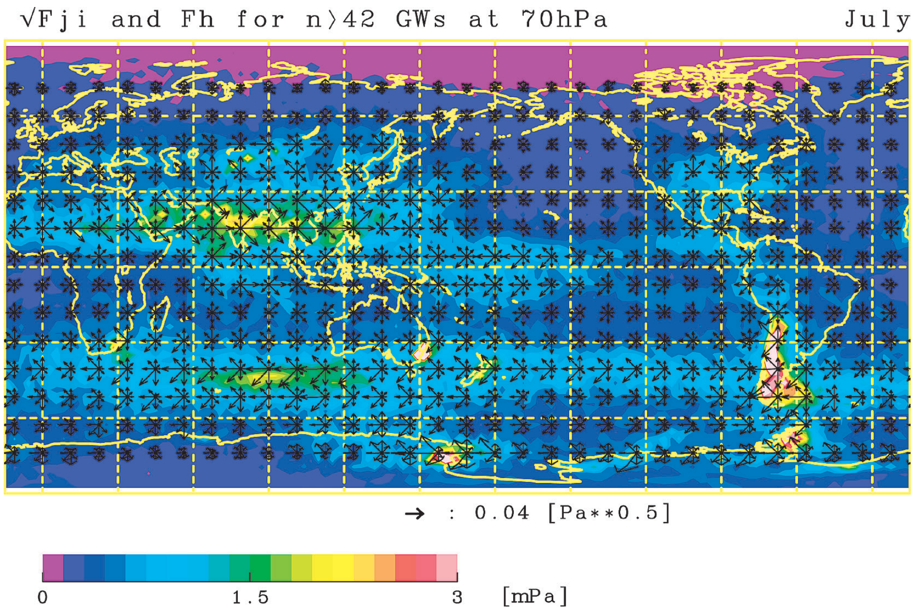

Fig. 5 The source function used for the Hines parameterization. Arrows show the eight azimuthal components for the monthly averaged vertical flux of the horizontal momentum associated with small scale (< 950 km) gravity waves, which are derived using the result of the T213L256 AGCM. The length of the arrows shows the square root of the momentum flux for better visualization. Color shows the magnitude of the momentum flux, which is represented by the square root average of the eight azimuthal components.

drag parameterization (see Section 2.3 for a description). Non-orographic gravity waves with large momentum fluxes are mainly emitted from the cumulus convection associated with tropical cyclones, cloud clusters, and extratropical low-pressure systems. Directions of wave propagation are mostly towards the upstream of the background large-scale winds. Eastward propagating gravity waves are dominant in an easterly wind region associated with the Indian summer monsoon circulation. Westward propagating gravity waves are dominant at the Southern Hemisphere mid-latitudes, whose dissipation causes decelerations of the wintertime westerly jet in the stratosphere and mesosphere. The source function includes some orographic gravity wave signatures over Antarctica and the South Andes. They are difficult to separate from the non-orographic gravity waves, because they have a wave structures that varies with time [15].

Fig. 6 shows the meridional distribution of the zonal-mean zonal wind for MIROC-kissme, as well as the CIRA86 wind [25]. In January, the model accurately simulates the meridional structure of the wintertime westerly jet in the stratosphere. An axis of the westerly jet exists between 60°N and 70°N below about 1 hPa, while it exists at lower latitudes in the mesosphere. The strength

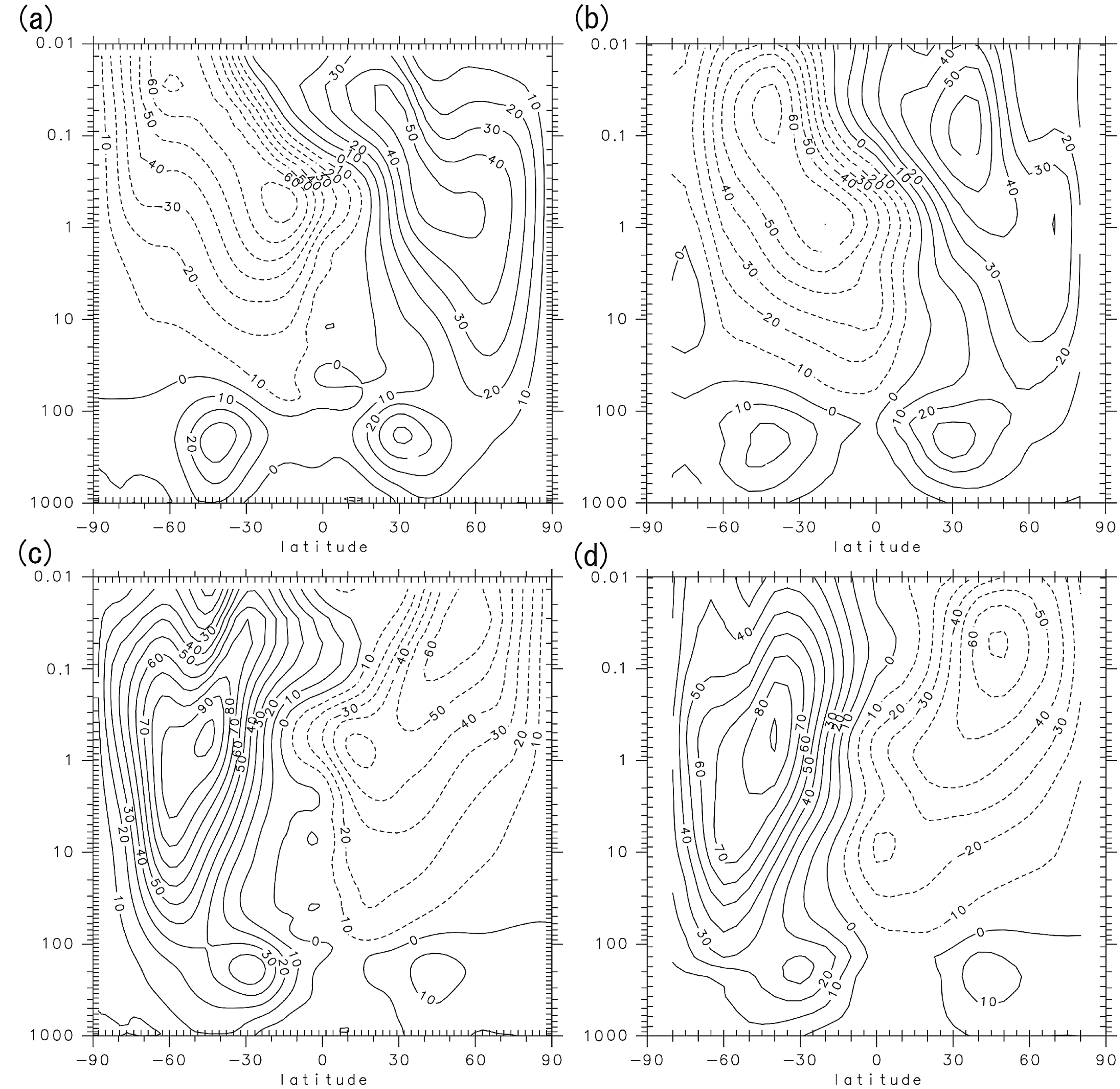

Fig. 6 The zonal mean zonal wind in January for MIROC-kissme (a) and CIRA86 (b), and in July for MIROC-kissme (c) and CIRA86 (d). The contour interval is 10 m·s^{-1}. Dashed contours show the easterly winds.

of the westerly wind is comparable to the CIRA wind in the lower stratosphere, while it is slightly overestimated in the upper stratosphere and mesosphere. In July, the modeled Southern Hemisphere westerly jet has similar characteristics to those observed. The center of the westerly jet tilts equatorward with increasing altitude above about 10 hPa. The mesospheric westerly jet has a double peak structure. The strength of the westerly wind is overestimated above the middle stratosphere by about 10–20 m·s^{-1}, which is mainly due to a lack of effects for the horizontal propagation of gravity waves in the Hines scheme [19]. The easterly jet in the summer hemisphere middle atmosphere is also reasonably simulated. The center of its maximum shifts poleward with increasing altitude from the upper stratosphere to the mesosphere. Wind speeds of the easterly jet are also realistic. These results show that the model with Hines parameterization and the given source function reproduces reality accurately.

Fig. 7 shows the time evolution of the monthly averaged equatorial zonal mean zonal wind for MIROC-kissme. The stratopause semi-annual oscillation is seen near 1 hPa [26]. It starts in the mesosphere and propagates downward to the stratopause height. The zonal wind oscillation in the upper mesosphere has an opposite phase to that near the stratopause. These characteristics are qualitatively reasonable, although observations in the mesosphere are insufficient for quantitative comparisons. In the lower stratosphere, a QBO-like zonal wind oscillation is seen. The typical maximum wind speeds are about 13 m·s^{-1} for the westerly phase and about 27 m·s^{-1} for

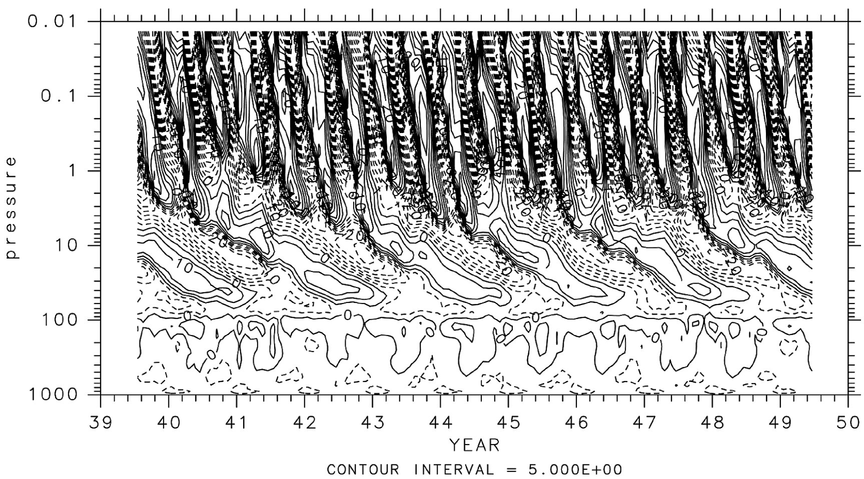

Fig. 7 Time evolution of the monthly averaged zonal mean zonal wind at the equator. The contour interval is 5 $m \cdot s^{-1}$. Dashed contours show the easterly winds.

the easterly phase. The model underestimates the amplitude of the QBO by about 5 $m \cdot s^{-1}$. Periods of the modeled QBO-like oscillation are about 18 months, while those observed average approximately 28 months [27]. The amplitude and period of the modeled QBO-like oscillation strongly depends on the strength of the gravity wave source used in the Hines parameterization. Careful tuning of the source function in the tropics may allow the model to reproduce a more realistic QBO-like oscillation. This tuning is beyond the scope of this study. The tuning should not be a difficult task, because other GCMs with the Hines gravity wave drag parameterization have reproduced quite realistic QBO-like oscillation [28, 29]. However, the next step is to consider the temporal evolution of the gravity wave source function associated with global warming [30, 31]. Further observations and model experiments should be required to reduce uncertainly in future changes in gravity waves and the QBO.

4. Conclusions

Compared with the MIROC-mid, the dynamical and physical processes in the stratosphere determined by MIROC-kissme are much better. The hybrid σ-pressure vertical coordinate system reduces the moisture bias. The cold biases near the tropical tropopause and in the extratropical lower stratosphere are decreased by the updated radiative scheme. The overestimation of the westerly wind in the upper part of the tropospheric subtropical jet is also decreased. This can be associated with the improvement in the thermal structure near the tropopause. The general circulation in the middle atmosphere is successfully simulated using the Hines gravity wave drag parameterization with the source function derived from the high-resolution AGCM. It is expected that a more realistic future projection for global warming can be obtained using MIROC-kissme, which has an improved stratosphere. The realistic thermal structure around the tropopause allows an accurate evaluation of climate forcing due to greenhouse gases. The stratosphere-troposphere exchange of greenhouse gases, such as ozone, water vapor, and methane, can be calculated more accurately. Future studies will consider the effects of the QBO and solar variability on the dynamical and thermal fields, as well as on atmospheric chemistry. Distribution of the modeled chemical constituents and statistics for the transport processes in the MIROC-kissme will be studied.

Acknowledgments

The authors thank anonymous refrees for valuable comments on the original manuscript. This study is a contribution to the Innovative Program of Climate Change Projection for the 21st Century, MEXT Japan. The simulations in this study are performed on the Earth Simulator, and GFD-DENNOU Library and GTOOL were used for drawing the figures.

(This article is reviewed by Dr. Takeshi Enomoto.)

References

[1] M. Kawamiya, C. Yoshikawa, T. Kato, H. Sato, K. Sudo, S. Watanabe, and T. Matsuno, Development of an Integrated Earth System Model on the Earth Simulator, *Journal of the Earth Simulator*, vol.**4**, pp.18–30, 2005.

[2] IGBP, Science plan and implementation strategy, *IBGP Report*, No.55, IGBP Secretariat, Stockholm, 76pp, 2006.

[3] V. Erying, N. Buchart, D. W. Waugh, H. Akiyoshi, J. Austin, S. Bekki, G. E. Bodeker, B. A. Boville, C. Brühl, M. P. Chipperfield, E. Cordero, M. Dameris, M. Deushi,

V. E. Fioletov, S. M. Frith, R. R. Garcia, A. Getteleman, M. A. Giorgetta, V. Grewe, L. Jourdain, D. E. Kinnison, E. Mancini, E. Manzini, M. Marchand, D. R. Marsh, T. Nagashima, P. A. Newman, J. E. Nielsen, S. Pawson, G. Pitari, D. A. Plummer, E. Rozanov, M. Schracer, T. G. Shepherd, K. Shibata, R. S. Stolarski, H. Struthers, W. Tian, and M. Yoshiki, Assessment of temperature, trace species, and ozone in chemistry-climate model simulations of the recent past, *J. Geophys Res.*, vol.**111**, D23308, doi:10.1029/2006JD007327, 2006.

[4] N. Buchart and A. A. Scaife, Removal of chlorofluorocarbons by increased exchange between the stratosphere and troposphere in a changing climate, *Nature*, vol.**410**, pp.799–802, 2001.

[5] K. Sudo, M. Takahashi, and H. Akimoto, Future changes in stratosphere-troposphere exchange and their impact on future tropospheric simulations, *Geophys. Res. Lett.*, vol.**30**, 2256, doi:10.1029/2004GL020794, 2003.

[6] K. Kodera, On the origin and nature of interannual variability of the winter stratospheric circulation in the northern hemisphere, *J. Geophys. Res.*, vol.**100**, pp.14077–14087, 1995.

[7] K. Matthes, Y. Kuroda, K. Kodera, and U. Langematz, Transfer of the solar signal from the stratosphere to the troposphere: Northern winter, *J. Geophys. Res.*, vol.**111**, D06108, doi:10.1029/2005JD006283, 2006.

[8] S. Watanabe, T. Hirooka, and S. Miyahara, Interannual variations of the general circulation and polar stratospheric ozone losses in a general circulation model, *J. Meteorol. Soc. Japan*, vol.**80**, no.4b, pp.877–895, 2002.

[9] K-1 model developers, K-1 coupled model (MIROC) description, *K-1 Technical Report*, vol.**1**, H. Hasumi and S. Emori (eds.), Center for Climate System Research, University of Tokyo, 34pp., 2004.

[10] T. Nozawa, T. Nagashima, T. Ogura, T. Yokohata, N. Okada, and H. Shiogama, Climate change simulations with a coupled ocean-atmosphere GCM called the Model for Interdisciplinary Resarch on Climate: MIROC, *CGER'S SUPERCOMPUTER MONOGRAPH REPORT*, vol.**12**, Center for Global Environmental Research, National Institute for Environmental Studies, Tsukuba, Japan, 2007.

[11] M. Takahashi, Simulation of the stratospheric quasi-biennial oscillation using a general circulation model, *Geophys. Res. Lett.*, vol.**23**, pp.661–664, 1996.

[12] M. Takahashi, Simulation of the stratospheric quasi-biennial oscillation in a general circulation model, *Geophys. Res. Lett.*, vol.**26**, pp.1307–1310, 1999.

[13] S. Watanabe and M. Takahashi, Kelvin waves and ozone Kelvin waves in the quasi-biennial oscillation and semiannual oscillation: A simulation by a high-resolution chemistry-coupled general circulation model, *J. Geophys. Res.*, vol.**110**, D18303, doi:10.1029/2004JD005424, 2005.

[14] H. Miura, Vertical differencing of the primitive equations in a σ-p hybrid coordinate (for spectral AGCM), *CCSR Internal Report*, pp.1–19, University of Tokyo, 2002.

[15] S. Watanabe, K. Sato, and M. Takahashi, A general circulation model study of orographic gravity waves over Antarctica excited by katabatic winds, *J. Geophys. Res.*, vol.**111**, D18104, doi:10.1029/2005JD006851, 2006.

[16] M. Sekiguchi and T. Nakajima, The study of the absorption process and its computational optimization in an atmospheric general circulation model, J. Quant. Spectrosc. Radiat. Transfer (to be submitted).

[17] D. C. Fritts and M. J. Alexander, Gravity wave dynamics and effects in the middle atmosphere, *Rev. Geophys.*, vol.**41**, 1003, doi:10.1029/2001RG000106, 2003.

[18] N. A. McFarlane, The effect of orographically excited gravity wave drag on the general circulation of the lower stratosphere and troposphere, *J. Atmos. Sci.*, vol.**44**, pp.1775–1800, 1987.

[19] S. Watanabe, Y. Kawatani, Y. Tomikawa, K. Miyazaki, M. Takahashi, and K. Sato, General aspects of a T213L256 middle atmosphere general circulation model, *J. Geophys. Res.* (submitted).

[20] C. O. Hines, Doppler-spread parameterization of gravity-wave momentum deposition in the middle atmosphere. Part 2: Broad and quasi monochromatic spectra, and implementation, *J. Atmos. Solar Terr. Phys.*, vol.**59**, pp.387–400, 1997.

[21] D. L. Wu and J. W. Waters, Satellite observations of atmospheric variances: A possible indication of gravity waves, *Geophys. Res. Lett.*, vol.**23**, pp.3631–3634, 1996.

[22] T. Tsuda, M. Nishida, C. Rocken, and R. H. Ware, A global morphology of gravity wave activity in the stratosphere revealed by the GPS occultation data (GPS/MET), *J. Geophys. Res.*, vol.**105**, pp.7257–7273, 2000.

[23] S. M. Uppala, P. W. Kållberg, A. J. Simmons, U. Andrae, V. da Costa Bechtold, M. Fiorino, J. K. Gibson, J. Haseler, A. Hernandez, G. A. Kelly, X. Li, K. Onogi, S. Saarinen, N. Sokka, R. P. Allan, E. Andersson, K. Arpe, M. A. Balmaseda, A. C. M. Beljaars, L. van de Berg, J. Bidlot, N. Bormann, S. Caires, F. Chevallier, A. Dethof, M. Dragosavac, M. Fisher, M. Fuentes, S. Hagemann, E. Holm, B. J. Hoskins, L. Isaksen, P. A. E. M. Janssen, R. Jenne, A. P. McNally, J.-F. Mahfouf, J.-J. Morcrette, N. A. Rayner, R. W. Saunders, P. Simon, A. Sterl, K. E. Trenberth, A. Untch, D. Vasiljevic, P. Viterbo, and J. Woollen, The ERA-40 re-analysis, *Quart. J. R. Meteorol. Soc.*, vol.**131**, pp.2961–3012, doi:10.1256/qj.04.176, 2005.

[24] R. Swinbank and A. O'Neill, A stratosphere-troposphere data assimilation system, *Mon. Wea. Rev.*, vol.**122**, pp.686–702, 1994.

[25] D. Rees, J. J. Barnett, and K. Labitzke (ed.), CIRA 1986,

Part II Middle Atmosphere Models, *Advances in Space Research (COSPAR)*, vol.**10**, no.12, 1990.

[26] I. Hirota, Equatorial waves in the upper stratosphere and mesosphere in relation to the semiannual oscillation of the zonal wind, *J. Atmos. Sci*., vol.**35**, pp.714–722, 1978.

[27] M. P. Baldwin, L. J. Gray, T. J. Dunkerton, K. Hamilton, P. H. Haynes, W. J. Randel, J. R. Holton, M. J. Alexander, I. Hirota, T. Horinouchi, D. B. A. Jones, J. S. Kinnersley, C. Marquardt, K. Sato, and M. Takahashi, The Quasi-Biennial Oscillation, *Rev. of Geophys.*, vol.**39**, pp.179–229, 2001.

[28] M. A. Giorgetta, E. Manzini, and E. Roeckner, Forcing of the quasi-biennial oscillation from a broad spectrum of atmospheric waves, *Geophys. Res. Lett.*, vol.**29**, no.8, pp.86–1 – 86–4, 2002.

[29] A. A. Scaife, N. Butchart, C. Warner, D. Stainforth, W. Norton, and J. Austin, Realistic quasi-biennial oscillations in a simulation of the global climate, *Geophys. Res. Lett.*, vol.**27**, pp.3481–3484, 2000.

[30] S. Watanabe, T. Nagashima, and S. Emori, Impact of global warming on gravity wave momentum flux in the lower stratosphere, *SOLA*, vol.**1**, pp.189–192, 2005.

[31] M. A. Giorgetta and M. C. Doege, Sensitivity of the quasi-biennial oscillation to CO_2 doubling, *Geophys. Res. Lett*., vol.**32**, L08701, doi:10.1029/2004GL021971, 2005.

Journal of the Earth Simulator, Volume 9, March 2008, 37–49

Global Warming Simulation using the High-Resolution Climate Model

A Summary of the K-1 Project

Akimasa Sumi

Center for Climate System Research, The University of Tokyo,
5-1-5 Kashiwanoha, Kashiwa-City, Chiba, 277-8568 Japan
E-mail: sumi@ir3s.u-tokyo.ac.jp

(Received February 21, 2007; Revised manuscript accepted March 3, 2008)

Abstract A high resolution climate model has been developed in order to improve the simulation of Global Warming. Based on preliminary experiments, characterization of the model such as resolution and physical process subroutines has been determined as follows. An atmospheric component employs the T106 global spectral model with 56 levels and an ocean component involves a 1/4˚ × 1/6˚ grid point model with 46 levels. A land surface model (MATSUSIRO = Minimal Advanced Treatments of Surface Interaction and RunOff) and a river run-off model are also incorporated. Corresponding to the increase in horizontal and vertical resolutions, all the physical processes have been retuned. Various options of parameterization schemes have been examined and a final specification has been decided upon. The atmospheric component and the ocean component are allocated to different nodes and comunicated through a coupler. 10 nodes in the Earth Simulator (ES) are allocated to the atmospheric component and 76 nodes are allocated to the oceanic component.

The climate model has been run, covering 100 years, as a control run and it is noted that there is no climate drift result even though the flux correction technique is not applied. The globally averaged surface temperature is about 14˚C and the amplitude of the annual variation is about 3.5˚C. Compared with climatology, the global mean is 4˚C cooler and the annual cycle is of the same order. A low surface temperature bias is noted in the mid-latitude of the northern hemisphere, although warm surface temperature is noted in the southern hemisphere. Meridional circulation in the Atlantic Ocean is maintained at about 20 Sv, and ocean currents and convection in GIN (Greenland-Iceland-Norway) Sea region are well simulated. In the tropics, a dominant double ITCZ feature is found, consistent with an ENSO-like SST pattern. The Asian monsoon variability is well simulated.

Many runs were then conducted for the IPCC AR4 (the 4-th Assessment Report). The globally averaged surface temperature increase by 2100 in the SRES A1B scenario was about 3.5˚C. Much information has been obtained concerning regional climate change, such as the changes in precipitation in the Baiu and the Kuroshio Current. In summary, the high-resolution climate model is able to represent many features of the mean states and variability of the present climate, and offer more detailed information about the future climate. It is concluded that the high-resolution climate model is an indispensable tool for conducting Global Warming simulations.

Keywords: high resolution climate model, Earth Simulator, Global Warming

1. Introduction—Background to the development of the high-resolution climate model

Climate change associated with the Global Warming is one of the most important problems with which the 21st century society is confronted. Immediate action is necessary by all governments, and for this purpose, demand for a more reliable assessment of Climate Change at the regional-scale is increasing. For example, we are frequently asked whether, or not, the numbers of severe storms and typhoons have increased recently. However, the present climate model is not sufficient to answer these questions accurately, mainly because our knowledge of the climate system is insufficient and model capability is imperfect. On the other hand, it is true that we do not make a maximum use of our present knowledge. For example, in case of short-range weather forecasting, we are able to make better and reliable forecasts. If we can apply a weather forecasting model to the Global Warming issue, better results are expected to be obtained. The reason why this knowledge of the daily weather forecast cannot be applied to climate modeling is because our computational capability is limited.

In general, more processes and higher resolution are required in order to achieve a reliable Global Warming simulation. An example of invoking more processes is the coupling of a carbon cycle with a climate model. An example of higher resolution is the increased spatial and temporal resolutions within the climate model. However, increasing resolution does not directly guarantee a better quality of simulation. Better representation of physical processes, consistent with the high resolution grid system, is critical for improved simulation. At the same time, we have to pay attention to any uncertainty associated with the simulation. In order to increase reliability, an ensemble technique has become widely used. Through these improvements of models and underatanding of processes in the natue, more reliable assessment of future change, such as extreme events and floods, should be obtained.

It goes without saying that a huge computer capability is necessary to achieve the goals described above. With respect to computer hardware, the Earth Simulator project which was conducted from 1998 to 2002, has opened a door to the new era of high-end computing! Subsequent to the Earth Simulator project, USA and Japan as well as South Africa and Singapore are developing a new super computer.

Once a high-end computing capability is provided, it becomes an issue of how to make a maximum use of it. We have discussed as to whether higher resolution or complexity or both are needed. As a result, we have chosen the high resolution option, rather than including processes such as a carbon cycle. The reasons are as follows; (1) In order to obtain a support from people for the adaptation and mitigation policies, we have to present detailed information regarding the future climate situation when greenhouse gases are doubled. (2) For that purpose, we have to present information as to what kind of weather may occur in the future. We require information of climate change at finer scales in both temporal and spatial scales in order to provide society with more reliable climate scenarios. Thus, it is considered that a climate model, which can be used in weather forecasting, is necessary for the Global Warming simulations. (3) With the carbon-cycle and other processes, there are many unknown processes and fundamental research is still necessary. In short, we have decided to develop a high resolution, atmosphere-ocean coupled model. As computer resources for the Earth Simulator are limited, a project to develop a high resolution, atmosphere-ocean coupled model has been started, jointly, by CCSR (Center for Climate System Research, The University of Tokyo), NIES (National Institute of Environmental Studies) and FRCGC (Frontier Research Center for Global Change).

2. Model design

Although the Earth Simulator has a huge computational power, there is a limit to the capability. Thus, we have to design the characterization of the high resolution climate model. For this, we have to define the requirements and objectives of the model. Then, in order to satisfy those requirements and achieve the objectives, the specifications of the model must be determined. In the past, computing capability was a limiting factor. We have frequently determined the specifications of the model in order to maximize performance with the available computer capability, without consideration of the objectives and requirements.

First, we have to consider the computer resources available, because many experiments need to be done for the Global Warming Simulation. For IPCC runs, the following numerical experiments were proposed;

(1) CO_2 transient experiment, increasing CO_2 by 1% per year

(2) Simulation of the 20th century climate

(3) Simulation, based on the IPCC SRES scenario.

Furthermore, when we consider the time schedule for submitting results to IPCC, a 100 year time integration of the coupled model should be completed in one month, using the Earth simulator. This is the first requirement.

How about the objective? Our objectives are to provide information about the regional climate changes over the East Asia. Thus, the second requirement is to represent the prominent phenomena in the East Asia such as the Baiu phenomena and the Kuroshio.

Next question is as to what depth of resolution is necessary. It is obvious that resolution should be consistent with the subroutines for physical processes. We have determined this by reference to previous AGCM experiment results. For example, Kawatani and Takahashi (2003) ran the T106L60 AGCM to simulate the Baiu front. They succeeded in simulating the mean profile of the Baiu front as well as disturbances in it. Kimoto (2002) examined the frequency distribution of daily precipitation in T42 and T106 AGCM, and observations over a 5.0 × 5.0 box (Fig. 1, top), 2.5 × 2.5 boxes (Fig. 1, middle) and 1.0 × 1.0 box simulations (Fig. 1, bottom) around Japan. It was clearly shown that the light rain is more frequent in the T42 simulation than actually observed. On the other hand, frequency of heavy rainfall became larger in T106. It is concluded that the T106 simulation well represents the observed distribution.

Regarding the ocean component, characterization was determined by reference to the past experiments over the North Western Pacific region. For example, the variability of sea surface height over the North-eastern Pacific region from simulations with different resolutions has

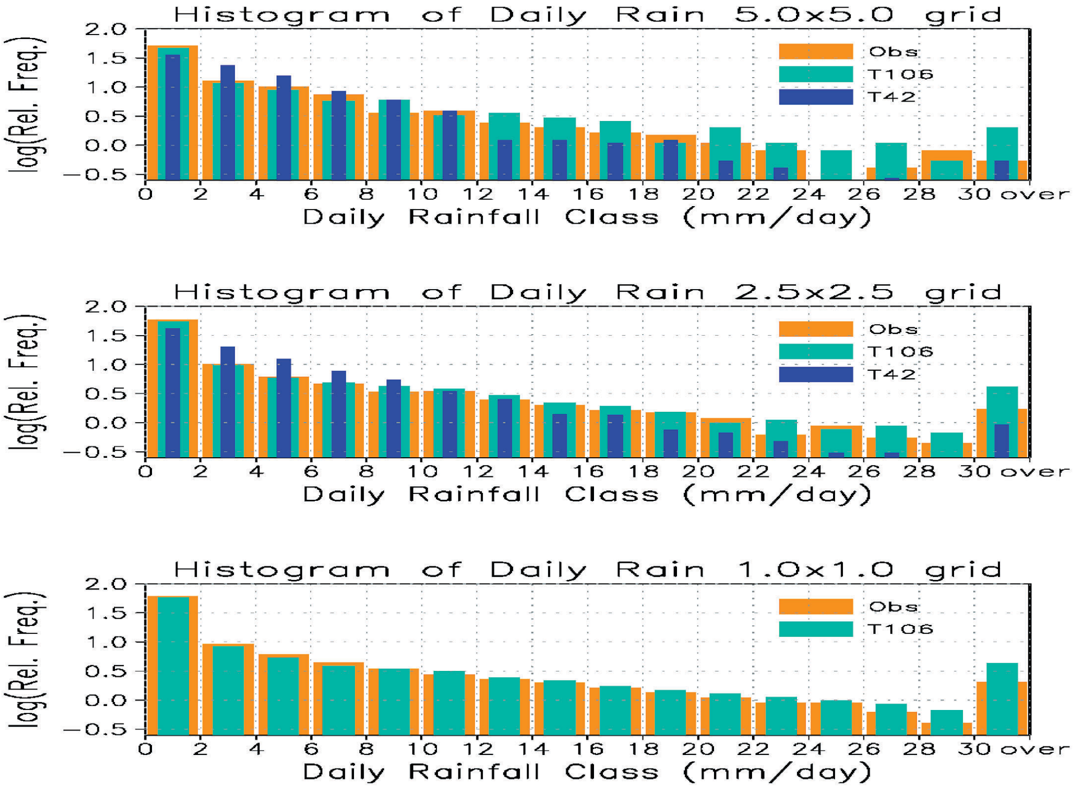

Fig. 1 Histogram of daily rainfall over the Japan, simulated by the T42 (blue) and T106 (green) AGCM. Observation (brown) is also shown. Daily rainfall is averaged over 5 degrees in longitude by 5 degrees in latitude (top), 2.5 degrees by 2.5 degrees (middle), and 1 degree by 1 degree (bottom) regions.

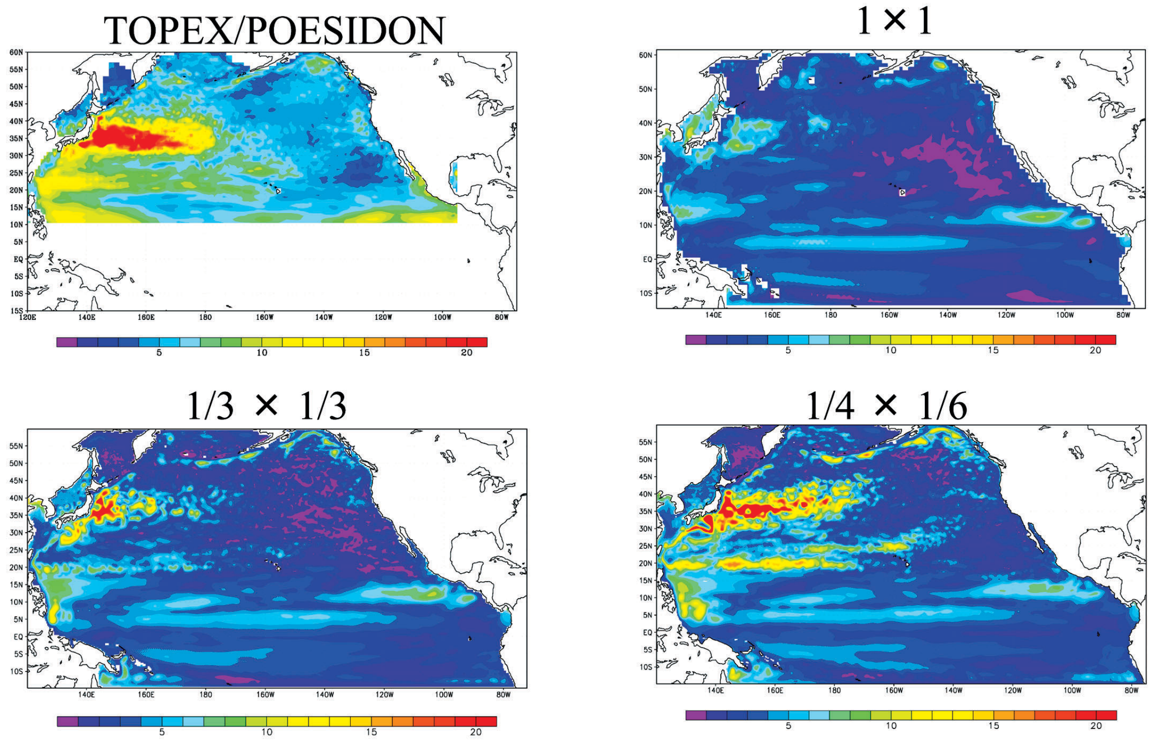

Fig. 2 Variability of surface height over the north Pacific region. (Top left) is an observation by satellite altimeter (TOPEX/POESIDON). Results over 1 degree by 1 degree (top right), 1/3 degree by 1/3 degree (bottom left) and 1/4 degree by 1/6 degree (bottom right) OGCM are displayed. These model results were obtained by observed wind forcing.

Table 1 Characterization of the high resolution atmosphere-ocean coupled model. For more details, see K-1 Model developers (2004).

(1) Atmospheric component;
① T106 spectral dynamical core with 56 level sigma levels,
② Grid advection for tracer transport,
③ K-distribution DOM/Adding radiation with maximum-random cloud overlapping,
④ Direct and indirect aerosol effect,
⑤ Prognostic Arakawa-Schubert cumulus convection scheme,
⑥ Meller-Yamada level 2 + non-local PBL,
⑦ Topography induced gravity drag.
(2) Oceanic component;
① Grid ocean model with a free surface(hybrid sigma-z model),
② Rotated lat.-lon. Grid (Poles are in Greenland and Antarctic),
③ 48 vertical levels with 8 sigma levels near the surface,
④ UTOPIA/QUICKEST advection scheme,
⑤ Smagorinsky horizontal viscosity,
⑥ Isopycnal diffusion,
⑦ Surface Boundary layer,
⑧ Bottom boundary layer,
⑨ Convective adjustment.

been examined. In Fig. 2, the simulation results from a 1 degree × 1 degree model, 1/3 degree × 1/3 degree model and 1/4 degree × 1/6 degree model are shown, with the observed height variability using the Topex-Poseidon. Compared with the satellite observations, it is considered that the 1/4 degree × 1/6 degree model result well represents nature (Nakano and Hasumi, 2003). Besides this comparison, various aspects have been examined, such as the separation of the Kuroshio from Japan Island. In this case, we concluded that 1/4 degree × 1/6 degree resolution is sufficient.

Based on the reasoning described above, we have determined the characterization of the high resolution climate model (see, Table 1). This model is named the MIROC (Model for Interdisciplinary Research on Climate)-high in the IPCC AR4 archives. At the same time, since the project is named as the first component of *Kyousei Project (in Japanese)*, we often call the model the K-1 model. Coupling of atmospheric component and oceanic component is achieved through MPMD (Multiple Programming and Multiple Data). Another feature of the model is the inclusion of an interactive aerosol model, where 5 species of aerosols (dust, sea salt, sulfate, black carbon and organic carbon). A direct effect and the first and the second indirect effects of the aerosols are included, as a unique feature of this model (Takemura et al, 2005). Other component models include the land surface model (MATSUSIRO) and the river run-off model. For more detailed information, refer to the document(K-1 Model developers, 2004) Besides the high-resolution climate model, the medium-resolution climate model, whose atmospheric component is T42L20 AGCM and ocean component is 0.5–1.4 × 1.4 degree OGCM with 44 levels, is also employed. Codes for the physical processes are common to both models, although it is impossible to make the effects of the physical processes equal in the two models. We have investigated the mechanism of the climate system by applying both models. For example, an ensemble run has been conducted by using the medium resolution model, because of computational efficiency. To obtain the regional impacts, however, the high resolution climate model is used.

3. Performance of the K-1 climate model

Many simulations including runs for IPCC AR4 have been conducted and analyzed, using this model, (Emori et al, 2005a; Suzuki et al, 2005a; 2005b, Yokohata et al, 2005a; 2005b). In this section, the basic performance of the K-1 model is described.

First, climate drift is examined. Here, it should be noted that a flux correction method is not applied in our simulation. The time-sequence of monthly mean globally averaged 2-m temperatures in the control run over 100 years are shown in Fig. 3 (top) and the sea-ice contents in the northern hemisphere(red) and the southern hemisphere (black) are shown in Fig. 3 (bottom). The globally averaged 2-m temperature is about 14˚C and the amplitude of the annual cycle is about 3.5˚C. Compared with the climatology (about 18˚C), the global mean is 4˚C cooler than the observation, but the amplitude of the annual cycle is of the same order. The content of sea-ice is stable for all 100 years in the control run, suggesting that heat balance is maintained in the climate model. In summary, it is concluded that the model shows no climate drift.

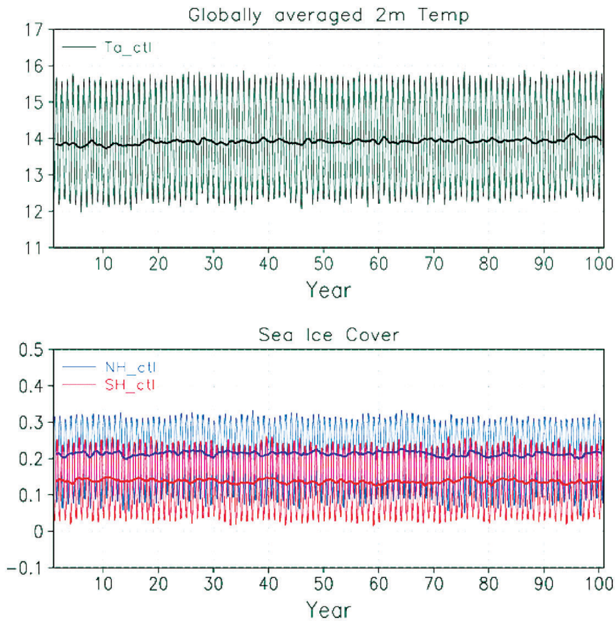

Fig. 3 Time-sequence of the globally averaged 2 m temperature (top) and sea-ice cover (bottom). Blue color represents the Arctic sea-ice and the red color represents the Antarctica sea-ice.

Performance of the climate can be briefly judged by using the annual mean of precipitation field and the Sea Surface Temperature (SST) field. Thus, the precipitation (top) and SST (middle) fields, averaged over 100 years, in the control run (left) and from observation (right), are shown in Fig. 4. First, the annual mean observed rainfall is examined. In general, detailed feature of the precipitation pattern is well simulated, for example, the Baiu front is well simulated. On the other hand, the SPCZ is poorly simulated, and the double ITCZ features are emphasized. Compared with the observed SST (middle, left in Fig. 4), it is noted that the general features of the SST are well represented, although there are many points to be improved. The warm water pool in the western tropical Pacific is narrower than the observation and the expansion of the warm water pool into the subtropical western Pacific in the northern hemisphere is not well

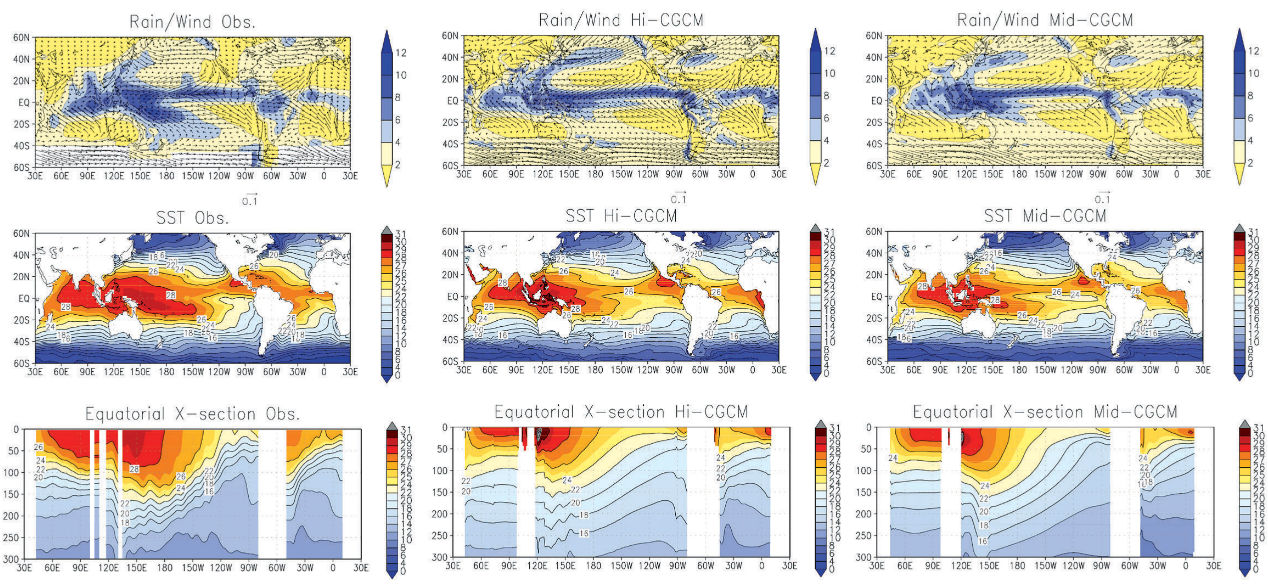

Fig. 4 Annual mean of precipitation and wind fields at 850 hPa (top), Sea Surface Temperature (middle) and cross section of sea temperature along the equator (bottom). Observations (left) and the results from the high-resolution model and the medium resolution (right) are shown. Counters for SST are 2 degrees.

simulated. The warm SST bias off the Peru coast is also noted. In other words, we can say that the model is biased toward an ENSO-like situation. Finally, the zonal-depth cross-sections of the sea temperature structure along the equator are shown at the bottom of Fig. 4. Compared with the observations, the structure of the main thermocline in the simulation tends to be diffusive. These are common features to most of climate models, which suggest that basic knowledge of the key processes is insufficient. This may be improved in the future. In the mid-latitude, a cold bias is noted, both in the Pacific ocean and the Atlantic ocean in the northern hemisphere, but a slightly warm bias is noted in the southern hemisphere. However, the SST distribution is maintained during the 100 year time integration. Although there are many unsatisfactory aspects, it can be said that the major features of the present climate system are well represented in this climate model.

Next, we will examine the possibility of representing severe events of precipitation. Main concern is whether extreme and severe events will be well simulated or not. As an example, we have examined the frequency distribution of daily precipitation over a 2.5 degree by 2.5 degree region around the Japan area (Fig. 5). In the same figure, the medium resolution (T42) climate model result is displayed. This figure is similar to Fig. 1, but the results from the coupled model are presented in Fig. 5. It is found that there exits a higher frequency of light rain in T42 than in T106. On the other hand, a higher frequency in heavy rainfall exists in T106. Compared with the observed frequency distribution, it can be said that the result simulated by the high resolution climate model is able to well represent the observed frequency distribution. Compared with Fig. 1, the frequency of heavy rainfall in T42 is not found in Fig. 5. This is because the SST is specified in Fig. 1 but the result in Fig. 5 is provided by the coupled model. In contrast, there is no difference for T106 between Fig. 1 and Fig. 5. This suggests that the SST is well maintained by the high resolution climate model.

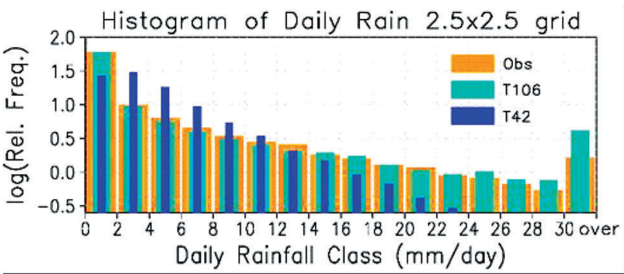

Fig. 5 Histogram of daily rainfall over the 2.5 degree by 2.5 degree region around Japan from the high-resolution (green) and the medium resolution (blue) climate models.

4. Impacts of high resolution

4.1 Global Features

As the high-resolution global model produces huge amount of data, it is almost impossible to summarize its impact over all fields in this paper. As is described in the introduction, it is expected that the local impact would be greater than the global impact. Then, the impact on the global features of the atmosphere is briefly summarized. Readers who are interested in other aspects may refer to other papers (Emori et al, 2005a; Takemura et al., 2005; Inatsu and Kimoto, 2005; Hirota et al., 2005). Impacts on the ocean have been analyzed by Oka and Hasumi(2006) and Suzuki et al.(2005).

Although there are many methods to evaluate performance of a climate model, we have used a Taylor diagram, which represents RMSE (Root Mean Square Error) and anomally correlation, as a measure of the global performance of the climate model. Many variables are included in the model and it is, therefore, difficult to compare all the variables. Here, we select the following variables, such as 2 m temperature (Sat), sea-level pressure (Slp), zonal wind (U250) and meridional wind (V250) at 250 hPa, geopotential height (Z500) at 500 hPa, temperature at 850 hPa (T850), relative humidity at 700 hPa (RH700), specific humidity at 700 hPa, cloud cover (Ccover), Precipitation (Prcp), outgoing longwave radiation at TOA (Top Of Atmosphere), outgoing shortwave at TOA, LW (Long Wave) cloud forcing and SW (Short Wave) cloud forcing. The Taylor diagrams of these variables in the control run have been computed for the annual and seasonal means. It is noted that some variables, such as Z500 and U250, are better represented in the high resolution model, but others are not. These features differ with the season and it is difficult to say that the high-resolution climate model is better, overall, than the low-resolution model. However, during December, January and February (DJF), most variables are better in the high resolution model (see, Fig. 6).

In general, the large-scale variables relating to dynamic factors, such as a zonal wind at 200 hPa, and geopotential height at 500 hPa, are better represented in the high resolution model. However, it should be noted that performance of the model results is not automatically improved, simply by increasing resolution. In order to achieve a better performance, careful tuning of physical processes in the climate model must be exercised.

4.2 Regional Features

Local climate features are expected to be well represented by using the high-resolution model. Therefore, impacts due to the increase in resolution are expected to be found in the local phenomena. As all of the regional cases cannot be described, a few examples are discussed

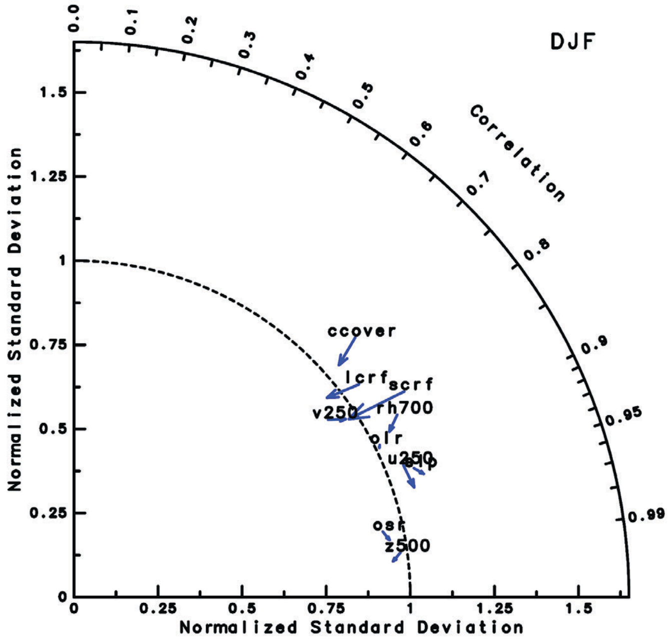

Fig. 6 Difference between the high resolution climate model and the medium-resolution model. Heads of arrows correspond to the high-resolution model and roots of arrows correspond to the medium-resolution model. Regarding variables, please refer to the text.

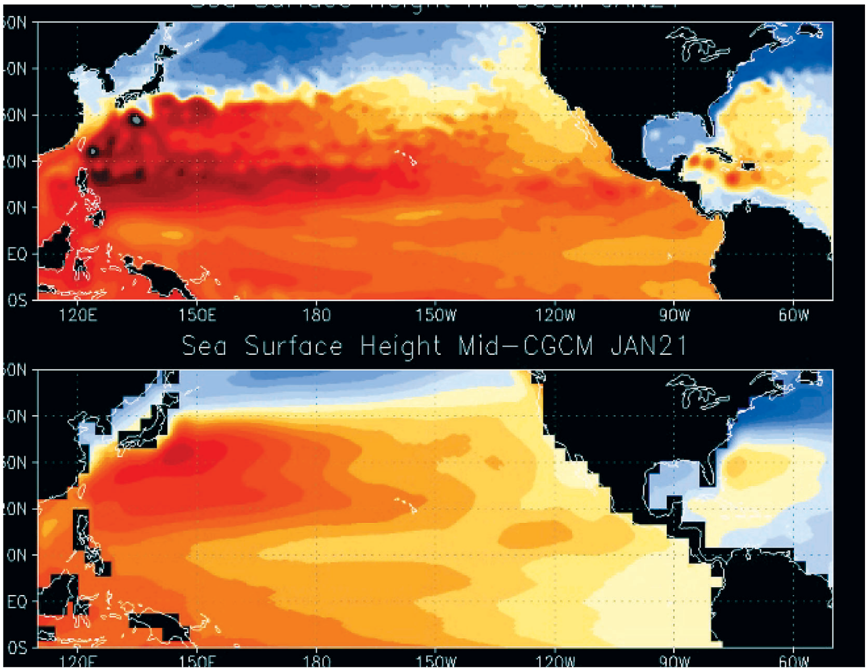

Fig. 7 Simulated ocean surface height, (Top) using the high-resolution climate model. (Bottom) using the medium-resolution model.

here. One example is the interaction between an island or coast line, the atmosphere and the ocean. In Fig. 7, a sea-surface height distribution over the Pacific basin and in the Caribbean Sea, simulated by the high-resolution climate model (top) and medium-resolution model (bottom), are displayed. It is noted that many vortices, originating in the Hawaiian Islands, propagate westward to the Philippine Islands. Similarly, many vortices are found leeward of the islands in the Caribbean Sea. These vortices are excited by the wind fields on the lee-side of the Hawaiian Island and islands in the Caribbean Sea. It should be noted that these phenomena cannot be simulated by the medium resolution model (bottom), because these islands are not represented. Vortices are generated and propagated westward from the Hawaiian Islands, because oceanic vortex is excited by the wind, influenced by the Hawaiian Island mountain. This phenomenon has been observationally investigated by Xie et al. (2001) and this far-reaching effect of the Hawaiian Island in the sea-surface height, simulated by the high-resolution climate model, has been demonstrated by Sakamoto et al. (2004).

Another example is the behavior of the Kuroshio to the east of the Japan Island (Honshu). Here, we should recall that the sensitivity of resolution to the Kuroshio has been demonstrated in the stand alone OGCM experiments, with given wind stress (see, Section.2). In Fig. 8, the Kuroshio and SST off the Japan Island are presented using the high and the medium resolution models. In this figure, results from the high-resolution atmosphere model, coupled with each of the medium-resolution ocean model and the medium-resolution atmosphere model and the high-resolution ocean model, are also shown. By comparing the four figures, we can estimate impacts due to the horizontal resolution. In the cases of the medium resolution models (hAmO and mAmO), the Kuroshio current tends to flow northward along the Japan Island. By contrast, the Kuroshio tends to depart from the Japan Island and flows eastward in a meandering fashion in the high-resolution ocean model. The mechanism of the Kuroshio separation has been the subject of discussion and the shape of the coast line of the Japan Island is considered to be critical (Mitsudera et al., 2005). As the

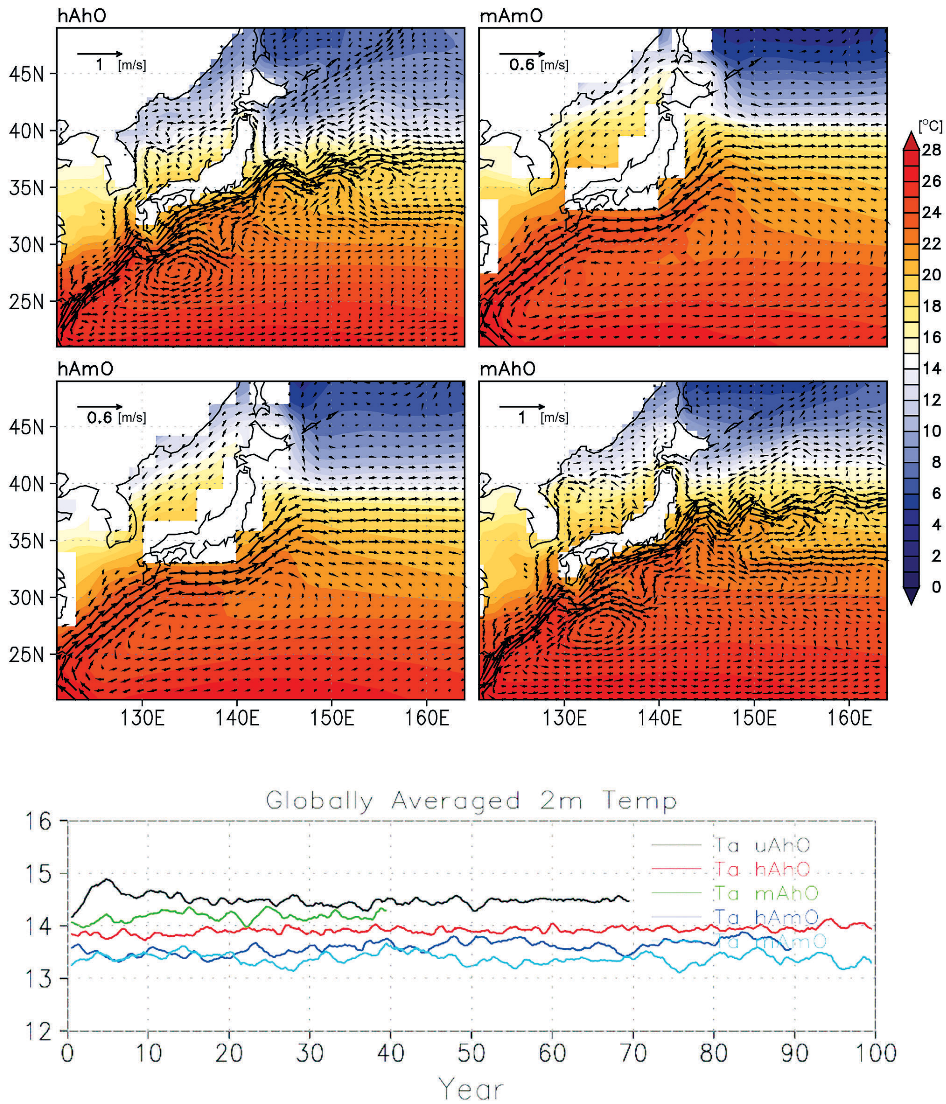

Fig. 8 (Top) Averaged SST and ocean currents around the Japan Islands in hAhO (top left), mAmO (top right), hAmO (bottom left) and mAhO (bottom right). Explanation of hAhO, mAmO, hAmO, mAhO is given in the text. (Bottom) Time sequence of the globally averaged 2 m temperature of hAhO, mAmO, hAmO, mAhO and uAhO. uA corresponds to T213AGCM.

coast line of the Japan Island is well represented in the high resolution model, the Kuroshio separation is also considered to be well represented in the high resolution model. This result is also suggested by the OGCM experiments. The Oyashio current has also been simulated around the Hokkaido with the high resolution climate model (hAhO), although it is difficult to simulate in other cases (mAmO, hAmO and mAhO). This difference is considered to stem from the difference of wind stress over the northern Pacific Ocean.

It is noteworthy that little drift is found when component models are interchanged. In Fig. 8 (bottom), the global averaged 2 m temperature is displayed, resulting from the five models (uAhO, hAhO, hAmO, mAmO, and mAhO). Here, uA denotes T213L56AGCM. Although the global averaged surface temperature is not the same in each run, there is no drift. This means that once energy balance and water balance in each component model is realized, a model, coupling these components tends to show little drift. As air-sea interaction is dependent on resolution, the globally averaged surface temperature is not the same. If we wish to simulate with the same resultant value, a little tuning is necessary.

It is concluded that the behavior of the Kuroshio Current is mainly determined by the resolution of the ocean model. However, the horizontal resolution of the atmosphere plays an important role in the heat exchange between the atmosphere and the ocean.

When we compare hAhO with mAhO, SST in hAhO is cooler that that in mAhO. A similar result is obtained, comparing hAmO and mAmO. When we use the high resolution atmosphere model, the smaller scale and high frequency components of air-sea interaction can be represented, explaining the reason for the above. Thus, it should be noted that air-sea interaction is sensitive to horizontal resolution.

Another example is improvement in the simulation of high-frequency phenomena. In Fig. 9, standard deviations of daily precipitation during June and July are displayed. The top left panel is the standard deviation, estimated by satellite observation, whilst the bottom figures are estimates from the high-resolution climate model (middle) and the medium resolution climate model (bottom). It is clearly shown that high frequency variability along the Baiu front is improved in the high resolution run.

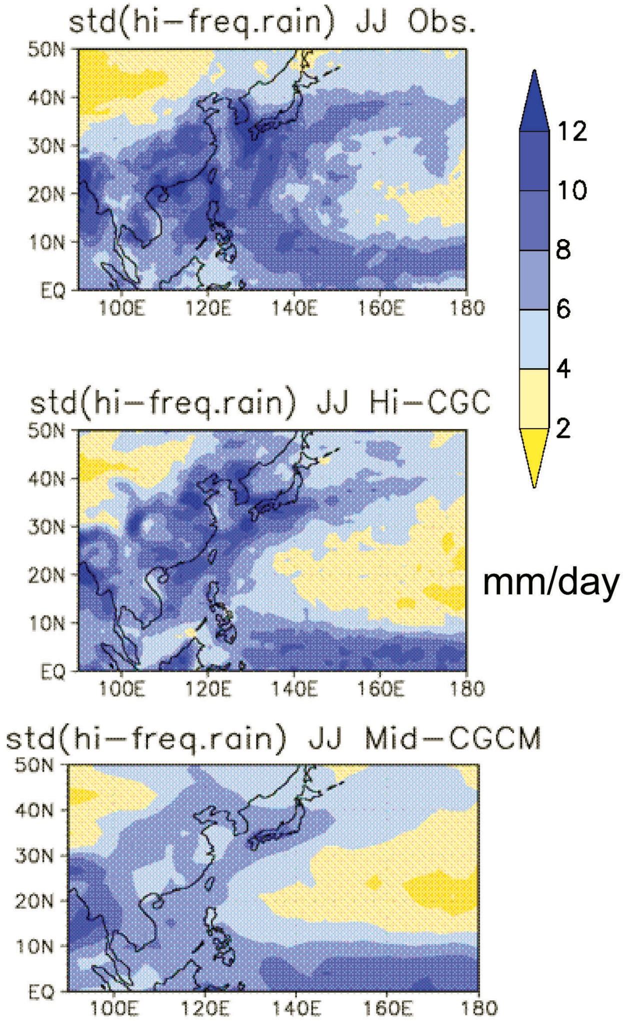

Fig. 9 Standard deviation of high-frequency (less than 10 days) rainfall in June and July, estimated by Satellite observation (top), and standard deviation in the high-resolution (middle) and the medium-resolution climate models (bottom). The results are averaged for 6 years of the control run.

5. Global warming simulation

Global Warming simulation has been conducted, using the high resolution and medium resolution climate models. In responding to requests by IPCC, simulations for IPCC AR4 have been conducted, in the form of (1) a control experiment, (2) 1% CO_2 increase experiment, (3) the 20^{th} Century Climate Change (203C) simulation, (4) an experiment with a mixed layer ocean and (5) IPCC SRES scenario run (A1B, A2 and B1). These results have been submitted to the IPCC Data Center and are available through the Data Center. These data are denoted as MIROC-hi and MIROC-low. In Fig. 10, the time-sequences are displayed for globally averaged surface temperature (Ts) in the different runs for IPCC AR4. Global aspects of the warming are similar to previous experiments, in that there is much warming in the high latitudes and over the continents. In this figure, results due to a stabilization scenario are also presented. Thick lines represent results from the high-resolution climate model and thin lines represent results from the medium resolution. It is noted that no drift exists in the control run of both models. In the 1% increase run, a similar increase

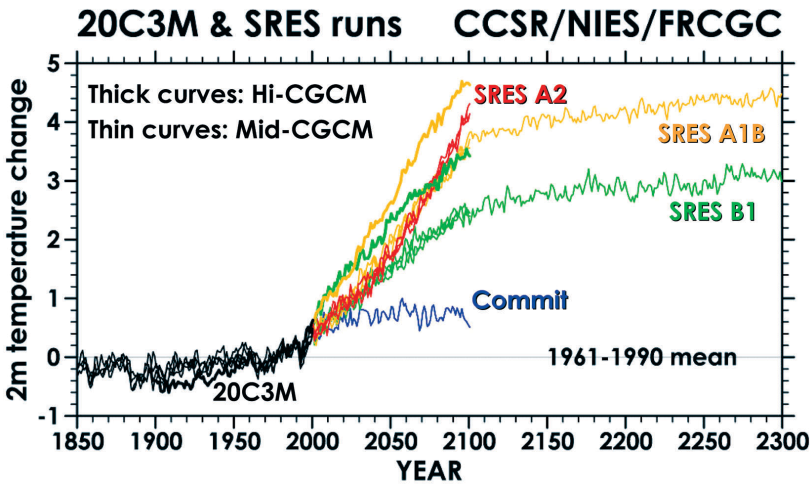

Fig. 10 Globally averaged 2 m temperature in the various IPCC runs (SRES A2, A1B and B1). Thick (thin) lines denote the high (medium)-resolution climate models, respectively.

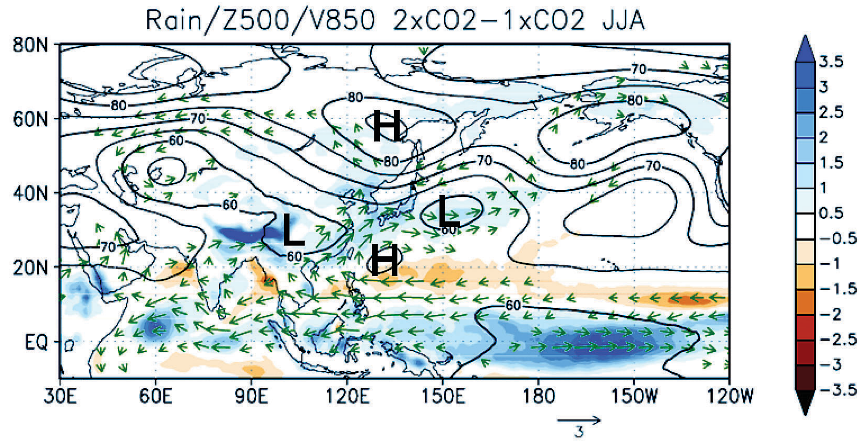

Fig. 11 Changes of precipitation field, geopotential height field at 500 hPa and wind field at 850 hPa, due to CO_2 doubling during June, July and August, over the East Asia. Unit is 10gpm for the geopotential height, and cold (warm) color corresponds to increasing (decreasing) precipitation.

in the surface temperature is noted, although a greater increase is found in the high resolution climate model (about 0.6 C after 70 years). This difference is considered to be due to difference in resolution. It is considered that the ice-albedo feedback effect and the ocean heat uptake is different in these two models (Yokohata, 2007).

New information regarding the regional impacts due to the Global Warming has been obtained with these simulations. One example relates to the climate change in the East Asia summer (see, Fig. 11). Both the subtropical high and the Okhotsk high are intensified. At the same time, the low pressure zone between these two high pressure systems is intensified, indicating that the rainfall intensity associated with the Baiu front becomes greater. It should be noted the days of heavy precipitation and days with no rain both increase. In conclusion, heavy rainfall and dry days are anticipated in the warmer climate (Kimoto et al., 2005). Furthermore, analysis of the change in heavy rainfall due to warming, using these data (Emori and Brown, 2005b), suggests that information regarding extreme events will, in future, be obtained using the high-resolution climate model.

Another example relates to the change in the Kuroshio Current. The Kuroshio separation is a prominent feature and the high-resolution climate model is able to simulate this separation (refer to 4.2). Fig. 12 shows ocean current and SST around the Japan Islands in the present climate simulation (top, left) and in the warmer climate (bottom left). In previous simulations we could not say anything about the change in Kuroshio Current because grid distance in the ocean model was so coarse and the Kuroshio Current was not well represented. However, the current model successfully simulates the Kuroshio Current around the Japan Islands. In the warmer climate, the currents

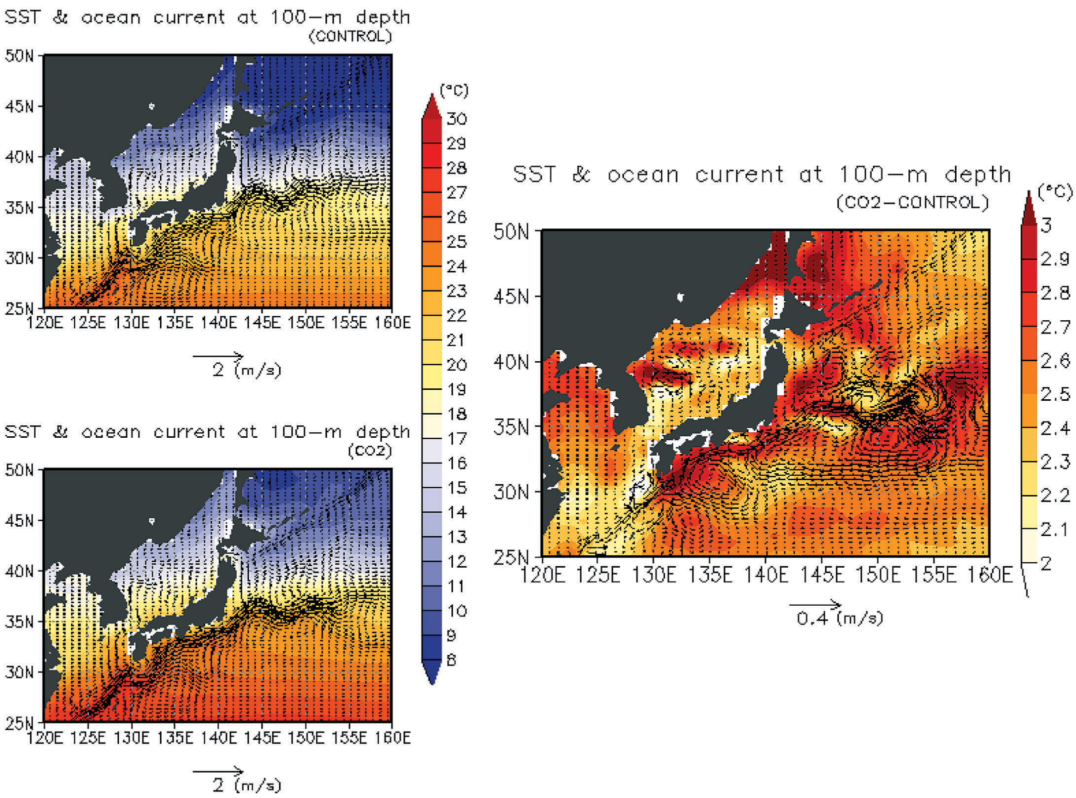

Fig. 12 SST and ocean current at 100 m depth in the control run (left top) and in the CO_2 doubling run (bottom left). The unit of current is 2 m/sec and the unit of SST is 1˚C. Difference between these two runs is displayed (right). The unit of current is 0.4 m/sec and the unit of SST is 0.1˚C.

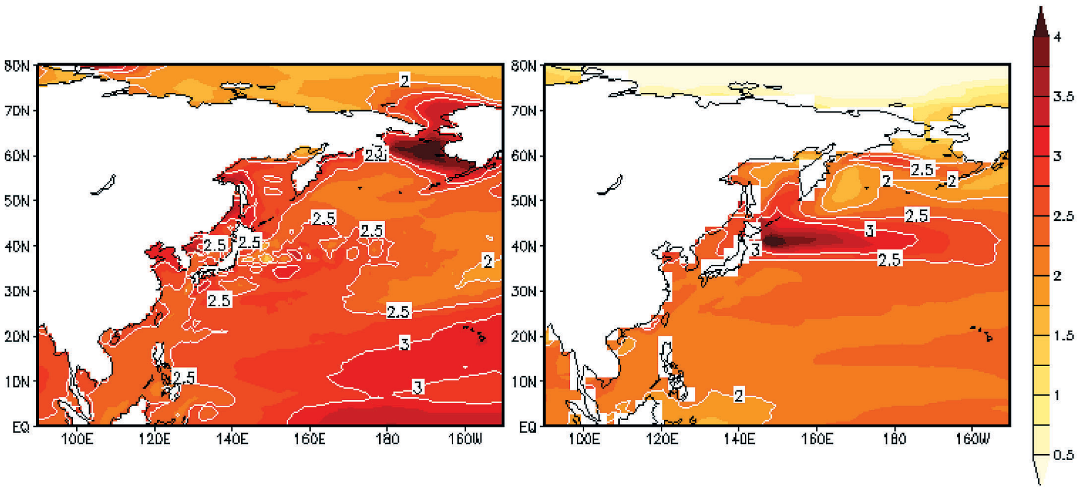

Fig. 13 The increase in SST from the CO_2 doubling run around the Japan Island, using the high resolution coupled model (left) and the medium-resolution coupled model (right).

around the Japan Island are similar to those in the current climate. However, current speed is intensified and SST is increased (right; Sakamoto et al, 2005). These results are very important to the investigation of the impact of the warming to fisheries around the Japan Islands.

Regarding the behavior of the Kuroshio Current around the Japan island, the SST anomaly due to CO_2 doubling tends differ with the model used. In the medium resolution model, the Kuroshio tends to flow northwards. However, the Kuroshio is separated from the Japan Island around 35N in the high resolution model. When Global Warming occurs, the Kuroshio tends to move further northwards in the medium resolution model, although the location of the Kuroshio extension remains at the same latitude in the high resolution runs. The differences in SST between 60–80 year averages in the 1% CO_2

increase run are shown in Fig. 13 for the high-resolution climate model, (left), and the medium-resolution model, (right). It is well noted that a large difference exists between two regions in the northern Pacific Ocean, east to the Japan (Honshu) Island. The difference in the Arctic region is due to the difference in the sea-ice distribution, which results from the difference in the performances between the two ocean components in the Arctic Sea. Thus, when we apply a time-slice method to this SST anomaly, the different results may be obtained, and it must be carefully examined to judge whether a given SST anomaly is reasonable, or not.

6. Summary

A high resolution climate model has been developed by CCSR, NIES and FRCGC researchers, because the Earth Simulator been made available to us. This model has approximately 100 km resolution in the atmosphere and 20 km resolution in the ocean. The interactive aerosol model is included and the direct and the first and second indirect effects of aerosols are all taken into account. Their performance for the present climate is better than that obtained from the medium resolution climate model. The general performance of the large-scale features is improved for many variables when the high-resolution climate model is used. However, more direct impacts are obtained for regional phenomena. For example, the influence of the Hawaiian Island on the north-west Pacific Ocean is clearly demonstrated. Regional climate, such as disturbances in the tropics and the Baiu front, is well simulated. Another important aspect is an improvement in the ocean current simulation. Behavior of the Kuroshio is well simulated.

It is quite obvious that increasing resolution does not automatically guarantee good performance. However, the results shown in this paper strongly suggest that the high-resolution climate model will provide us with many stimulating and interesting results. Firstly, there exists no climate drift without a flux correction. The globally averaged surface temperature and the sea-ice contents are maintained in the integration. Although the global average exhibits a cool bias, the amplitude of the annual cycle is the same as in the climatology. Secondly, when one component model (the high-resolution atmosphere model) is replaced by the other component model (the medium resolution atmosphere model), there are no biases to the atmosphere-ocean coupled model. These results suggest that, when careful treatment of each component model is undertaken, the coupled model shows little climate drift.

However, there remain many problems, most of which are common to many of the climate models. We need to develop many aspects within a climate model. In general, it is concluded that the performance of the high resolution climate model is promising, and increasing the resolution in the climate model is one direction for the strategy in future developments of a climate model.

The Global Warming simulation has been conducted by using these models. The results have submitted to IPCC AR4. The global aspects are similar to previous experiments, but new findings for regional climate change have been obtained. For example, it is shown that rainfall activity, associated with the Baiu, front will be intensified in the climate of the future. Another example is a change in the Kurosio current around the Japan Islands. It is particularly important that the impact of the Global Warming on the marginal sea region is obtained, using the high-resolution climate model, because the environmental change in the marginal sea region is very important to society. It is concluded that, in order to consider the regional climate change due to the Global Warming, the high resolution climate model, described in this paper, is indispensable.

Acknowledgements

The author should express sincere thanks to members of the K-1 project (listed in Table 2). Allocation of the resources of the Earth Simulator was critical for this study and special thanks is conveyed to Dr.Tetsuya Sato, the Director of the Earth Simulator Center. This research was funded by the MEXT (Ministry of Education, Culture, Sports, Science and Technology).

(This article is reviewed by Dr. Takeshi Enomoto.)

Table 2 Members of the K-1 project.

CCSR	Masahide Kimoto, Hiroyasu Hasumi, Ken Oka, Ayako Abe, Teruyuki Nakajima, Masaaki Takahashi, Yukari Takayabu
NIES	Seita Emori, Toru Nozawa, Tatsuya Nagashima, Tokuta Yokohata, Hideo Shiogama
FRCGC	Tatsuo Suzuki, Takeshi Sakamoto, Akira Hasegawa, Yoko Tsushima, Fuyuki Saito, Teruyuki Nishimura

References

[1] S. Emori, A. Hasegawa, T. Suzuki, and K. Dairaku, Validation, parameterization dependence, and future projection of daily precipitation simulated with a high-resolution atmospheric GCM, *Geophys. Res. Lett.*, vol.**32**, L06708, doi:10.1029/2004GL022306, 2005.

[2] S. Emori and S. J. Brown, Dynamic and thermodynamic changes in mean and extreme precipitation under changed climate, *Geophys. Res. Lett.*, vol.**32**, L17706, doi:10.1029/2005GL023272, 2005.

[3] N. Hirota, M. Takahashi, N. Sato, and M. Kimoto, Change of the Baiu Season Climate in the East Asia During 1979 to 2003, *SOLA*, vol.**1**, pp.137–140, 2005.

[4] M. Inatsu and M. Kimoto, Difference of boreal summer climate between coupled and atmosphere-only GCMs, *SOLA*, vol.**1**, pp.105–108, doi:10.2151/sola. 2005-028, 2005.

[5] Y. Kawatani and M. Takahashi, Simulation of the Baiu front in a High resolution AGCM, *J. Met. Soc. Japan*, vol.**81**, pp.113–126, 2003.

[6] K-1 Model Developers, K-1 Coupled Model (MIROC) description, *K-1 Tech Report*, ed by H. Hasumi and S. Emori, 34pp, Center for Climate System Research, Univ. of Tokyo, 2004.

[7] M. Kimoto, Private communication, 2002.

[8] M. Kimoto, N. Yasutomi, C. Yokoyama, and S. Emori, Projected changes in precipitation characteristics around Japan under the global warming, *SOLA*, vol.**1**, pp.85–88, doi: 10.2151/sola. 2005-023, 2005.

[9] H. Nakano and H. Hasumi, A series of zonal jets embedded in the broad zonal flows in the Pacific obtained in eddy-permitting ocean general circulation models, *Journal of Physical Oceanography*, 2003.

[10] A. Oka, and H. Hasumi, Effects of model resolution on salt transport through northern high-latitude passages and Atlantic meridional overturning circulation, *OCEAN MODELLING*, vol.**13**, no.2, pp.126–147, 2006.

[11] T. T. Sakamoto, A. Sumi, S. Emori, T. Nishimura, H. Hasumi, T. Suzuki, and M. Kimoto, Far-reaching effects of the Hawaiian Islands in the CCSR/NIES/FRCGC high-resolution climate model, *Geophys. Res. Lett.*, vol.**31**, L17212, doi:10.1029/2004GL020907, 2004.

[12] T. T. Sakamoto, H. Hasumi, M. Ishii, S. Emori, T. Suzuki, T. Nishimura, and A. Sumi, Responses of the Kuroshio and the Kuroshio Extension to global warming in a high-resolution climate model, *Geophys. Res. Lett.*, vol.**32**, L14617, doi:10.1029/2005GL023384, 2005.

[13] T. Suzuki, T. T. Sakamoto, T. Nishimura, N. Okada, S. Emori, A. Oka, and H. Hasumi, Seasonal cycle of the Mindanao dome in the CCSR/NIES/FRCGC atmosphere-ocean coupled model, *Geophys. Res. Lett.*, vol.**32**, L17604, doi:10.1029/2005GL023666, 2005.

[14] T. Takemura, T. Nozawa, S. Emori, T. Y. Nakajima, and T. Nakajima, Simulation of climate response to aerosol direct and indirect effects with aerosol transport-radiation model, *J. Geophys. Res.*, vol.**110**, D02202, doi:10.1029/2004JD005029, 2005.

[15] S. -P. Xie, W. T. Liu, Q. Liu, and M. Nonaka, Far-reaching effects of the Hawaiian Islands on the Pacific ocean-atmosphere system, *Science*, Vol.**292**, pp.2057–2060, 2001.

[16] T. Yokohata, S. Emori, T. Nozawa, T. Ogura, T. Suzuki, Y. Tsushima, M. Kawamiya, A. Abe-Ouchi, H. Hasumi, A. Sumi, and M.Kimoto, Different transient climate responses of two versions of an atmosphere-ocean coupled general circulation model, *Geophys. Res. Lett.*, vol.**34**, L02707, doi:10.1029/2006GL027966, 2007.

Journal of the Earth Simulator, Volume 9, March 2008, 51–63

Vectorization of Polygon Rendering for Off-line Visualization of a Large Scale Structural Analysis with ADVENTURE System on the Earth Simulator

Hiroshi Kawai[1], Masao Ogino[2]*, Ryuji Shioya[2], and Shinobu Yoshimura[3]

[1] *Faculty of Science and Technology, Keio University, 3-14-1 Hiyoshi, Kohoku-ku, Yokohama 223-8522, Japan*
[2] *Faculty of Engineering, Kyushu University, 744 Motooka, Nishi-ku, Fukuoka 819-0395, Japan*
[3] *Department of Quantum Engineering and Systems Science, The University of Tokyo, 7-3-1 Hongo, Bunkyo-ku, Tokyo 113-8656, Japan*

(Received June 14, 2007; Revised manuscript accepted March 13, 2008)

Abstract Using ADVENTURE system, a 3-D structural analysis of a very large scale problem can be performed on supercomputers such as the Earth Simulator (ES). However, the data size of the analysis results also becomes huge. We developed an off-line visualizer for visualization of a huge scale 3-D structural analysis on ES. The off-line visualizer performs rendering of surface patch triangles to produce image files of deformation plot and stress contour plot. It is vectorized. The vectorization scheme of its polygon rendering using a look-up table is explained in detail, and its performance evaluation on ES is carried out. It is also demonstrated that a 3-D structural analysis over 200 millions DOFs can be visualized efficiently using our off-line visualizer.

Keywords: Visualization, polygon rendering, vectorization, FEM, structural analysis

1. Introduction

A variety of distributed-parallel supercomputers, such as the Earth Simulator (ES), IBM BlueGene/L, Cray X1E, Hitachi SR11000 and SGI Altix, are available for a heavy-load numerical simulation task. Using those computational servers, a simulation user can perform a huge scale 3-D solid structural analysis based on the finite element method, whose degrees of freedom exceed 100 millions [1].

For example, currently, we are planning an earthquake response simulation of a full-scale nuclear power plant. In this simulation, a solid Finite Element (FE) model over 200 million Degrees Of Freedom (DOFs), which represents a whole nuclear pressure vessel, is employed. It contains lots of structural details, such as nozzles, pipes, control rods and other support structures. It takes just a few hours to execute a dynamic analysis job on ES.

However, each analysis task produces gigantic analysis result data files, which may occupy a disk space size of terabytes order. Because of this size issue, it is difficult and time consuming for the simulation user to move those analysis result data files back to his or her workstation for visualization purposes. Although the visualization capability of a workstation or a PC terminal on the client side still remains an issue, the low network speed between the computational server and the client terminal is also a serious issue against the huge scale visualization.

Including ES, there are a couple of computational servers in the world, with an unprecedented level of computational power. Ideally, such an extremely powerful supercomputer should not be dominated by any single organization, and it should be shared among many users nationwide, including researchers at universities, national research centers and research sections in the industries, or, if possible, worldwide also. In this case, those users should not be forced to only visit the supercomputer center directly and stay inside the center building while using the supercomputer, but it is also desirable for them to use the supercomputer remotely from their own laboratories far away from the supercomputer center. This implies that there should be some effective ways to access the supercomputer over the Internet. Remote visualization should also be considered seriously in this context.

Actually, in the Earth Simulator Center (ESC), there are some graphics workstations. Each of them has a dedi-

* ***Corresponding author****: Masao Ogino, Faculty of Engineering, Kyushu University, 744 Motooka, Nishi-ku, Fukuoka 819-0395, Japan. E-mail: ogino@mech.kyushu-u.ac.jp*

cated 3-D graphics hardware and OpenGL library, and they are connected to ES through the local area network called ES-LAN. There is also virtual reality equipment in the ESC called BRAVE and its software package called VFIVE [2]. However, to use these graphics workstations and the virtual reality environment, we have to visit the ESC. It is more convenient to perform our visualization tasks over the Internet, using a client PC in our laboratories. Of course, because the Internet is far slower than ES-LAN, it usually takes days or weeks to move our analysis result data files back into our laboratories.

Here in this paper, we assume that the average transmission speed through the Internet is currently about 100 M bps or less, based on the number measured actually between the ESC at Yokohama, located at the east region of Japan, and our laboratories in Kyushu University at Fukuoka, located at the south region of Japan. There are many routers on the communication path. The network is unstable, and some extra efforts are usually required to guarantee the completion of long-term data transfer for more than one day.

In this paper, we explain about our implementation of a server-side visualizer running on ES, one of the most powerful computational servers in the world, for a 3-D solid structural analysis using the finite element method.

After a huge scale FE analysis finishes, the visualization of the analysis result data is performed at the post-processing stage. Two of the most important visualization techniques for a structural analysis are a scalar contour plot and a deformation plot. In case of a 3-D solid problem, a contour plot of stress or strain distribution over the surface of the analysis model is drawn. It may also be combined with a deformation plot, which renders a displacement vector distributed over the model surface. This type of visualization, which belongs to surface rendering in a classical categorization of scientific visualization, is the main target of our research. If the FE analysis is dynamic, animation is also required.

To visualize a surface contour and deformation plot efficiently, it is necessary to obtain the boundary surface information of the 3-D solid FE mesh. It is called the 'surface patch' of the mesh. In case of using tetrahedral solid elements, which are often used to model a complicated 3-D solid structure, the surface patch is composed of triangles. Of all 4 triangular faces of all the tetrahedral elements, only the triangles just on the surface boundary of the mesh are collected and compose the surface patch.

Usually, it is time-consuming to extract the surface patch from a given huge scale structural model. Fortunately, the surface patch has already been extracted from the analysis model before the post-process stage begins, because this information is also required to specify loads and constraints at the pre-process stage.

At this stage, we have mainly two ways to visualize the huge analysis result data. One is to generate on the computational server only intermediate data to represent mainly the geometry information, and then, transfer and visualize them on a remote client PC. The other is to generate a final image data directly on the server.

In case of the former approach, first, triangles are generated from the surface patch and its associated analysis result data on the computational server. Then the generated geometry data are sent over the Internet from the ESC to our university. In our laboratory, the geometry data can be visualized interactively, using the powerful graphics hardware in an ordinary client PC. We can pan, zoom and rotate those triangles.

However, there are still some problems in this former approach. Except for viewing parameters, anytime we need to change any of the visualization parameters, such as contour type and range, vector magnification ratio, as well as selection of physical quantity types and their evaluation schemes related to structural analyses, new geometry data may have to be re-generated at the computational server. Moreover, in case of a dynamic analysis with many time steps, the amount of geometry data transferred through the Internet becomes huge. It is also mentioned as a serious issue in the reference [3]. For example, let us consider about our earthquake simulation of a nuclear pressure vessel model, with 200 M DOFs and 1000 time steps. Before sending the data over the Internet, we first extract only the relevant portion of the result data on the surface boundary of the model as an enriched geometry model, which is dedicated for our visualization purpose. Then, the extracted data are converted into a binary format called ADVENTURE I/O [4], and the data are compressed also. Usually, the size of the enriched geometry data, limited on the model surface only, can be reduced into about one tenth of the size of the whole original analysis result data. Even using those data on the surface patch only, it still takes a few days to transfer them over the slow Internet.

In the latter approach, instead of geometry data, image or animation data are generated directly on the computational server. Only those image data are sent to our laboratories. The size of the data is usually small, an order of M bytes or less. Obviously, the drawback of this approach is that, when the animation data are shown on a client PC, except time step parameters, all the visualization and viewing parameters have already been fixed and we cannot change them interactively.

We think both of two approaches are useful. While waiting for huge amount of extracted geometry data on the model surface coming from the ESC over the Internet, we can browse through image data generated by our off-line visualizer and monitor the status of the analysis job running at the same time. Once the geometry data have come, then using a PC on the client-side, we can dive into the model to search more detailed information thoroughly in an interactive environment, using walkthrough visualization techniques [5]. In this paper, we focus on a visualization technique on the server-side based on the latter image generation approach.

Originally, the keyword, 'off-line rendering', often used in the computer graphics field, means non-interactive image generation. It is different from 'interactive rendering' in front of the monitor screen of a graphics workstation through mouse and keyboard operations. In some computer graphics studio companies, off-line rendering may be performed using a PC cluster or a supercomputer. Here, we use this keyword as image generation for scientific visualization on a supercomputer.

The concept of off-line visualization is shown in Fig. 1. For example, a user may invoke the off-line visualizer from a remote terminal using the time-sharing system mode of a supercomputer, or the off-line visualizer may be executed as a batch job through the job manager. In either case, the visualizer reads the result data files and performs image rendering on the supercomputer. It produces image files or animation files rather than 3-D interactive graphics on a monitor screen.

Further, to implement this image generation approach actually, we can use either surface rendering or volume rendering.

In case of the volume rendering approach, usually, ray tracing or ray casting are used. There are some research such as Max [6] and GeoFEM/HPC Middleware [7] [8]. An image is generated directly from the surface patch and its associated result data, in a pixel-wise manner.

In case of the surface rendering approach, not only triangle geometry data are generated, but also an image is rendered from those temporary triangles. Rendering of the image from the triangles is performed using a triangle rasterization algorithm in a triangle-wise manner. Both triangle and image generation processes are performed on the computational server.

We have chosen the latter surface rendering approach, because this approach is fully compatible with most of the visualization methods and existing applications used in the structural analysis field. It is relatively easy to port an existing visualization application on ES, by simply switching an implementation of the 3-D graphics portability layer, such as [9], inside the application code.

In summary, the essential task of our off-line visualizer

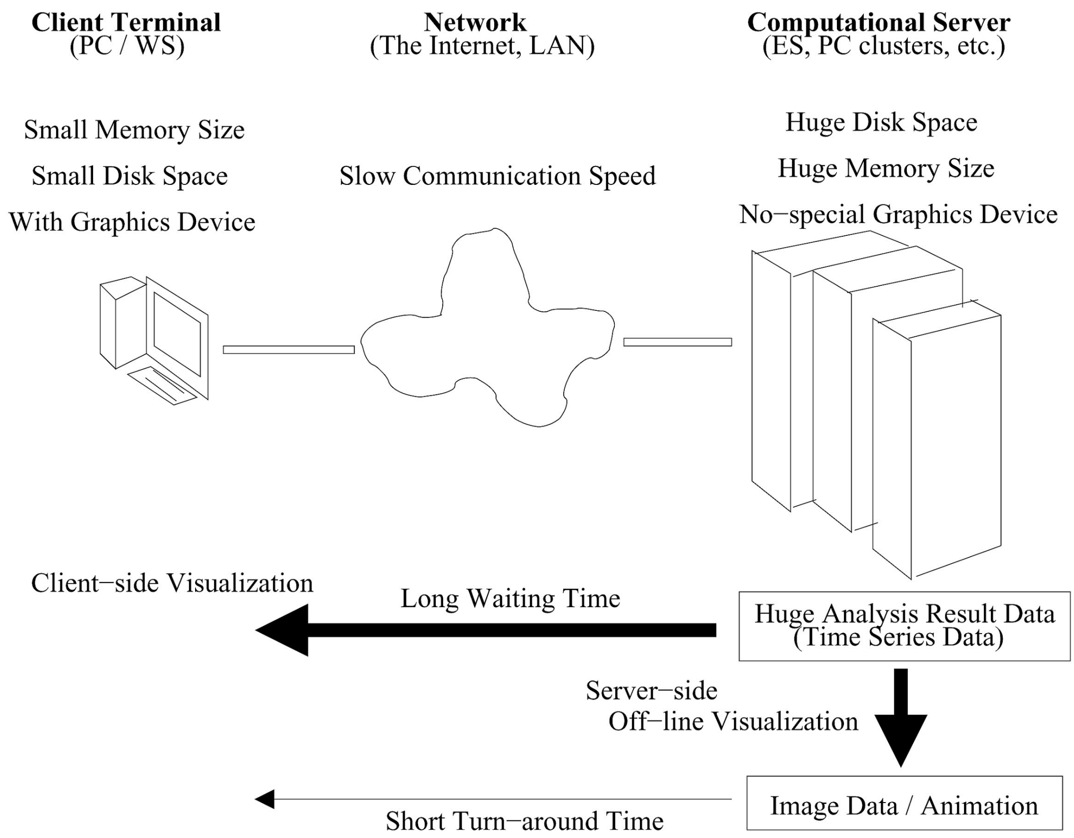

Fig. 1 Off-line visualization on a computational server.

is, to render a huge amount of triangles forming the surface patch, which has already been extracted. This means, we need a polygon renderer running on the supercomputer. A deformation plot can be rendered as a set of deformed triangles of the surface patch reflecting the displacement vector. A scalar contour plot can also be rendered using one dimensional texture mapping.

In this approach, however, we have to prepare a pure software-based polygon renderer running on ES. Most of the supercomputers, including ES, have no dedicated 3-D graphics hardware. It is also possible that no 3-D graphics library is available, or its implementation is not effcient even if available. Furthermore, because ES is a vector-parallel type architecture supercomputer, the polygon renderer should be both vectorized and parallelized.

As for the parallelization of the polygon rendering, there are already several methods available. Molnar [10] classified parallel rendering algorithms into three categories, sort-first, sort-middle and sort-last. The sort-first approach is used mainly for an existing sequential application to parallelize only its rendering part. This approach is usually implemented as the substitution of a 3-D graphics library from the sequential version to the parallel one. Nowadays, the sort-middle approach is used only for the implementation of new graphics hardware, because it requires heavy communication.

For most of the applications already parallelized based on domain-decomposition, including our case, the sort last approach is suitable. This approach generates an image domain-by-domain, then these domain-wise images are collected into the master process, and they are composed into a final single image. For the surface rendering without transparency, depth buffer information is used for the image composition. In our system, we use a binary-tree communication approach [5].

Therefore, the only remaining issue is, how to vectorize the polygon rendering process for a vector-type processor. There are some approaches, such as RVSLIB [11] [12], PATRAS [13] and MovieMaker [2], to utilize simply an existing implementation of triangle rasterization available for scalar-type processor. However, in these approaches, the rendering process can become a performance bottleneck on a vector-type supercomputer. It is especially true if the rendering task is also executed within the analysis process, or in the same large-scale batch job.

This paper focuses on this important missing part, vectorization of the triangle rasterization, which runs on ES and generates image data of surface scalar contour and deformation plots using the pre-extracted triangle surface patch. The most significant feature of our approach is the usage of a look-up table to accelerate the triangle rasterization. It is necessary not only to vectorize the majority of the rendering code but also to minimize the performance cost at the remaining scalar bottleneck.

Here, our vectorized polygon rendering algorithm using the look-up table is explained briefly. At the first stage, it performs triangle-wise calculation. At the second stage, it performs triangle fragment-wise calculation. And at the third stage, it performs image pixel-wise calculation. There are two kind of object sorting in our algorithm. One is in the middle of the rendering process, at the transition between triangle-wise and fragment-wise calculations. The other sorting is at the last of the process, at the transition between fragment-wise and pixel-wise calculations. The look-up table reduces execution time of the former transition step, which is a scalar section and the main bottleneck of our algorithm. As far as we know, there seems to be no other research activities about vectorization of polygon rendering, although our algorithm has some similar points with those for SIMD machines [14] [15] [16].

One thing we assume is that almost all the triangles rendered at visualization of a huge scale 3-D structural analysis are very small, usually less than 10 by 10 pixels in the screen coordinate space. This assumption is the same as the one used in other research [14] [15]. Based on this assumption, our algorithm uses the look-up table for most of the triangles to perform in-out detection and generation of fragments at the scan conversion stage efficiently.

In this paper, the size of our look-up table is relatively large. It may occupy about tens or hundreds of M bytes. It is understandable that there has been no practical application using this sort of look-up table-based approaches ever before, because, until recently, such a table has been considered prohibitively large. However, now we think it is well acceptable, because the memory capacity per single processor of ES is 2 G bytes.

2. Polygon Rendering Algorithm

Here, we describe our polygon rendering algorithm in detail. Its vectorization on a vector type supercomputer such as ES is also explained.

The main functionalities of our polygon renderer currently supported are as follows.

- pan, zoom and rotate
- orthogonal projection
- lighting and shading (flat shading)
- hidden surface removal using a depth buffer
- triangle polygon fill
- smooth and band contours using 1-D texture mapping
- clipping by arbitrary section planes

2.1 General Rendering Procedure

Here, for convenience, we introduce a general procedure to render triangle polygons briefly. The procedure shown below is a classical one. As we did in this paper for a vector-type parallel computer, depending on the specific hardware configuration of each system, some modifications may occur.

1. With each triangle, coordinate transformation from the world coordinate system to the screen coordinate system is performed.
2. With each triangle, clipping is performed. Triangles outside the clipping volume are removed.
3. With each triangle, lighting calculation is performed and vertex colors are calculated.
4. With each triangle, scan conversion is performed and the triangle is decomposed into multiple fragments.
5. With each fragment, shading is performed and its color is interpolated among the color of three vertices.
6. With each fragment, depth test is performed for hidden surface removal. If the fragment passes the test, it is written into the corresponding pixel in the screen image.

We further explain about the triangle scan conversion process in more detail. It is shown in Fig. 2.

With a given triangle, which is already transformed into the screen coordinate space, the scan conversion process decomposes the triangle into multiple scan lines horizontally. Then, each scan line is further decomposed into multiple fragments vertically.

Here, these fragments are the pixels composing the triangle. Usually, only a portion of the fragments, which pass depth test using a depth buffer, is reflected into the corresponding pixels in the screen image.

2.2 Assumption

A few assumptions are made for the basic design of our polygon renderer. These assumptions are derived from the typical characteristics of surface patches of our 3-D solid structural analyses on ES, and the usage patterns of our off-line visualizer to render surface contour and deformation plots.

First, there are millions of triangles in the surface patch of a huge scale 3-D structural analysis with hundreds of millions DOFs. If the off-line visualizer is parallelized, each processor manages at least tens of thousands of triangles or more.

Second, most of the triangles rendered on the screen image is very small compared with the image size. When using a 1,000 by 1,000 resolution image, an average pixel size of triangles on the screen coordinate system is less than 10 by 10 pixels. The larger the analysis scale

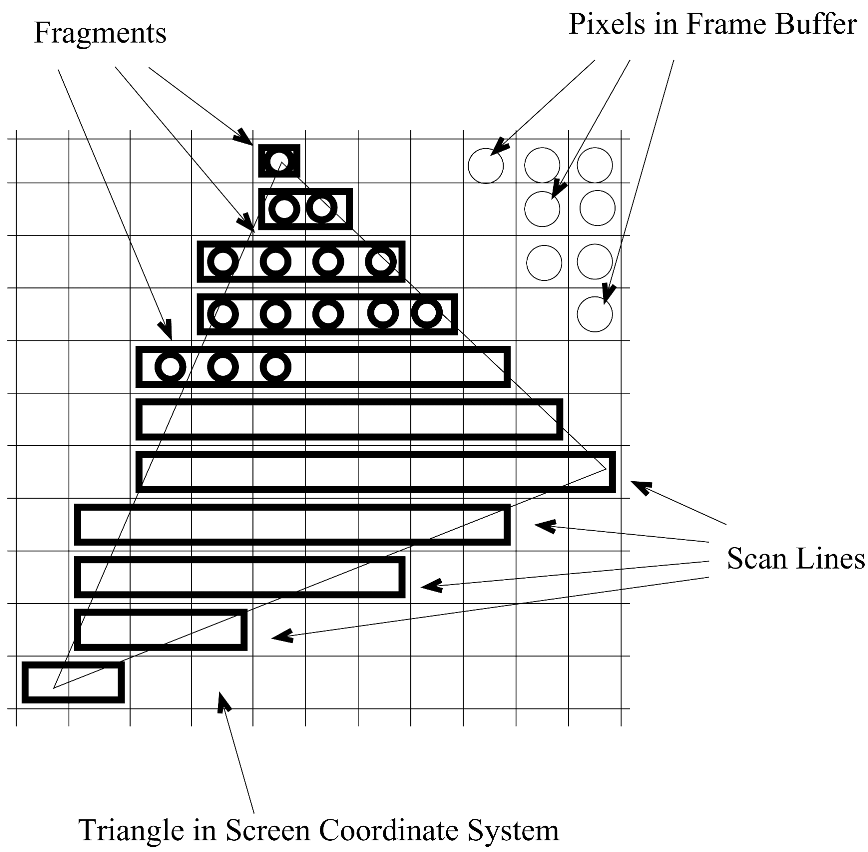

Fig. 2 A scan conversion of a triangle. A triangle is decomposed into multiple scan lines, then each scan line is decomposed into multiple fragments.

becomes, the more the number of triangles in the surface patch is, while the resolution size of the monitor screen on a client side terminal has kept almost constant in recent years, because of technical difficulties of LCD monitor production. Therefore, the average triangle pixel size will become smaller and smaller.

2.3 General Strategy

Based on the assumptions described above, our polygon rendering algorithm deal with only small triangles whose pixel size fits with the look-up table. Here, we call these triangles as 'table-fit' triangles.

Therefore, input triangles are divided into two groups, 'table-fit' or not. The criterion for this classification is the pixel size of each triangle. Usually, the size less than 10 or 20 pixels are classified as 'table-fit'. In case of our usage patterns, most of the input triangles in a surface patch are classified into the 'table-fit' group. The rest of the input triangles are processed using a conventional triangle scan conversion algorithm.

In vectorization, the vector loop length, which is the loop length of the inner most loop, is either the number of triangles or the number of fragments generated from those triangles. Usually, they are tens of thousands or more.

2.4 Triangle Coordinate System

Here, we introduce a keyword, a 'triangle coordinate system', for convenience of the discussions below.

At the coordinate transformation stage, a triangle defined in the world coordinate system is transformed finally into the screen coordinate system. The screen space is a 2-D XY integer value coordinate system.

Further, we transform the triangle from the screen coordinate system into the 'triangle coordinate system' of its own. The triangle coordinate system of a given triangle has the same scale and orientation as the screen coordinate system and its origin point is at one of the three vertices of the triangle. It is shown in Fig. 3.

Suppose there are three vertices in the triangle, v0, v1 and v2, respectively. In the triangle coordinate system of this triangle, the origin point is the position of vertex v0. Thus, the coordinate value at vertex v0 is (0, 0) in the triangle coordinate system.

The coordinate values of other two vertices, v1 and v2, are (tx1, ty1) and (tx2, ty2) in the triangle coordinate system, respectively. Each of these four coordinate component values, tx1, ty1, tx2, ty2, is an integer value and it may be positive, zero or negative. If the pixel size of the triangle is small, the component value fits within the cer-

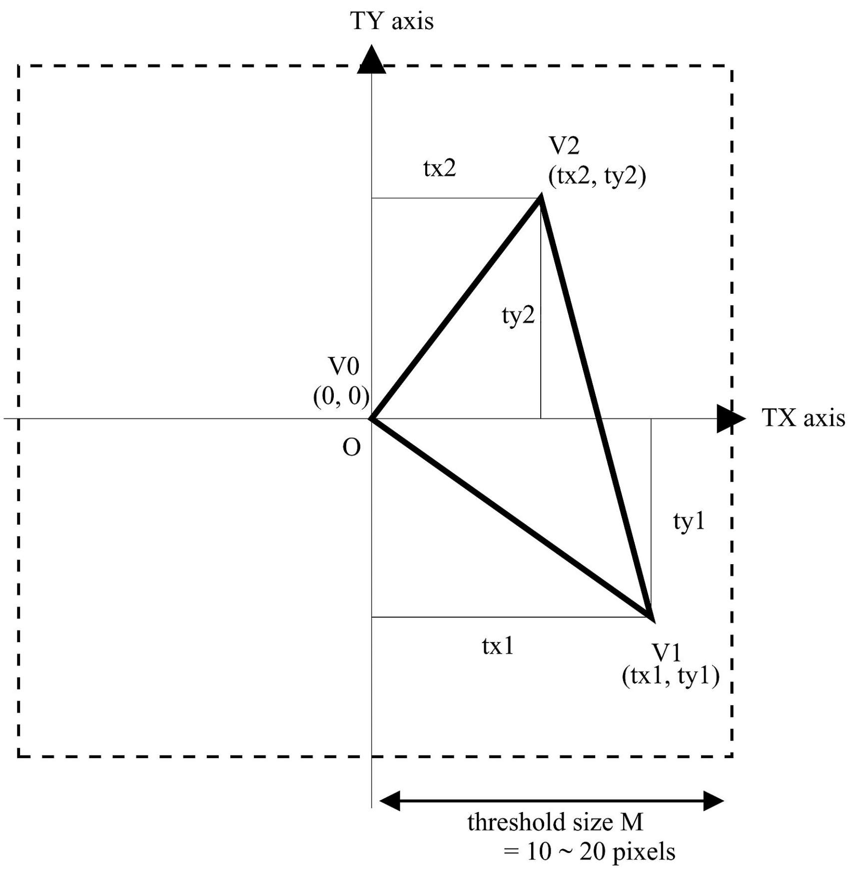

Fig. 3 Triangle coordinate system, which is a special system for assigning a triangle defined in the screen space.

tain range, for example, between –10 to 10, or between -15 to 15, or, at most, between –20 to 20 for most of the cases.

Any allowable combination of four coordinate component values, tx1, ty1, tx2, ty2, specifies the fill pattern of the corresponding triangle uniquely. The set of four integer values completely decides its scan conversion. Therefore, if we prepare all the fill patterns defined by all the combinations of these four values as a look-up table on memory, it can accelerate the scan conversion of a triangle of an arbitrary shape.

The number of all the possible combinations of four integer values is the maximum triangle pixel size powered by 4. It occupies a very large memory space. This threshold pixel size is limited by the allowable memory size of a user process of the off-line visualizer running on ES. Typically, we choose from 10 to 20 as the threshold pixel size. It is sufficient for most of our 3-D structural analysis cases.

As a more concrete representation of the look-up table, we store the beginning and ending TX indices of all the scan lines for each pattern.

Here is an example of a triangle, $tx1 = 10$, $ty1 = 4$, $tx2 = 4$, $ty2 = 10$, shown in Fig. 4.

The look-up table is organized as TX coordinates at the left and right end point of each scan line for each pattern.

In Fig. 4, TX values of the first scan line are from 4 to 4, those of the 2nd scan line are from 4 to 5, those of the 3rd scan line are from 3 to 6, and so on. If the threshold pixel size value is 10, the look-up table becomes the one listed as Table 1.

The memory size required to store a look-up table is proportional to the threshold pixel size powered by 5. A TX coordinate value can be stored as a signed integer of one byte. For example, if the threshold value is 10, 15, and 20, it occupies 6.4 M bytes, 49 M bytes and 205 M bytes, respectively.

Table 1 A Look-up table to define a triangle in a triangle coordinate system.

TY	start TX	end TX
10	4	4
9	4	5
8	3	6
7	3	7
6	2	8
5	2	9
4	2	10
3	1	8
2	1	6
1	1	3
0	0	1
-1	Null	Null
-2	Null	Null
.		
.		
.		
-10	Null	Null

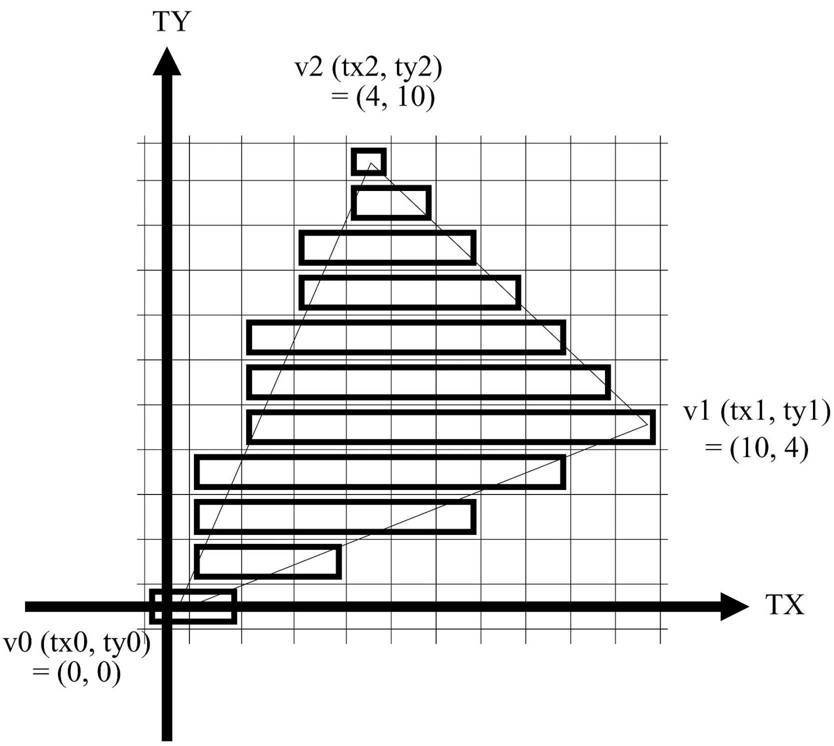

Fig. 4 Scan conversion of a triangle using a look-up table.

Here is a sample implementation code in C language of the definition of the look-up table, shown below.

```
#define MAX_TRI_SIZE 10

signed char ScanLineMinTx

[MAX_TRI_SIZE * 2][MAX_TRI_SIZE * 2]
[MAX_TRI_SIZE * 2][MAX_TRI_SIZE * 2]
[MAX_TRI_SIZE * 2];

/* -1 : no scan line */
/* or 0 ... (MAX_TRI_SIZE - 1) (include) */

signed char ScanLineMaxTx
[MAX_TRI_SIZE * 2][MAX_TRI_SIZE * 2]
[MAX_TRI_SIZE * 2][MAX_TRI_SIZE * 2]
[MAX_TRI_SIZE * 2];

/* -1 : no scan line */
/* or 0 ... (MAX_TRI_SIZE-1) (include) */
```

A constant parameter, MAX TRI SIZE, which is the threshold size, is specified as 10. There are two arrays of signed byte type, ScanLineMinTx and ScanLineMaxTx. The former 4 array indices represent tx1, ty1, tx2, ty2, respectively. The last 5th array index represent the TY value of each scan line. Each array occupies 3.2 M bytes. Note that all the TX values stored in these arrays and the TY value of each scan line are incremented by MAX TRI SIZE, so that a valid value becomes non-negative. If the value is –1, this scan line does not have to be filled.

2.5 Triangle-wise Calculation

The former part of our polygon rendering is triangle-wise calculation including coordinate transformation and lighting. It is performed for all the input triangles.

coordinate transformation and lighting For each vertex of each triangle, coordinate transformation and lighting are performed. Flat shading is used for the lighting calculation.

gradient for depth value and scalar interpolation For each triangle, the gradient vector of depth component in the viewing coordinate system, namely, Z value, is evaluated. If a contour plot is required, the gradient vectorof scalar value distribution over the triangle is also calculated.

pixel size and range in the screen coordinate system For each triangle, the pixel size and the range in the screen coordinate system are calculated. Triangle coordinates of vertices v1 and v2, and a set of four values, tx1, ty1, tx2, ty2, are also calculated.

classification of table-fit triangle If the pixel size of the triangle is less than the threshold value, it is classified as ’table-fit’.

As a result of these procedures above, only table-fit triangles are collected. Almost all of these procedures can be vectorized. The vector loop length is the number of the input triangles. It is long enough. Of all the computational load of polygon rendering, typically the half is on this side.

2.6 Scan Conversion

The latter part of our polygon rendering is the scan conversion stage. Here, we only explain how to deal with small triangles marked as ’table-fit’, because other big triangles are handled using a conventional algorithm. At this stage, fragments are generated from each of the ’table-fit’ triangles, and they are written down into image data.

fragment generation For each triangle, fragments are generated.

With the set of four coordinate component values, tx1, ty1, tx2, ty2, of the triangle, the corresponding section of the look-up table is referred. This section contains all the scan lines of the triangle fill pattern. Each scan line is represented as the TX coordinate component of the starting and the terminating end points. Using them, only fragments passing in-out detection are generated efficiently.

Fragments generated from multiple triangles are stored into the fragment pool of this vectorization session. Usually, tens of thousands fragments are stored at one session to keep the vector loop length long enough and save the workspace memory as minimum. Each fragment data store the source triangle ID where it originated, and its TX and TY coordinates in the triangle coordinate system of the source triangle.

This step is a scalar procedure. It is difficult to vectorize this step because a new fragment has to be checked one by one and added into data arrays. Owing to the look-up table, the number of arithmetic operations is minimized.

fragment calculation For each fragment, RGB color components and a depth value are calculated using the precalculated gradient values of the source triangle of the fragment.

On the color calculation, one dimensional texture mapping is used for producing a smooth contour or a band contour fill pattern.

Fragment-wise clipping check is also performed. Each fragment is tested against the range of image resolution as well as user-specified additional clip planes of arbitrary orientations.

This step can be fully vectorized. The vector loop length is the number of generated fragments in the fragment pool of this vectorization session. It is long enough.

fragment write For each fragment, the corresponding pixel in the image data is identified. Then, the depth value of the fragment and the one of the pixel, which is stored in the depth buffer, are compared. If it passes the depth test, the fragment color is written down into the image data at the pixel location.

This step is a scalar procedure. It is difficult to vectorize this step because of write dependency on the depth buffer.

The majority of the computational cost is spent on the fragment calculation step. Other two step, fragment generation and fragment write, cannot be vectorized because of data dependency. The look-up table is used to accelerate the former step.

Here is a sample implementation code in C language of the fragment generation, shown below. In this code section, arrays ScanLineMinTx and ScanLineMaxTx of the look-up table are used.

```
/* TC : triangle coordinate */

/* coordinate of vertex1 and vertex2 in TC */
int VecTri_v1Tc[2][MAX_TRIS];
int VecTri_v2Tc[2][MAX_TRIS];
/* box range in TC */
int VecTri_minTc[2][MAX_TRIS];
int VecTri_maxTc[2][MAX_TRIS];

/* the number of fragments */
/* in the fragment pool */
int NFragments;

/* triId : mapping from the fragment */
/* to source triangle */
int Fragment_triId[MAX_FRAGMENTS];

/* tx, ty : coordinate of the fragment in TC */
int Fragment_tx[MAX_FRAGMENTS];
intFragment_ty[MAX_FRAGMENTS];

void MakeFragment (void)
{
int iTri;

  /* NON-VECTORIZABLE LOOP */
  NFragments = 0;
  for (iTri = 0; iTri < NVecTris; iTri++) {
    int tx1 = VecTri_v1Tc[0][iTri];
    int ty1 = VecTri_v1Tc[1][iTri];

    int tx2 = VecTri_v2Tc[0][iTri];
    int ty2 = VecTri_v2Tc[1][iTri];
    int minTy = VecTri_minTc[1][iTri];
    int maxTy = VecTri_maxTc[1][iTri];

    int itx, ity;

    for (ity = minTy; ity <= maxTy; ity++) {
      int scanLineMinTx;
      int scanLineMaxTx;

      scanLineMinTx = ScanLineMinTx
         [tx1][ty1][tx2][ty2][ity];
      if (scanLineMinTx == -1) {
         continue;
      }

      scanLineMaxTx = ScanLineMaxTx
         [tx1][ty1][tx2][ty2][ity];

      assert(0 <= scanLineMinTx);
      assert(scanLineMinTx <= scanLineMaxTx);
      assert(scanLineMaxTx < MAX_TRI_SIZE * 2);

#pragma vdir novector
      for (itx = scanLineMinTx;
           itx<=scanLineMaxTx;
           itx++) {
        assert(NFragments< MAX_FRAGMENTS);
        Fragment_triId[NFragments]= iTri;
        Fragment_tx[NFragments] = itx;
        Fragment_ty[NFragments] = ity;
        NFragments++;
      }
    }
  }
}
```

Array VecTri_v1Tc stores the triangle coordinate (tx1, ty1) at vertex v0, and array VecTri_v1Tc stores (tx2, ty2)at vertex v1. Arrays VecTri_minTc and VecTri_maxTc are the box range of each triangle in its triangle coordinate system. The values in these arrays have already been filled in the previous steps.

Because the fragment generation step is a scalar process, the length of the inner loop in function MakeFragment is too short to be vectorized. All the fragments generated are stored into new arrays, Fragment_triId, Fragment_tx and Fragment_ty. They represent the source triangle ID, TX and TY coordinates ofthe fragment, respectively.

Here is a sample code section to evaluate the Z depth value at each fragment.

```
void CalculateFragmentDepth (void)
{
  int iFragment;

  /* VECTORIZABLE LOOP */
  /* containing indirect array reference */
  /* and read access */
  for (iFragment = 0;
      iFragment < NFragments;
      iFragment++) {
    int triId = Fragment_triId[iFragment];

    int tx = Fragment_tx[iFragment];
    int ty = Fragment_ty[iFragment];

    int dx = tx - MAX_TRI_SIZE;
    int dy = ty - MAX_TRI_SIZE;

    /* z value interpolation */

    float vz0 = VecTri_v0Dc[2][triId];

    float za = VecTri_za[triId];
    float zb = VecTri_zb[triId];

    float z = vz0 + za * dx + zb * dy;

    Fragment_zDc[iFragment] = z;
  }
}
```

Array VecTri_v0Dc stores the x, y and z component values at vertex v0 in the screen coordinate system. Arrays VecTri_za and VecTri_za are the gradient coefficients to specify the depth value distribution over the source triangle. The Z depth value of each fragment is stored in array Fragment_zDc.

All the fragment-wise loops, such as the code section in function CalculateFragmentDepth, are vectorized. If any data about the source triangle are required, the information is accessed using indirect index reference.

3. Performance Evaluation

For the implementation of our off-line visualization system, we used an open-source CAE system, ADVENTURE [4]. AutoGL library in ADVENTURE Auto module in ADVENTURE system is used for the implementation base of the polygon renderer [9].

Using this off-line visualizer, a performance evaluation is carried out on ES. Here, the vectorization performance of the polygon renderer running on a single processor of ES is shown.

As a benchmark problem, we prepared an artificial problem to render a scalar contour plot on semi-cylindricalsurface sheets. The model consists of 8 semi-cylindrical sheets placed in depth order and each of the sheets is composed of a 250 by 250 grid. In total, the surface patch is composed of 1 million triangles. The distribution of a scalar quantity over the semi-cylindrical sheets is artificially made so that the magnitude of the scalar value is proportional to the distance from the center of each sheet. Fig. 5 shows the benchmark model. In this case, the resolution of the imageis 1,000 by 1,000. An average pixel size of the triangles is about 5 by 5 pixels.

To render this image data on ES using a single Arithmetic Processor (AP), it takes 0.82 seconds to render 1 million triangles. Rendering performance of 1.22 million triangles per seconds is obtained. Acceleration ratio by vectorizationis about 4.2 times.

Here, as an example of the problem with a large number of triangles, a Pantheon model was performed shown in Fig. 6. Though detail of the model is described in the section 4, since the Pantheon model consists of about 4.1 million solid tetrahedron elements, total number of triangles amounts to 16.6 million when rendering in four faces of all elements. In rendering such large number of polygons model, our system achieved rendering performance of 2.33 million triangles per seconds, and acceleration ratio by vectorization of 4.9 times.

Next, we further investigated the performance bottleneck of our vectorized code using ftrace utility offered by the ESC. Table 2 and 3 show performance analysis of each rendering step using ES ftrace utility.

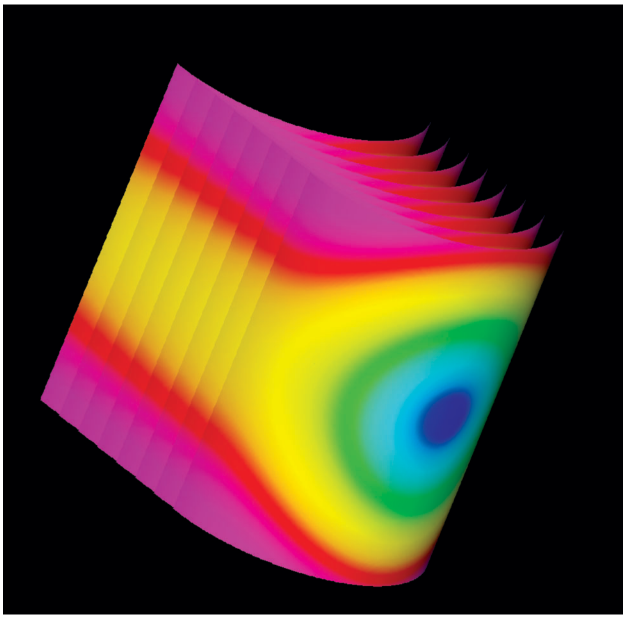

Fig. 5 Scalar contour plots on semi-cylindrical sheets as a benchmark problem, which has 1 million triangles.

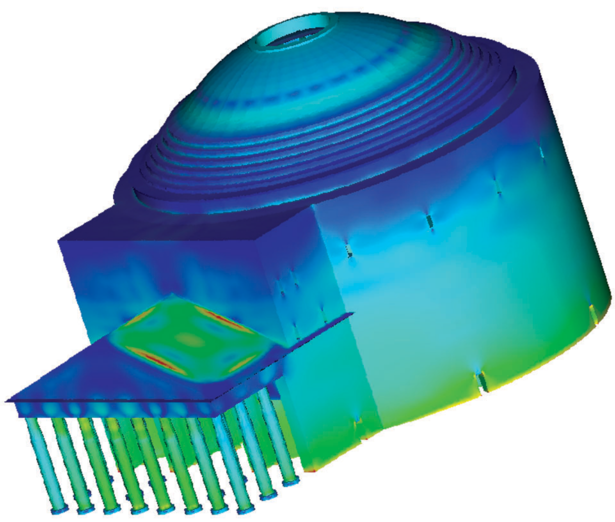

Fig. 6 Deformation and stress contour plots of a Pantheon model with 18 million DOFs.

Table 2 Performance analysis of rendering steps. In this table, Vec. means whether a step can be vectorized, and vec-off/on show runtime performances with vectorization off/on.

Rendering step	Vec.	Time vec-off (sec.)	Time vec-on (sec.)	Accel. ratio
transform and light	Y	0.982	0.043	24
clip triangle	Y	0.011	0.003	4
depth gradient	Y	0.121	0.010	12
scalar gradient	Y	0.172	0.015	12
range and TC	Y	0.197	0.008	26
collect table-fit	Y	0.314	0.053	13
generate fragment	N	0.289	0.288	1
interpolate z	Y	0.427	0.036	12
interpolate color	Y	0.617	0.068	9
write fragment	N	0.295	0.296	1

Table 3 Performance analysis of rendering a Pantheon model with 16.6 million triangles.

Rendering step	Vec.	Time vec-off (sec.)	Time vec-on (sec.)	Accel. ratio
transform and light	Y	10.712	0.663	17
clip triangle	Y	0.187	0.076	3
depth gradient	Y	2.154	0.171	13
scalar gradient	Y	2.901	0.216	14
range and TC	Y	2.615	0.149	18
collect table-fit	Y	4.100	0.798	9
generate fragment	N	2.693	2.687	1
interpolate z	Y	3.338	0.259	13
interpolate color	Y	4.661	0.581	8
write fragment	N	1.513	1.511	1

There are mainly ten rendering steps in our algorithm. All the steps before generate fragment step are triangle-wise vectorized calculations, and two steps, interpolate z and interpolate color, are fragment-wise vectorized calculations. However, fragment generation and fragment write steps, which are in the scan conversion stage, are not vectorized.

When run with vectorization off, no vectorized steps occupy 17 and 12 percents of total execution time in 1 million triangles and 16.6 million triangles model, respectively. With vectorization on, vectorized steps are accelerated about 10 times or more, while they remain the same. As a result, they are shown up as the bottleneck. The fragment generation step, which is accelerated by our look-up table approach, occupies about 71 or 59 percents of the bottleneck steps.

We also prepared a scalar-tuned version of the off-line visualizer, which is mainly intended for PC, WS and PC clusters. And, in rendering a benchmark model, the vectorized version is 4.3 times faster than the scalar-tuned version, when they are executed on ES. One reason is that the ES processor runs at 500MHz and its scalar performance is relatively slow compared with its vector performance. This means, it is still better to prepare a vectorized version optimized for ES or other vector machines than to bring a scalar version running on other scalar-processor platform and keep using it on ES.

4. Visualization Examples

Here, some visualization examples of huge scale 3-D structural analyses are demonstrated.

First, Pantheon in Roma, Italy is analyzed. The total DOFs in FE model is 18 million. The surface patch of the Pantheon model consists of 0.65 million triangles. A gravity force is applied as a body force. The result of elasto-static analysis is visualized using 8 APs of ES. Runtime performance of visualization with generating 100 image data from various angles is about 218 seconds. Fig. 6 and Fig. 7 are deformation and equivalent stress contour plots of a Pantheon model.

The next example is an earthquake response simulation of a full-scale nuclear power plant. It is a Boiled Water Reactor (BWR). The FE model contains 200 million DOFs. The surface patch consists of 16.7 million triangles. A horizontal acceleration force is applied as an earthquake load. The visualization with 100 images of elasto-dynamic analysis results is successfully performed in 7.5 minutes using 32 APs of ES. Fig. 8 and Fig. 9 are deformation and equivalent stress contour plots of a BWR model. In Fig. 9, the amount of deformation is magnified by 5,000 times.

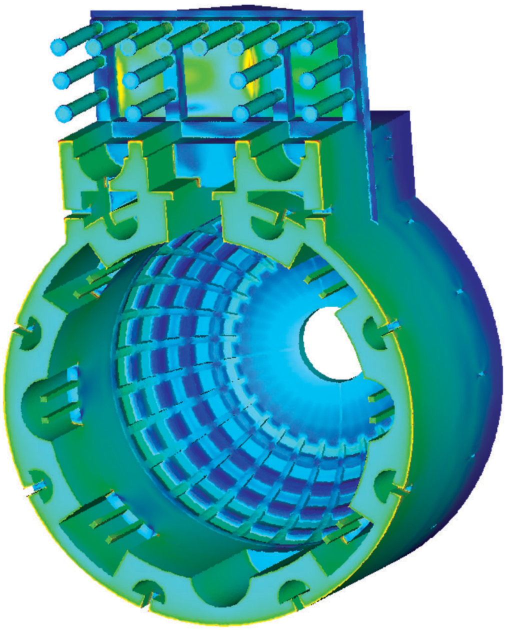

Fig. 7 Bottom view of a Pantheon model with deformed configuration and stress distribution.

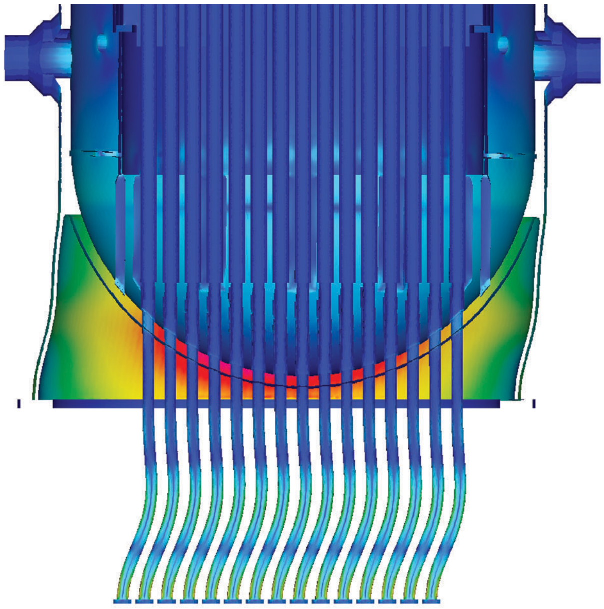

Fig. 9 Cross section around a skirt portion of a BWR model. The amount of deformation in this figure is magnified by 5,000 times.

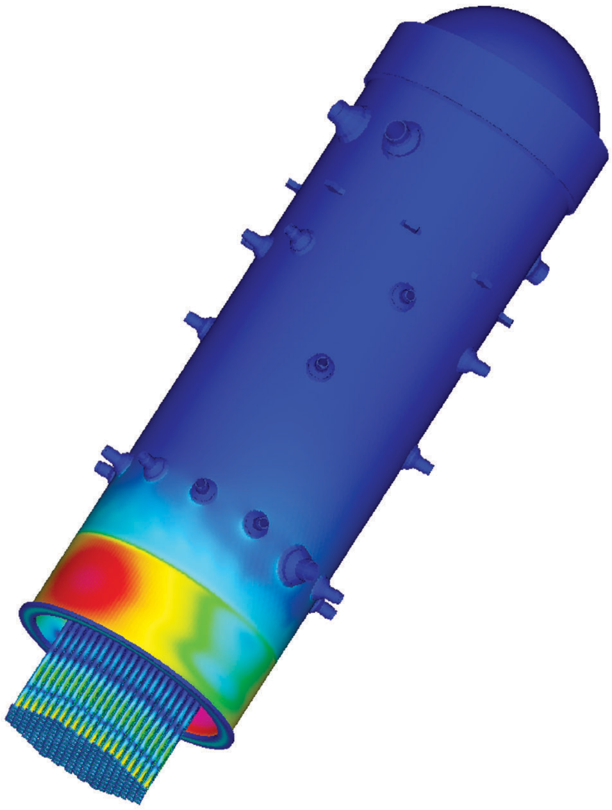

Fig. 8 Deformation and stress contour plots of a BWR model with 200 million DOFs.

5. Conclusions

An off-line visualizer is developed for visualization of a huge scale 3-D structural analysis on ES. The off-line visualize performs rendering of surface patch triangles to produce image files of deformation plot and stress contour plot. It is vectorized and parallelized. The vectorization scheme of its polygon rendering using a look-up table is explained in detail, and its performance evaluation on ES is carried out. Rendering performance of 1.22 million triangles per seconds is obtained per a single processor of ES. Acceleration ratio by vectorization is about 4.2 times. And it is 4.3 times faster than the corresponding implementation specially tuned for a scalar-type processor. It is also demonstrated that a 3-D structural analysis over 200 millions DOFs can be visualized efficiently using our off-line visualizer.

6. Acknowledgement

One of the authors (Hiroshi Kawai) was financially supported by The 21st Century COE Program, 'System Design: Paradigm Shift from Intelligence to Life', of the Ministry of Education, Science and Culture of Japan.

(This article is reviewed by Dr. Horst D. Simon.)

References

[1] M. Ogino, R. Shioya, H. Kawai, and S. Yoshimura, Seismic Response Analysis of Nuclear Pressure Vessel Model with ADVENTURE System on the Earth

Simulator, *Journal of The Earth Simulator*, vol.**2**, pp.41–54, 2005.

[2] F. Araki, H. Uehara, N. Ohno, and S. Kawahara, Visualization of Large-scale Data Generated by the Earth Simulator, *Journal of The Earth Simulator*, vol.**6**, pp.25–34, 2006.

[3] J. S. Painter, H. -P. Bunge, and Y. Livnat, Case Study: Mantle Convection Visualization on the Cray T3D, *IEEE Visualization 96*, p.409, 1996.

[4] http://adventure.q.t.u-tokyo.ac.jp/

[5] H. Kawai, M. Ogino, R. Shioya and S. Yoshimura, Parallel Visualization of Huge Scale 3-D Structural Analysis Using Server-side Rendering and Walkthrough, *APCOM'07*, Dec 3–6, 2007, Kyoto, Japan.

[6] N. L. Max, Vectorized Procedural Models for Natural Terrain: Wave and Islands in the Sunset, *ACM SIGGRAPH*, vol.**15**, no.3, pp.317–324, 1981.

[7] http://geofem.tokyo.rist.or.jp/

[8] Y. Okuda and K. Nakajima, *Parallel Finite Element Analysis [I] Cluster Computing*, Baifukan, Japan, 2004 (in Japanese).

[9] H. Kawai, ADVENTURE AutoGL: A Handy Graphics and GUI Library for Researchers and Developers of Numerical Simulations, *CMES*, vol.**11**, no.3, pp.111–120, 2006.

[10] S. Molnar, M. Cox, D. Ellsworth, and H. Fuchs, A Sorting Classification of Parallel Rendering, *IEEE CG&A*, vol.**14**, no.4, pp.23–32, 1994.

[11] http://www.sw.nec.co.jp/APSOFT/SX/rvslib/

[12] S. Doi, T. Takei, and H. Matsumoto, NEC Supercomputer Visualization Efforts, *IEEE CG&A*, pp.10–13, 2001.

[13] Y. Suzuki, K. Sai, F. Araki, H. Uehara, and H. Haginoya, Development of a Visualization Scheme for Large-scale Data on the Earth Simulator, *ES Annual Report*, *April 2002–March 2003*, pp.139–144, 2003.

[14] F. A. Ortega, C. D. Hansen and J.P. Ahrens, Fast Data Parallel Polygon Rendering, *SC*, pp.709–718, 1993.

[15] C. D. Hansen, M. Krogh, and W. White, Massively Parallel Visualization: Parallel Rendering, *Proceedings of SIAM Parallel Computation Conference*, pp.790–795, 1995.

[16] S. Whitman, A Load Balanced SIMD Polygon Renderer, *ACM SIGGRAPH*, pp.63–106, 1995.

Journal of the Earth Simulator

Volume 9 March 2008

The Earth Simulator Center, Japan Agency for Marine-Earth Science and Technology
3173–25 Showa-machi, Kanazawa-ku, Yokohama, 236-0001 JAPAN
Tel: +81-45-778-5792 Fax: +81-45-778-5490
URL: http://www.es.jamstec.go.jp/
E-mail: esc_journal@jamstec.go.jp

First edition: March 2008

Instructions for Authors

Journal of the Earth Simulator is directed not only to researchers in the earth science, but also to researchers from other academic fields as well as general readers who are interested in science and technologies. The journal is devoted to the publication of original research papers, technical articles, reviews, commentaries, proposals, opinions, introductions, and news, etc. with the aim of research promotions and disseminations.

Preparation of manuscripts

Manuscripts must be written in English. Since publishing staffs take care of the layout, it is unnecessary to submit manuscripts in a camera-ready form. Maximum length of manuscripts is not specified. (Details are presented in the "Author Guidelines for Journal of the Earth Simulator")

Submission of manuscripts

Authors are requested to submit the manuscript to the Earth Simulator Center, after having it reviewed by editors. The text and tables should be prepared in an electronic form either as text files or files using popular word-processing software such as MS Word, and must be accompanied by a high quality printout copy. Figures and photographs, even if they are supposed to be inserted among the text, must be submitted independently in the form of electronic files with their printout copies. Figures and photographs can be either black-and-white or color. The submitted manuscripts will not be returned unless specifically requested. (Details are presented in the "Author Guidelines for Journal of the Earth Simulator")

Copyright

The comprehensive copyright (including its utilization in electronic form) of the articles printed in the journal in principle belongs to the Earth Simulator Center. When quoting from other publications, authors should take into account the following issues: (a) to pay attention to the copyright of the given literature, (b) to get permission from the firm or publisher holding the copyright, before using figures, tables or photograph from other books and journals.

Contact Address

For enquiries relating to the submission of manuscripts, please contact the address below.

Editorial Office, Journal of the Earth Simulator
The Earth Simulator Center
Japan Agency for Marine-Earth Science and Technology
3173-25 Showa-machi, Kanazawa-ku, Yokohama, 236-0001 JAPAN
E-Mail esc_journal@jamstec.go.jp
TEL +81-45-778-5792 FAX +81-45-778-5490

Journal of the Earth Simulator Volume 9 March 2008

The Earth Simulator Center, Japan Agency for Marine-Earth Science and Technology